

AD-A264 513



WL-TR-92-2099

PULSE MITIGATION AND HEAT TRANSFER
ENHANCEMENT TECHNIQUES

VOL 5 - TRANSIENT LIQUID MOVEMENT IN HEAT
PIPE WICKS



DTIC
ELECTE
MAY 19 1993
S A D

L.C. Chow
J.H. Ambrose

University of Kentucky
Department of Mechanical Engineering
Lexington, KY 40506-0046

AUG 1992

FINAL REPORT FOR 07/01/87 - 07/31/92

APPROVED FOR PUBLIC RELEASE; DISTRIBUTION IS UNLIMITED.

83 5 10 047

93-11086


AERO PROPULSION AND POWER DIRECTORATE
WRIGHT LABORATORY
AIR FORCE MATERIEL COMMAND
WRIGHT-PATTERSON AFB OH 45433-6563

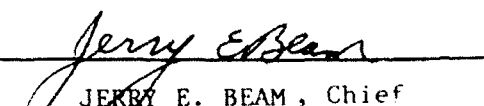
NOTICE


When Government drawings, specifications, or other data are used for any purpose other than in connection with a definitely Government-related procurement, the United States Government incurs no responsibility or any obligation whatsoever. The fact that the government may have formulated or in any way supplied the said drawings, specifications, or other data, is not to be regarded by implication, or otherwise in any manner construed, as licensing the holder, or any other person or corporation; or as conveying any rights or permission to manufacture, use, or sell any patented invention that may in any way be related thereto.

This report is releasable to the National Technical Information Service (NTIS). At NTIS, it will be available to the general public, including foreign nations.

This technical report has been reviewed and is approved for publication.


MICHAEL J. MORGAN
Project Engineer


JERRY E. BEAM, Chief
Thermal Technology Section


MICHAEL D. BRAYDON, LIAISON OFFICER
Depot, CSMF
Aerospace Center Building
Aerospace and Thermal Technology

If your address has changed, if you wish to be removed from our mailing list, or if the addressee is no longer employed by your organization please notify WL/POOS, WPAFB, OH 45433-6563 to help us maintain a current mailing list.

Copies of this report should not be returned unless return is required by security considerations, contractual obligations, or notice on a specific document.

REPORT DOCUMENTATION PAGE			Form Approved OMB No 0704-0188	
<small>Public reporting burden for this collection of information is estimated to average 1 hour per response, including the time for reviewing instructions, searching existing data sources, gathering and maintaining the data needed, and completing and reviewing the collection of information. Send comments regarding this burden estimate or any other aspect of this collection of information, including suggestions for reducing this burden, to Washington Headquarters Services, Directorate for Information Operations and Reports, 1215 Jefferson Davis Highway, Suite 1204, Arlington, VA 22202-4302, and to the Office of Management and Budget, Paperwork Reduction Project (0704-0188) Washington, DC 20503</small>				
1. AGENCY USE ONLY (Leave blank)		2. REPORT DATE AUG 1992		3. REPORT TYPE AND DATES COVERED FINAL 07/01/87--07/31/92
4. TITLE AND SUBTITLE PULSE MITIGATION AND HEAT TRANSFER ENHANCEMENT TECHNIQUES VOL 5 - TRANSIENT LIQUID MOVEMENT IN HEAT PIPE WICKS			5. FUNDING NUMBERS C F33615-87-C-2777 PE 63218 PR D812 TA 00 WU 08	
6. AUTHOR(S) G.C. Chow J.H. Ambrose				
7. PERFORMING ORGANIZATION NAME(S) AND ADDRESS(ES) University of Kentucky Department of Mechanical Engineering Lexington, KY 40506-0046			8. PERFORMING ORGANIZATION REPORT NUMBER UK-ME-92-01	
9. SPONSORING / MONITORING AGENCY NAME(S) AND ADDRESS(ES) ARMED FORCES RESEARCH AND POWER DIRECTORATE WRIGHT LABORATORY AIR FORCE MATERIEL COMMAND WRIGHT-PATTERSON AFB OH 45433-6563 WL/POOS, Attn: MORGAN 513-2552922			10. SPONSORING / MONITORING AGENCY REPORT NUMBER WL-TR-92-2099	
11. SUPPLEMENTARY NOTES				
12a. DISTRIBUTION / AVAILABILITY STATEMENT APPROVED FOR PUBLIC RELEASE; DISTRIBUTION IS UNLIMITED.			12b. DISTRIBUTION CODE	
13. ABSTRACT (Maximum 200 words) A new transient model for the liquid flow is presented. The continuous distribution of the saturation in the wick is modeled, where previous models had assumed a uniformly saturated structure. Solution of the liquid flow model requires that the saturation dependence of the capillary flow properties be known. These properties must be determined experimentally because of the complex geometry of the porous wick structures. An experimental study of the flow properties was performed for the case of multilayer mesh wicks. X-ray radiography was used to determine saturation distributions in the wicks for a variety of conditions. Capillary pressure and relative permeability were determined from independent experiments. Results of the transient liquid flow model compare favorably with the results from the heat pipe experiments.				
14. SUBJECT TERMS TRANSIENT HEAT PIPE PERFORMANCE, FLOW IN POROUS WICKS, LIQUID SATURATION, CAPILLARY PRESSURE, PERMEABILITY			15. NUMBER OF PAGES 165	
			16. PRICE CODE	
17. SECURITY CLASSIFICATION OF REPORT UNCLASSIFIED	18. SECURITY CLASSIFICATION OF THIS PAGE UNCLASSIFIED	19. SECURITY CLASSIFICATION OF ABSTRACT UNCLASSIFIED	20. LIMITATION OF ABSTRACT UL	

Table of Contents

	PAGE
Figures	iv
Tables	v
Nomenclature	viii
Chapter 1 INTRODUCTION	1
Basic Principles of Heat Pipes	1
Studies of Transient Heat Pipe Operation	4
Physics of Capillary Flow	7
Chapter 2. PRELIMINARY STUDY OF LIQUID MOVEMENT IN A HEAT PIPE	16
Analytical Model	22
Experimental Investigation	33
Comparison of Results	43
Saturation Dependence of Liquid Flow	43
Chapter 3 SATURATION MEASUREMENT IN HEAT PIPE WICKS	46
Alternative Methods	48
System for Measurement of Saturation using X-Ray Radiography	56
Heat Pipe with Saturation Measurement	64
Chapter 4 DETERMINATION OF CAPILLARY FLOW PROPERTIES	66
Wicking Rise Experiments	66
Analysis and Discussion of Results	80
Steady Flow in partially Saturated structures	87
Chapter 5 DETAILED STUDY OF TRANSIENT LIQUID FLOW	95
Beryllium Heat Pipe Tests	102

Accession For	
NTIS CRA&I	<input checked="" type="checkbox"/>
DTIC TAB	<input type="checkbox"/>
Unannounced	<input type="checkbox"/>
Justification	
By	
Distribution /	
Availability Codes	
Dist	Avail and / or Special
A-1	

Appendix A	UNCERTAINTY ANALYSIS	139
Appendix B	EVALUATION OF NUMERICAL PARAMETERS USED IN SPRINT CODE	147
REFERENCES		151

List of Figures

	PAGE
Fig 1 Details of a Simple Heat Pipe	2
Fig 2 Porous Media	8
Fig 3 Darcy Flow Experiment	8
Fig 4 Liquid/Vapor Meniscus and Contact Angle	10
Fig 5 Heat Transport by Vapor	18
Fig 6 Heat Pipe Operating Limits	19
Fig 7 Heat Pipe Start-Up	21
Fig 8 Determination of Time Constant	25
Fig 9 Lumped Model Prediction	26
Fig 10 Flat Front Model	28
Fig 11 Predicted Movement of Liquid Front	32
Fig 12 Heat Pipe Test Setup	35
Fig 13 Verification of Capillary Limit	36
Fig 14 Transient Temperature Profiles ($Q_{in}=125$ W)	38
Fig 15 Transient Temperature Profiles ($Q_{in}=225$ W)	39
Fig 16 Pulsed Start-Up with Thermal Storage	41
Fig 17 X-ray Diffraction Results	52
Fig 18 Optical Density Data	55
Fig 19 X-ray Chamber	59
Fig 20 X-ray Shutter System	60
Fig 21 Film Digitizing System	62
Fig 22 Steady-State Wicking Apparatus	70
Fig 23 Transient Wicking Rise Test	73
Fig 24 Images of Wicking Front	75

Fig 25	Transient Wicking Rise, 5-280 wick	76
Fig 26	Transient Wicking Rise, HC7-200 wick	77
Fig 27	Transient Wicking Rise, HC7-85 wick	78
Fig 28	Transient Wicking Rise, HC7-51 wick	79
Fig 29	Steady-State Rising and Falling Capillary Pressure	81
Fig 30	Comparison of Capillary Pressure Data with Other Materials	82
Fig 31	Steady-State Rising Capillary Pressure	84
Fig 32	Relative Permeability Calculated from Wicking Tests	86
Fig 33	Relative Permeability Apparatus	89
Fig 34	Relative Permeability Data from Steady Flow Experiments	92
Fig 35	Comparison of Relative Permeability Data	93
Fig 36	Wick Control Volume	96
Fig 37	Falling Capillary Pressure Data	99
Fig 38	Transient Saturation Profile, 15 W	103
Fig 39	Transient Saturation Profile, 20 W	104
Fig 40	Transient Saturation Profile, 25 W	105
Fig 41	Transient Saturation Profile, 30 W	106
Fig 42	Transient Saturation Profile, 35 W	107
Fig 43	Beryllium Heat Pipe Schematic	109
Fig 44	Diagram of Wick Structure	110
Fig 45	Graphite Heater	110
Fig 46	Heat Pipe Fill Station	112
Fig 47	Heat Pipe Experiment Schematic	114
Fig 48	Transient Saturation Profile, Test 1141	117
Fig 49	Transient Saturation Profile, Test 1141	118

Fig 50	Transient Saturation Profile, Test 1142	119
Fig 51	Transient Saturation Profile, Test 1142	120
Fig 52	Transient Saturation Profile, Test 1171	121
Fig 53	Transient Saturation Profile, Test 1171	122
Fig 54	Transient Saturation Profile, Test 1172	123
Fig 55	Transient Vapor Temperatures, All Tests	124
Fig 56	Transient Temperatures, Test 1141	126
Fig 57	Transient Temperatures, Test 1142	127
Fig 58	Transient Temperatures, Test 1171	128
Fig 59	Transient Temperatures, Test 1172	129
Fig 60	Steady-State Saturation Profile	130
Fig 61	Steady-State Temperatures	132
Fig 62	Spacial Dependence of Source Term	133
Fig 63	Temporal Dependence of Source Term	134
Fig A.1	Effective Attenuation Coefficient - Freon 113	142
Fig A.2	Effective Attenuation Coefficient - Methanol	143

LIST OF TABLES

	PAGE
Table 1. Flat Front Model Input Parameters	33
Table 2. Wick Properties	67
Table 3. Input Parameters for Detailed Liquid Flow Model	102
Table A-1 Uncertainty of Saturation Measurement	144
Table B-1 Effect of Grid Size	148
Table B-2 Effect of Time Step	149
Table B-3 Effect of Tolerance Placed on Time Integration	150

Nomenclature

A	area
C	effective heat capacity
c	crimping factor
d	screen wire diameter
d_w	wick diameter
D	optical density
$f(S)$	moisture diffusivity, Eq(38)
F_ℓ	friction coefficient, Eq(22)
g	gravitational acceleration
h	convective heat transfer coefficient
H	equilibrium rise height
J	source term, Eq(37)
k_{hp}	effective heat pipe thermal conductivity
K	full permeability, Eq(5)
K_r	relative permeability, Eq(7)
L	length
m	mass of liquid in pores
\dot{m}	mass flow rate
M	mass flux of vapor
n	number of layers
N	screen mesh number
P	pressure
P_m	available pumping head
P_c	capillary pressure
P^*	Leverett Function, Eq(24)

Q	heat transfer rate
r	radius of curvature or pumping radius
S	saturation (ratio of liquid volume to void volume)
S_i	irreducible saturation
t	time
T	temperature
U	area averaged velocity
V	volume
w	mesh opening
x	position coordinate
α	inverse time constant
β	contact angle
δ	thickness of single layer of mesh
ϵ	wick porosity
λ	latent heat of vaporization
γ	angle of inclination to horizontal
κ	attenuation coefficient
ℓ	thickness of material penetrated
μ	dynamic viscosity of liquid
ν	kinematic viscosity of liquid
ϕ	reduced saturation ($\phi = \frac{S - S_i}{1 - S_i}$)
ρ	density of liquid
σ	surface tension
θ	temperature difference

Subscripts

c	condenser section
d	dry
e	evaporator section
eff	effective
fs	fully saturated
H	heater
max	maximum capillary transport
ps	partially saturated
t	transport section
T	entire heat pipe
tot	total
v	vapor
w	wick cross section
o	reference
∞	ambient

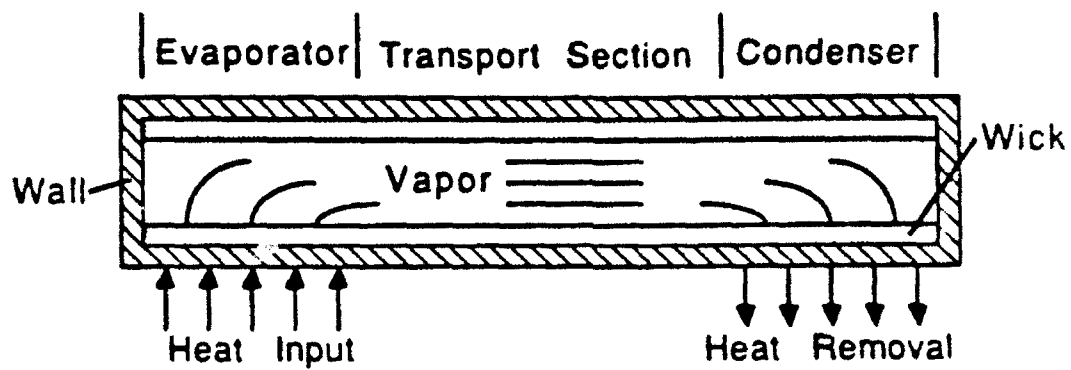
Chapter 1

INTRODUCTION

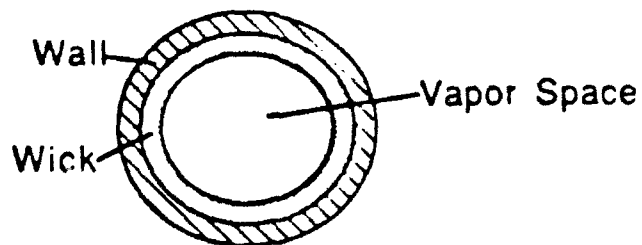
The objective of this research is to develop a thorough understanding of the operation of a low-temperature heat pipe during transient or pulsed heat loading. Central to this understanding is the knowledge of liquid movement and distribution in the wick. The low-temperature heat pipe is generally a capillary limited device. This means that the limitation to heat transport is usually a result of insufficient liquid return to the evaporator due to inadequate capillary pumping. The liquid flow to the evaporator is driven by the capillary pumping of the wick. The capillary pumping must balance the frictional resistance to flow caused by the restrictive nature of the flow path. This resistance to flow is common to all capillary structures and can be relatively large. Thus the understanding of the flow resistance and capillary pumping properties of the wick structure is most important to the understanding of transient operation of heat pipes.

Basic Principles of Heat Pipes

A heat pipe is in many cases a simple device, consisting of a container, a wick structure and a two-phase working fluid. The liquid phase of the working fluid occupies the void area of the wick structure and wets the wall and solid material of the wick. The most common configuration is shown in Fig 1. The liquid is evaporated at one end of the pipe through the addition of heat. The vapor then flows to the



Side Cross Section



End Cross Section

Fig 1 Details of Simple Heat Pipe

other end where it is condensed through the removal of heat. The liquid flows back to the evaporator through the wick structure to complete the cycle.

The wick structure can take many forms, but in the simplest case it consists of a porous material lining the interior wall of the heat pipe. The size and geometry of the pores play an important role in determining the magnitude of the capillary pumping and the frictional resistance.

The maximum power which the heat pipe can transport depends mainly on the working fluid and wick structure. The limitation arises when the amount of liquid returned to the evaporator section is insufficient to remove the heat input. For low-temperature heat pipes used in the 200 to 500 K temperature range, the major limitation to heat transport is called the capillary limit. The capillary pressure difference is at its maximum value and is exactly balanced by the frictional resistance to flow of the working fluid. The capillary limit represents a fundamental limitation of the capillary pumping of the wick structure. Capillary limits are commonly calculated utilizing the experimentally determined capillary flow properties. These conditions correspond to the maximum capillary pumping and the minimum frictional resistance.

Because heat pipes are passive devices and can transport heat over relatively large distances (of the order of a meter or more) with very small temperature drop, they are important to an increasing number of applications. Important applications have been witnessed in spacecraft thermal control, waste heat recovery and nuclear power generation. Because of these important applications, much heat pipe research has been performed over the last two decades. The bulk of this research

focused on developing new types of heat pipes, or modeling of heat pipe operation under a variety of conditions. The study of heat pipe operation under transient conditions has received particular attention in recent years. The transient behavior of heat pipes is controlled by a complex coupling of the heat transfer and fluid flow phenomena which has not been completely understood.

Studies of Transient Heat Pipe Operation

There has been a great interest in the modeling of transient heat pipe behavior in the last decade. This is a direct result of the increasing number of applications of heat pipes in thermal control. Because heat loading histories in actual applications are dictated by the heat producing elements, designers of heat pipes must be able to predict accurately the performance of the devices under a wide range of heat loading conditions. Pulsed loading profiles, which are the most severe from the standpoint of heat pipe operation, are not uncommon in actual applications, especially in cooling of electronics. To reduce the severity of the pulse profile of an on/off heat producing element requires some form of thermal buffer. However this reduces the heat transfer coefficient and nullifies the gains obtained from employing heat pipes. In direct contrast to pulsed loading, the common method used for testing heat pipes is to increase the heat load in small increments while allowing a sufficient time between changes for the device to reach steady-state operation.

Many previous studies of transient behavior of heat pipes have been

reported in the literature. However, the bulk of the literature will not be reviewed here. Rather, some of the recent literature pertinent directly to the present approach will be reviewed. The present work is not aimed at development of a comprehensive transient heat pipe model, but rather a unique approach to modeling of the liquid flow in the wick suitable for application to transient heat pipe modeling. For a more complete review of recent heat pipe modeling in general, the interested reader is referred to the review papers by Dobran [1] and Polasek [2].

Beam [3] studied transient heat pipe operation using a flat front model for the liquid flow. When the capillary limit is exceeded, the liquid is depleted from the wick. The liquid/vapor interface starts at the evaporator end farthest from the condenser and proceeds toward the adiabatic section. The time to reverse the motion of this front was defined as the rewetting time. A lumped model was used to predict the temperature response of the pipe. The rewetting time was compared to recovery periods noted in the experimentally obtained transient temperature profiles.

Holderness [4] studied the operation of a heat pipe at heat inputs greater than the capillary limit. His study also focused on the response of the heat pipe to pulsed heat loads and he too employed a flat-front model. He modeled the temporal behavior of the flat-front based on mass, momentum and energy balances on the wick and studied the effects of time constant and pulse size. He employed constant values of the capillary pressure and permeability in his model, but did account for the hysteresis of the capillary pressure. This detailed study included many interesting theoretical conclusions. However, it has been cited very little as a reference in other works, possibly because the

author did not publish his findings in more accessible fora.

Change [5] completed a detailed study of transient heat pipe behavior. He utilized a transient, two-dimensional, finite difference solution to the energy equation to obtain the temperature response. His overall heat pipe model did not include the liquid flow. However, he did use a flat-front model to predict when dryout behavior would occur. He conducted extensive testing of a slab-wick, Freon heat pipe, including measurement of internal vapor and wick temperatures. Tests included startup from the supercritical state. This was one of the first works with detailed internal measurements of transient temperature profiles.

Moss and Kelly [6] utilized neutron radiography to measure the liquid amounts in a heat pipe evaporator under steady-state operating conditions. The heat pipe used water as the working fluid and a thick (0.25 inch) wick of sintered stainless steel mesh. They used two models to describe the heat transfer in the evaporator. Both of these were based on the assumption that a steady layer of vapor blankets the evaporator section of the heat pipe wall. This is not likely to be the case in the thin wicks used in most heat pipes unless severe dryout occurs.

Eninger [7] studied the capillary pressure and permeability of a metal fiber wick. He used a beta ray attenuation method to measure saturation in the wick. He obtained capillary pressure as a function of saturation for both rising and falling cases. He developed a theoretical model for the capillary pressure starting from a force balance on a randomly oriented fiber. The theoretical model required an empirical constant obtained from the experimental results. Eninger also

measured permeability of the wick structure under conditions of partial saturation. However, saturation measurements could not be obtained for the permeability experiments.

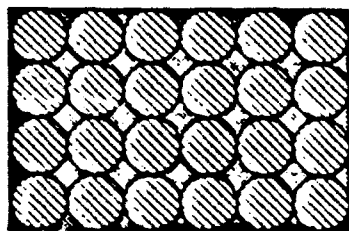
Shishido et al. [8] used a transient drainage experiment to determine the saturation dependence of the lumped frictional and capillary effects. They modeled the capillary limit based on a saturation dependent model by first assuming capillary pressure to be a linear function of saturation. They obtained saturation measurements under steady-state operating conditions in a heat pipe with wick structures of glass beads and crushed brick powder and water as the working fluid. These saturation data were obtained from discrete capacitance measurements. The capacitance of the wick structure depends upon the amount of liquid present. The measured steady state saturation distributions compared fairly well with the predicted distributions. These steady-state saturation distributions showed that the saturation dropped steeply in the evaporator region for large heat inputs. This offers support to the use of the flat-front model for the liquid flow.

Physics of Capillary Flow

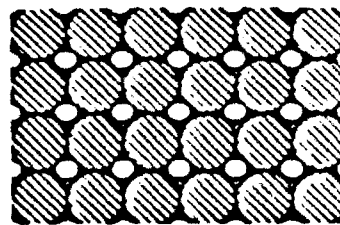
The basic phenomena controlling flow of fluids in capillary structures will be discussed in this section. First, the basic terminology will be explained.

The saturation is a measure of the amount of liquid present in a porous material. It is defined as the fraction of the void volume of a porous material which is occupied by liquid phase. Fig 2a illustrates a

fully saturated porous structure and Fig 2b illustrates the case of



a. Fully Saturated



b. Partially Saturated

Fig 2 Porous Media

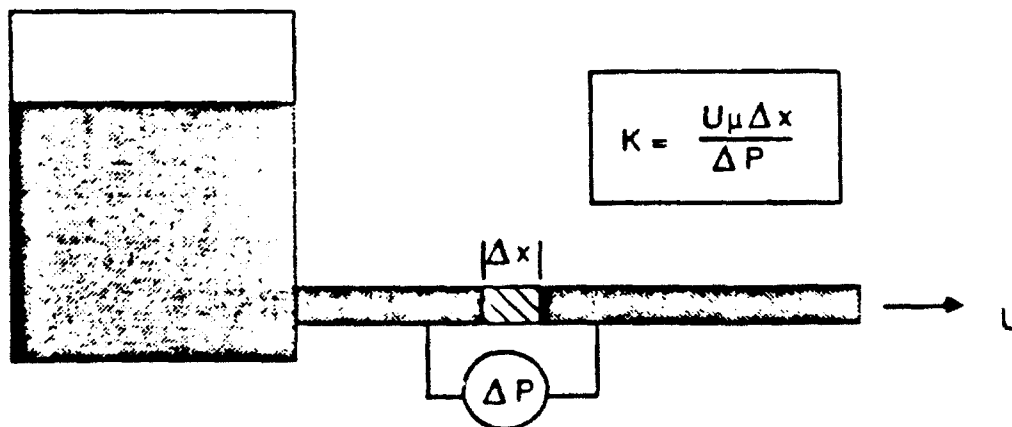


Fig 3 Darcy Flow Experiment

a partially saturated structure.

The capillary pressure or capillary pumping is the pressure difference between the liquid and gaseous phases occupying a porous material. It is due to the free energy of the interface between the phases. The capillary pressure is zero for the case of Fig 2a, while it is approaching the maximum value for the case of Fig 2b.

The permeability is a measure of the frictional resistance to flow of fluid through a porous material. It is defined empirically by Darcy's Law. This empirical definition is illustrated in Fig 3, where a given pressure drop across a fully-saturated, porous sample of known length produces a given flow velocity.

Capillary Pressure

The capillary pumping is developed due to pressure lowering across the curved liquid/vapor interface which occurs when the liquid recedes into the pores or void space of the wick. Because the liquid wets the solid phase of the wick structure, as the volume of liquid is reduced the curved interface necessarily occurs. The phenomenon of capillary pumping is described by the equation of Laplace and Young [9]:

$$P_c = \frac{\sigma \cos\beta}{1/r_1 + 1/r_2} \quad (1)$$

This equation shows that the capillary pressure depends on the two principal radii of curvature, r_1 and r_2 of the liquid/vapor interface and the contact angle. The contact angle illustrated in Fig 4 depends on the liquid/solid combination. The radius of curvature of the

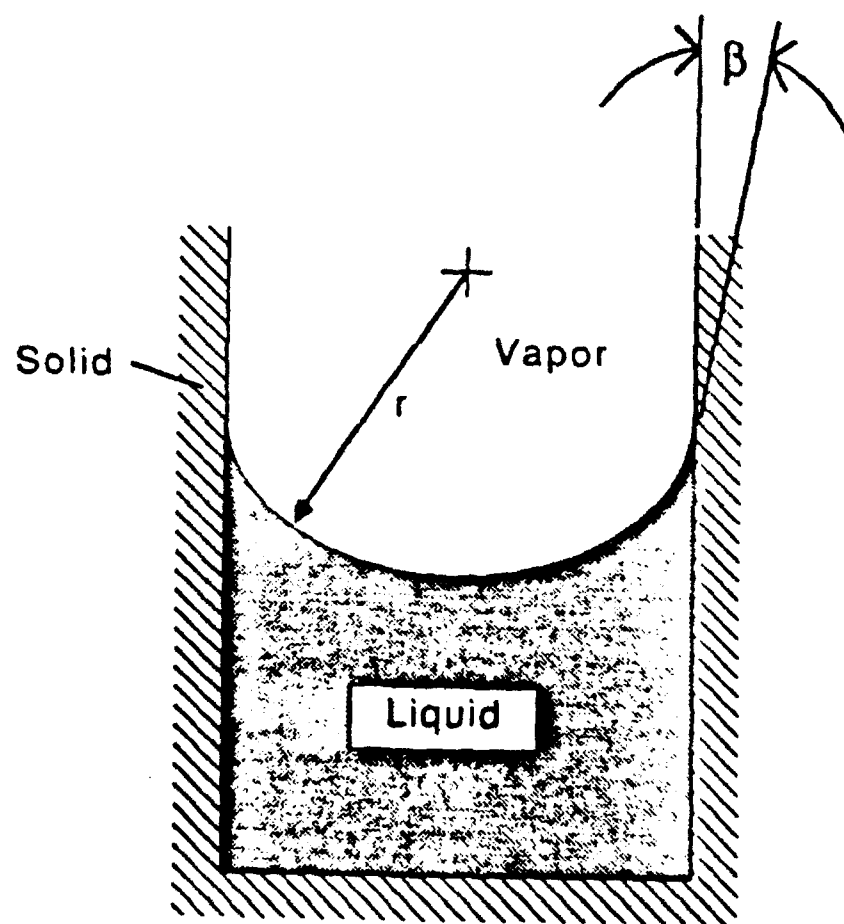


Fig 4 Liquid/Vapor Meniscus and Contact Angle

interface depends upon the geometry of the pore, the volume of liquid wetting the pore and the contact angle. For a given fluid and porous structure, the capillary pressure depends primarily on the amount of liquid present in the voids.

Due to the complex geometry of commonly encountered porous materials, Eq(1) may not be used directly. Instead the capillary pumping is determined experimentally. The experimental determination of capillary pumping usually consists of placing one end of a dry wick sample in contact with a pool of liquid, allowing it to imbibe liquid from the pool and measuring the height to which the liquid rises. This height is termed the rising wicking height. Since the liquid is in equilibrium, the pressure distribution is hydrostatic, and the maximum capillary pressure corresponds directly to the wicking rise height.

Because of the phenomenon of capillary hysteresis, the rising wicking height is different from the falling wicking height, which would be obtained if an initially saturated wick sample were allowed to drain into a pool of liquid. The capillary hysteresis is attributable to two causes. One is the hysteresis of contact angle. The contact angle is not necessarily a constant, but instead depends upon whether the liquid is advancing or receding from the solid surface. The second cause applies mainly to porous structures (as opposed to grooved surfaces). For a given equilibrium capillary pressure distribution, there is a range of configurations in which a liquid may exist within the porous structure. Smith [10] showed this to be true in his pioneering studies of moisture distributions in packed beds of spheres. He explained final distributions which occur under drainage conditions in terms of three distinct regimes. In the first, small ring-shaped pockets of liquid

exist around points of contact between spheres. This is called the pendular regime, in reference to the shape of the liquid pockets. There is no communication between these pockets other than by evaporation and condensation. We may refer to the amount of liquid present as the irreducible saturation S_i , since no matter where the free surface of the liquid is located, it has no effect on this type of liquid distribution. In the second regime, the rings of liquid grow and coalesce to form larger pockets of liquid which may enmesh several points of solid/solid contact. This is the regime of hysteresis because for a given height above the free surface of the liquid, many distributions of the liquid are possible. The amount of liquid present in this regime is bounded by the amounts corresponding to the irreducible saturation and fully saturated conditions. The last regime is at or below the free surface of the liquid, where the voids are completely filled with liquid.

Extensive measurements of the saturation distributions of water in sand made by Leverett [11] verified the general shape of the distributions predicted by Smith. Although a range of distributions could exist in theory, two distinct distributions are exhibited in practice. These correspond to the rising and falling cases.

The dependence of capillary pressure on saturation has been discussed only for the static case. The question arises as to whether the relationship is the same for the dynamic case, in which a flow of fluid occurs in the direction of a negative gradient in capillary pressure. The phenomenon of capillary pressure is due to free energy of the liquid/vapor interface. Movement of the liquid below the interface should therefore have no effect on this phenomenon. Indeed, Brown [12] has shown the two relationships to be identical based on measurements of

capillary pressure under both static and dynamic conditions in limestone cores. Thus in the present study it will be assumed that the capillary pressure measured under static conditions holds also for dynamic conditions.

Empirical expressions have been developed based on experimental capillary pressure data for various wick types. These involve defining an effective capillary radius from the equilibrium rise height. The effective capillary radius is defined by:

$$P_c = \rho g H = \frac{2\sigma}{r_{eff}} \quad (2)$$

where H is the maximum wicking height. Equation (2) is the form of Eq(1) for a spherical meniscus. These expressions are commonly used by designers of heat pipes to determine the maximum capillary pumping that a particular wick structure can produce. An example is the expression for the effective capillary radius of a square-mesh screen wick [13]:

$$r_{eff} = \frac{1}{2N} \quad (3)$$

When this expression is used to calculate the maximum capillary pumping of a square-mesh screen wick it yields:

$$P_c = 4\sigma N \quad (4)$$

Permeability

The frictional resistance to flow in a fully saturated wick is defined empirically by Darcy's Law:

$$U = - \frac{K}{\mu} \frac{dP}{dx} \quad (5)$$

The velocity U is the bulk velocity obtained by averaging the volumetric flow over the entire cross-sectional area. Darcy's Law is generally valid for low velocities. In particular, it is considered valid for $Re < 1$, where the Reynolds number Re is based on pore size. This is the case in porous heat pipe wicks.

For a given structure the permeability has been shown to depend upon the amount of fluid present in the voids. Unlike the capillary pumping, the permeability depends primarily on the geometry of the porous structure rather than the fluid properties. This leads to the definition of the relative permeability, which is used to model flow where more than a single fluid phase is present. Extensive studies of the flow of water/gas/oil mixtures in sand and rock formations have been performed in connection with oil recovery [14,15,16]. These studies showed that the pressure drop across a porous material is higher for two or more phases than for a single phase alone. This phenomenon is accounted for by introducing a separate permeability for each phase present. Thus Darcy's Law is written separately for each phase:

$$U_1 = \frac{K_1}{\mu_1} \frac{dP_1}{dx}, \quad U_2 = \frac{K_2}{\mu_2} \frac{dP_2}{dx}, \quad \dots \quad (6)$$

Each permeability is given as a fraction of the normal, single-phase permeability (hereafter referred to as the full permeability):

$$K_1 = K_{r1} K \quad (7)$$

The relative permeability K_{r1} so defined may take on values of zero to 1. K_{r1} is equal to 1 when the structure is fully saturated with component 1 and is equal to zero when the saturation of component 1 has dropped to zero.

The concept of relative permeability is common in the modeling of flow in geological and structural materials. Recent work by Udell [17,18] utilized the relative permeability in conjunction with mass, momentum and energy balances to model flow and phase change heat transfer in water-saturated, packed beds of sand. Relative permeability has not often been used to model the flow of fluid in heat pipe wicks.

The resistance to flow in a heat pipe wick may differ markedly from that calculated based on the full permeability. This will occur when portions of the wick are occupied by vapor, due to the recession of the liquid/vapor interface or boiling of the liquid in the wick.

Chapter 2 presents results of a preliminary study to determine if the simplified approach to liquid-flow modeling can provide detailed information concerning drying and rewetting of the wick. In Chapter 3 the selection and implementation of a technique for measurement of saturation in wick structures are described. Chapter 4 presents results of detailed measurements of the saturation dependence of the capillary flow properties. Development and verification of a detailed model for the liquid flow are presented in Chapter 5.

Chapter 2

PRELIMINARY STUDY OF LIQUID MOVEMENT IN A HEAT PIPE

In this chapter, the results of the preliminary study are presented. The objective of the preliminary study was to evaluate the usefulness of the flat-front model for predicting dryout and rewetting behavior. This work involved extension of the model of Beam [3] and comparison of the model with data from transient heat pipe experiments.

In recent years, the subject of transient heat pipe behavior has received considerable attention [3,5,19,20]. Prediction of heat pipe behavior when subjected to pulsed loading or transient heat loads has become an important research area. Several key questions in this area have yet to be fully answered and require further study. The most obvious of these questions are:

1. Will a heat pipe achieve normal operation after a suddenly applied load, and if so, under what circumstances?
2. If there is a dryout of the wick as a result of a pulsed heat load, under what circumstances will the heat pipe regain isothermal operation?

To address these questions, a series of transient heat pipe tests were performed and the performance characteristics were analyzed using a simplified model of the liquid flow and thermal response. Pulsed heat loading at the evaporator was selected as a worst-case condition for the study of transient operation of heat pipes.

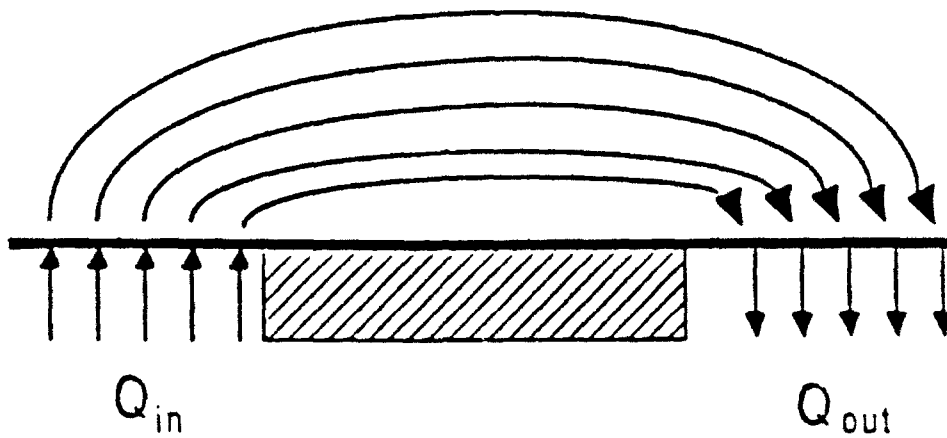
Pulsed Heat Pipe Start-Up

When a heat pipe is subjected to a sudden pulse of heat, the transient response will depend on the heat pipe geometry, working fluid, heat-input rate, cooling rate and the effective heat capacity of the heat pipe.

Consider the case of a heat pipe with convective cooling at the condenser. During steady-state operation all energy input at the evaporator is transported by vapor and rejected at the condenser as depicted in Fig 5a. During a pulsed start-up(Fig 5b), a portion of the energy addition at the evaporator is stored in the evaporator section. The remainder is used to vaporize the working fluid. The energy stored in the vapor is transported to the condenser and transport sections and part of it is used to heat up these two sections through condensation. The rest is rejected to the ambient. Both condenser and transport sections thus act as heat sinks, and this decreases the effective liquid-return path to the evaporator (average distance liquid must be pumped). If no dryout occurs, the heat pipe temperature will eventually reach a steady-state value which is sufficiently larger than the ambient fluid temperature to allow rejection of the entire heat- input rate. The energy transported by the vapor flow from the evaporator to the rest of the heat pipe will henceforth be referred to as the heat-transport rate. Except during steady-state operation, this is not the same as the heat-input rate. During start-up, the temperature, heat-transport rate, heat-rejection rate and thermal storage rate will all be changing with time.

Heat-transport limit curves for the water heat pipe used in the present study are shown in Fig 6. The capillary limit is calculated

a Steady State



b Start Up

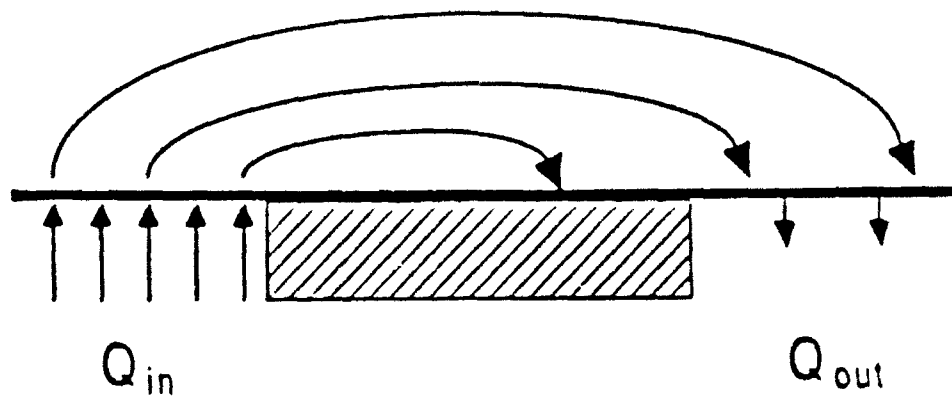


Fig 5 Heat Transport by Vapor

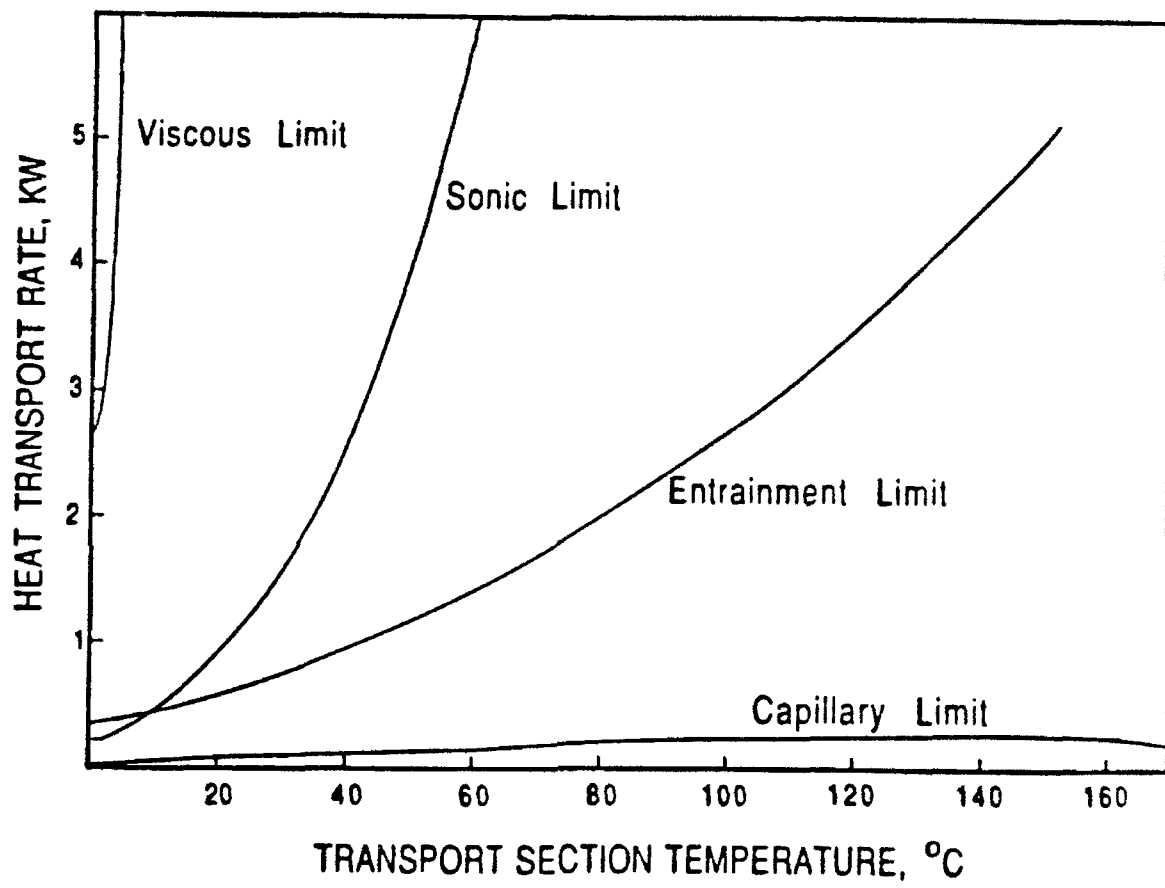


Fig 6 Heat Pipe Operating Limits

assuming constant flow properties. For screen-wicked, water heat pipes, the viscous, sonic and entrainment limits typically have much larger values than the capillary limit, even for temperatures only slightly above 0 °C. The viscous, sonic and entrainment limits depend on the vapor density. Water has sufficiently high vapor density that these heat-transport limitations are not usually encountered in screen-wick heat pipes unless extremely small vapor-flow passages are used. For this reason the capillary limit is the only heat-transport limit considered in this study. As seen in the figure, the capillary limit increases with temperature up to about 140 °C and then decreases. This occurs because of the change in physical properties of the working fluid with temperature. The capillary limitation is a balance between capillary pumping and viscous resistance forces. It thus depends on the ratio of surface tension to viscosity of the working fluid. For water, both properties decrease with increasing temperature. However, the ratio of the two properties increases up to about 140 °C, causing the capillary limit to increase. Above this temperature, the surface tension decreases more rapidly than the viscosity.

Two previous investigations of transient heat pipe behavior have concluded that the flow in a screen wick can respond very quickly to a capillary-induced pressure gradient and thus exhibits a quasi-steady behavior [3,5]. This means that a heat pipe with a screen wick should accommodate a pulsed heat load as large as the capillary limit without dryout.

Pulsed start-up refers to a step increase in power input from zero to some constant magnitude. The curves in Fig 7 represent two possible operating conditions (heat-transport rate due to vaporization

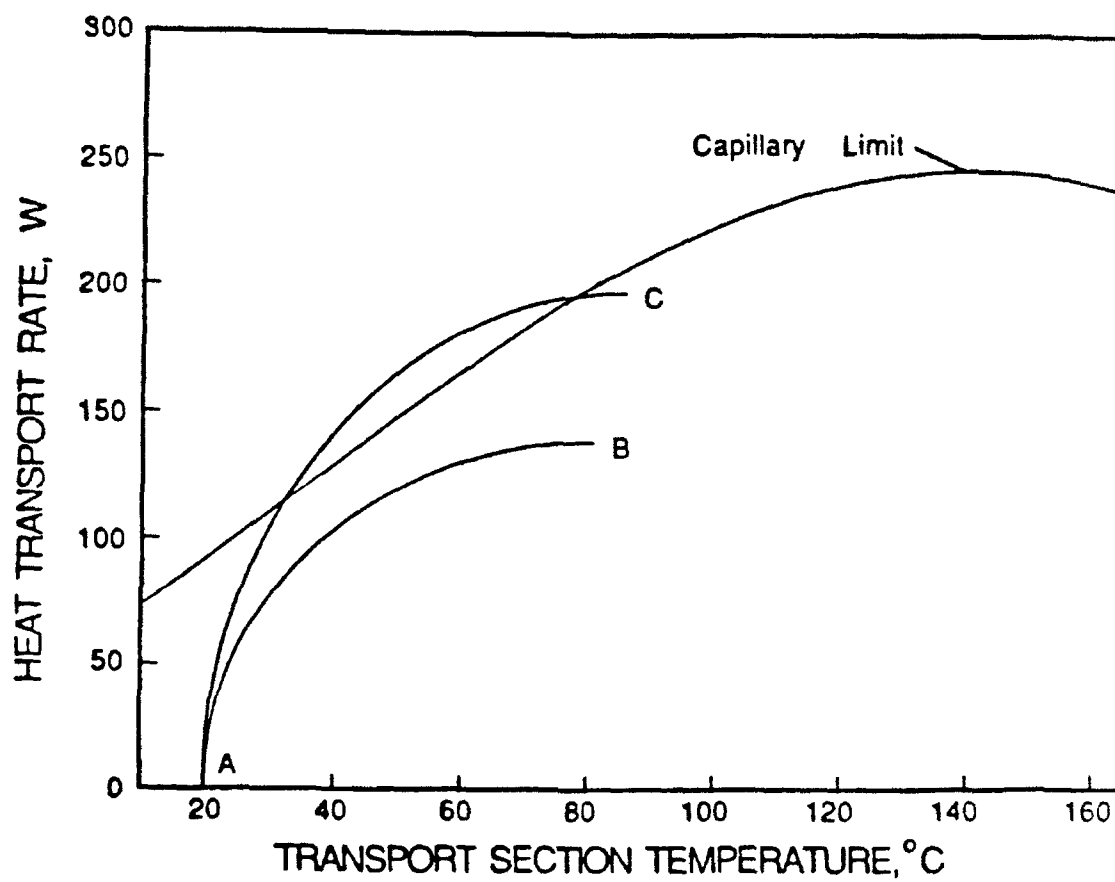


Fig 7 Heat Pipe Start-Up

versus transport-section temperature) during a pulsed start-up. These curves rise steeply and then level off because the thermal energy storage is initially large, but the heat-transport rate increases quickly until it approaches the steady-state value. If the heat-transport rate is less than the capillary limit during the entire response period, no dryout will occur. This situation is represented by curve AB. For a given constant pulse magnitude, the heat-transport rate may initially exceed the capillary limit. As the temperature increases, the capillary limit may become larger than the heat-transport rate. This case is shown by curve AC in Fig 7. If this situation occurs, the wick in the evaporator will dryout partially, followed by rewetting when the capillary limit again becomes smaller than the heat-transport rate.

Analytical Model

Transient Temperature Response

Beam [3] developed a lumped parameter model from an energy balance on the entire heat pipe. Since the effective thermal conductivity of the heat pipe is very large, the Biot number (hL_T/k_{hp}) is small : 1 the lumped parameter approach is justified. An energy balance for the entire heat pipe gives:

$$Q_{in} = Q_{out} + Q_{stored} \quad (8)$$

If the heat pipe is cooled by convection to an ambient fluid (transport

section insulated) the energy balance becomes:

$$Q_{in} = hA_c \theta + C_T \frac{d\theta}{dt} \quad (9)$$

where $\theta = T - T_\infty$. The heat transfer coefficient for the case of forced air cooling is only weakly dependent on the temperature. The variation of the effective heat capacity with temperature was calculated and is negligible. The solution to Eq(9) is:

$$\theta = \theta_0 e^{-at} + \frac{Q_{in}}{hA_c} \left[1 - e^{-at} \right] \quad (10)$$

where $\theta = \theta_0 = T_0 - T_\infty$ at $t=0$ and $a^{-1} = \frac{C_T}{hA_c}$ is the time constant. This is simplified to:

$$\theta = \frac{Q_{in}}{hA_c} \left[1 - e^{-at} \right] \quad (11)$$

for $\theta_0=0$, when the pipe is initially in equilibrium with the surroundings.

The values of the time constant and the heat transfer coefficient are determined experimentally for a given heat pipe and cooling condition. At steady state, the energy storage term becomes zero and Eq(9) becomes:

$$Q_{in} = hA_c \theta \quad (12)$$

Thus the heat transfer coefficient can be obtained from the measured heat input and average temperature. During a pulsed start-up, the average temperature is measured as a function of time and the inverse time constant a is determined from:

$$\ln \left[\frac{Q_{in}}{Q_{in} - hA_c \theta} \right] = at \quad (13)$$

The right side of Eq(13) is plotted versus time from experimental pulsed start-up data in Fig 8. The graph indicates that during the first 45 seconds of the pulse period there is a significant thermal lag. The thermal lag occurs because the electric heater must be heated up before it can supply heat to the heat pipe. Early in the pulse period, the heater absorbs most of the energy input. Given the measured heat capacity of the heater, $C_H = 105 \text{ J/}^\circ\text{C}$, it can be shown that, for the range of heat input considered, the thermal lag is of the order of 50 seconds.

The transient temperature response, Eq(10), has been modified slightly to account for the thermal lag. The thermal lag is characterized by the nonlinear behavior of the data in Fig 8 near $t=0$. If the thermal lag is accounted for, the temperature response becomes:

$$\theta = \frac{Q_{in}}{hA_c} \left[1 - e^{-at+0.08} \right] \quad (14)$$

For t less than 45 seconds, this solution has a much larger slope than the measured data, as shown in Fig 9. This is corrected by approximating the temperature for $t < 45$ seconds by a linear profile

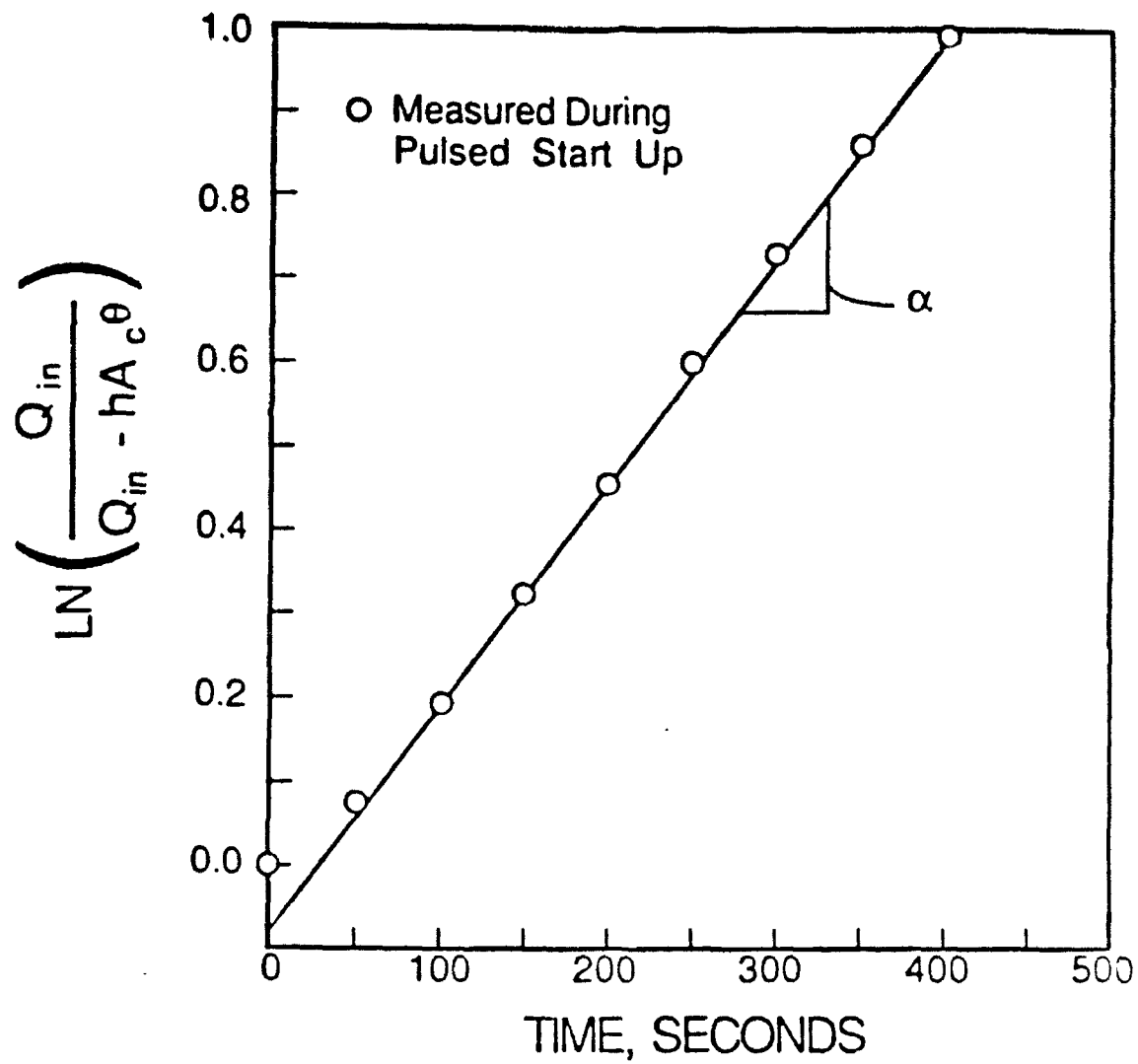


Fig 8 Determination of Time Constant

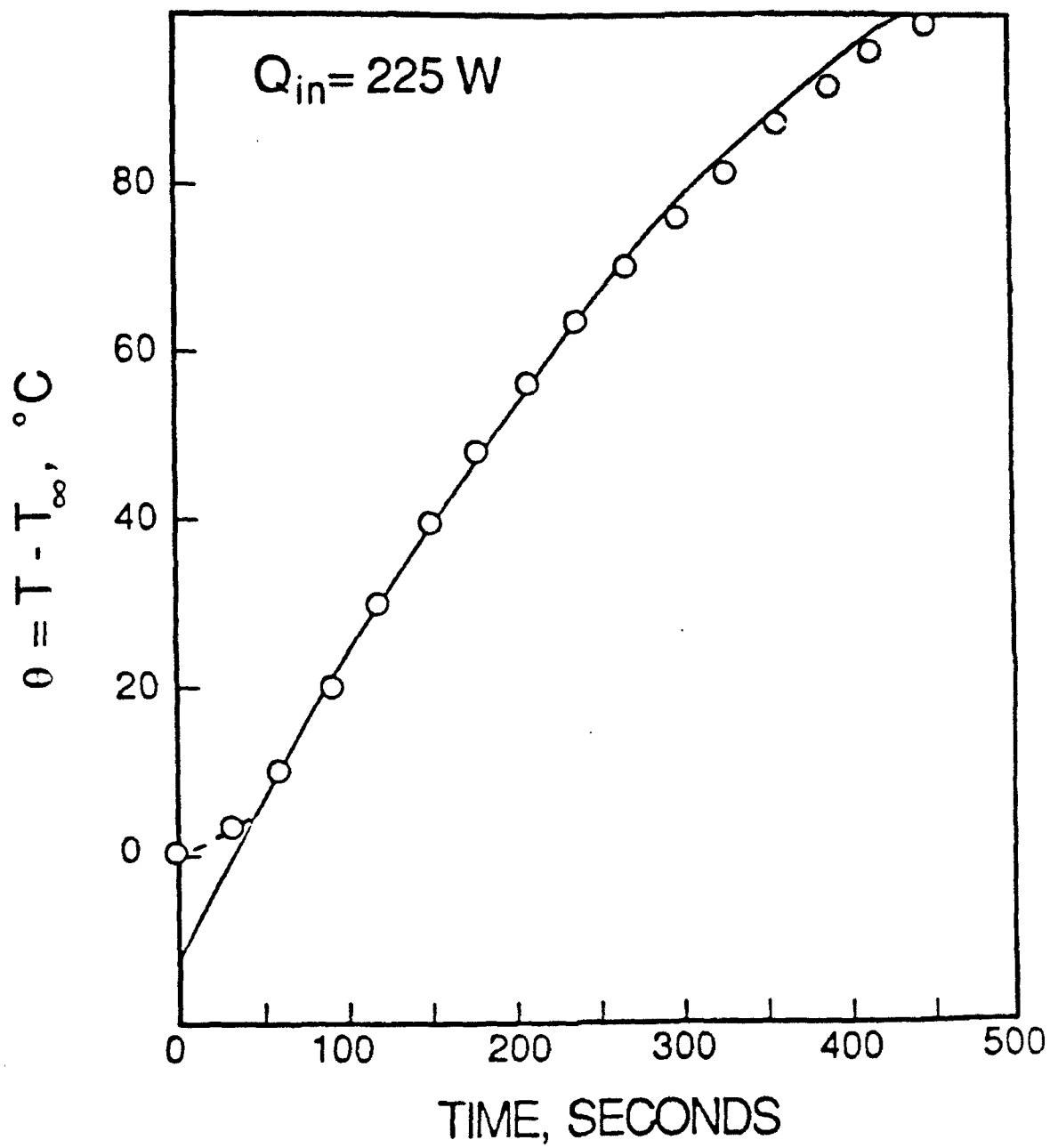


Fig 9 Lumped Model Prediction

(dotted line, Fig 9). The reduced rate of energy storage in the heat pipe during the initial pulse period is expected because of the additional energy storage required by the heater. The modified transient temperature response is given by:

$$\begin{aligned} \theta &= \frac{\theta(45)}{45} t & t \leq 45 \text{ s.} \\ \theta &= \frac{Q_{in}}{hA_c} \left[1 - e^{-at+0.08} \right] & t > 45 \text{ s.} \end{aligned} \tag{15}$$

Flat-Front Model for Liquid Flow

Beam [3] modeled dryout of the wick at the evaporator by assuming a distinct interface to exist between completely dry and completely saturated regions. The interface is perpendicular to the liquid flow direction and serves as a moving boundary of the control volume as shown in Fig 10. This simplified model is used in the present investigation to model the drying and rewetting of the wick during a pulsed start-up with thermal storage. The flat-front approximation has also been used by Chang and Colwell [19] and Holderness [4] in studies of transient heat pipe behavior.

Movement of the liquid/vapor interface shown in Fig 10 is governed by continuity of the mass flow entering (liquid) and leaving (vapor) the control volume. If the liquid enters from the right in the positive x-direction with velocity U , conservation of mass of the liquid requires that:

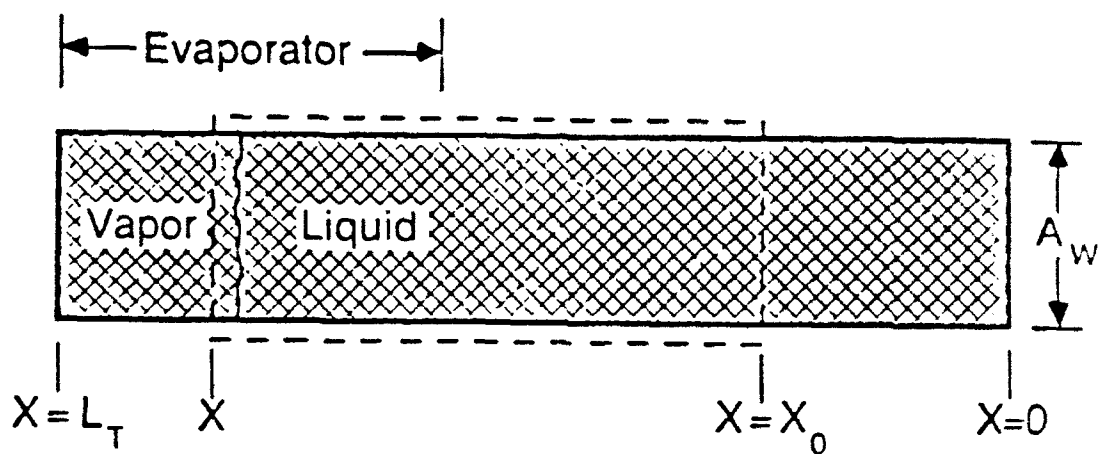


Fig 10 Flat Front Model

$$\rho A_w U = \rho A_w \frac{dx}{dt} + \dot{m}_v , \quad (16)$$

where \dot{m}_v is the mass flow rate of vapor leaving due to evaporation. The flow within the wick is slow and Darcy's Law is assumed to be valid, thus:

$$U = \frac{P_m K}{\mu(x - x_0)} , \quad (17)$$

where: $P_m = 4\sigma N - \rho g d_w$
 and: $x_0 = \frac{L_e + L_c}{2} .$

The maximum capillary pressure available for pumping P_m is based on the uppermost portion of the wick in the evaporator and is calculated by subtracting the loss in hydrostatic head associated with the diameter of the heat pipe wick from the maximum capillary head of the wick $P_c = 2\sigma/r_{eff}$. Eq(3), the commonly used expression for the effective capillary radius of a screen wick is used.

The permeability K is estimated from a modified Blake-Kozeny equation [13]:

$$K = \frac{d^2 \epsilon^3}{122(1 - \epsilon)^2} . \quad (18)$$

In Eq(17), $x - x_0$ represents an equivalent pumping length. This is consistent with the calculation of the capillary limitation to heat

transport based on the effective length for the liquid return [13]:

$$L_{\text{eff}} = L_t + \frac{L_e + L_c}{2} . \quad (19)$$

For a given value of x , the maximum capillary pumping head is assumed. This assumption is made because of the nature of the simplified model. If a distinct interface exists within the wick (rather than at the surface), then the minimum pumping radius of the wicking material would likely exist at this interface.

Because of the thermal storage, the vapor mass flow rate \dot{m}_v in Eq(16) will vary with time. This fact was not included in the earlier analysis of Beam [3]. The temperature profiles measured in heat pipe tests show that the axial conduction along the shell and wick is small, thus the energy stored in the transport and condenser sections of the heat pipe must be supplied by condensation of vapor. An energy balance on the evaporator section yields:

$$Q_{\text{in}} = C_e \frac{d\theta}{dt} + \dot{m}_v \lambda , \quad (20)$$

where the last term is due solely to evaporation and the heat capacity C_e is the portion of the total heat capacity attributed to the evaporator section. Eq(20) is combined with Eq(15) to define the mass flow-rate of vapor as:

$$\dot{m}_v = \frac{1}{\lambda} \left[Q_{in} - C_e \frac{\theta(45)}{45} \right] ; \quad t \leq 45 \text{ s} ,$$

$$\dot{m}_v = \frac{Q_{in}}{\lambda} \left[1 - \left[\frac{C_e}{C_T} \right] e^{-at+0.08} \right] ; \quad t > 45 \text{ s} .$$
(21)

Eqs(16,21) describe the movement of the liquid front during a pulsed start-up with thermal storage.

Solution of Eq(16) proceeds from starting conditions of a wick initially full of liquid and a constant heat load applied at $t=0$. These conditions correspond to (see Fig 10):

$$x(t=0) = L_T, \quad Q_{in}(t \geq 0) = \text{constant} .$$

Eqs(16,21) were solved by the fourth-order Runge-Kutta method to obtain a solution for the position of the liquid front as a function of time. At each new time step, the mean operating temperature was evaluated from the modified transient temperature response, Eq(15). The fluid properties were then evaluated at this temperature using polynomial approximations taken from [21].

The solution utilized the experimentally determined parameters a and h . It was carried out for the case of a 45.72 cm (18 in) long heat pipe with a 4-layer, 100-mesh screen wick. The value of h used in the solution corresponds to the case of forced-air cooling and the evaporator, transport and condenser lengths are 10.16 cm (4 in), 25.4 cm (10 in) and 10.16 cm (4 in), respectively. The input parameters used for the analytical model are listed in Table 1.

The behavior of the liquid front is shown in Fig 11 for various

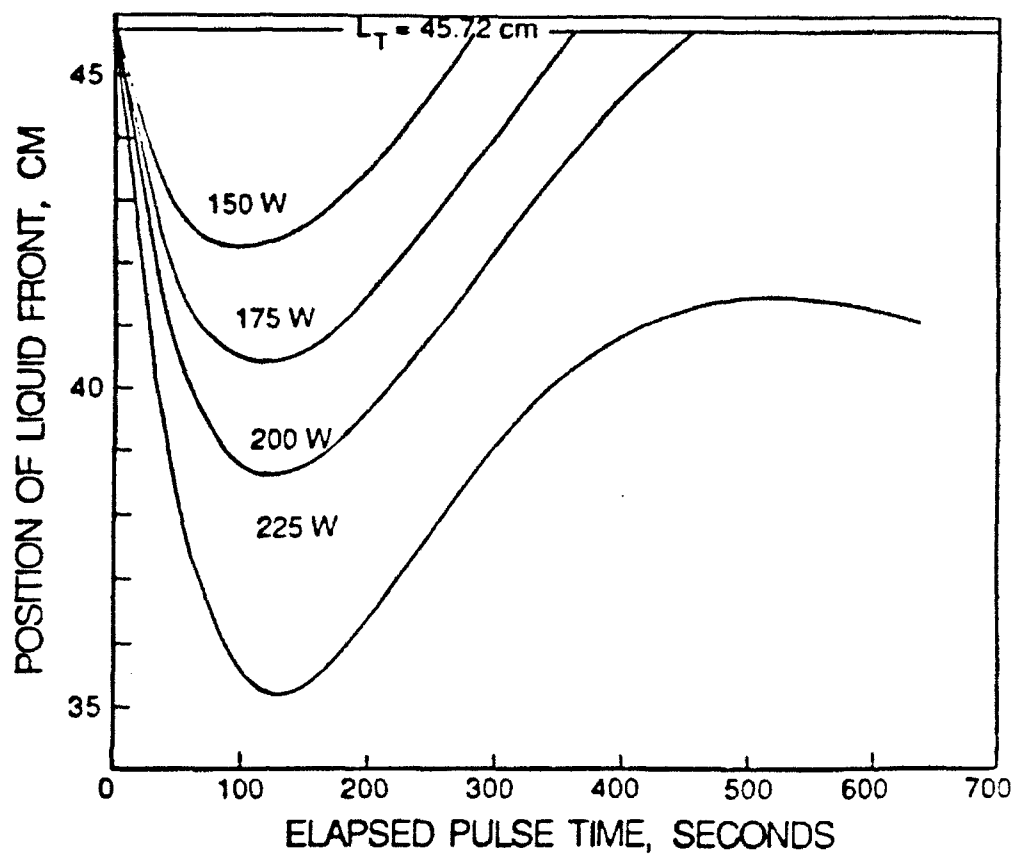


Fig 11 Predicted Movement of Liquid Front

Table 1. Flat Front Model Input Parameters

Constants	Dimensions
$a - 2.55(10^{-3}) \text{ s}^{-2}$	$A_w - 5.75(10^{-5}) \text{ m}^2$
$h - 200 \text{ W/m}^2\text{oC}$	$A_c - 7.13(10^{-3}) \text{ m}^2$
$K - 1.93(10^{-11}) \text{ m}^2$	$L_{\text{eff}} - 35.56 \text{ cm}$
$C_e - 109 \text{ J/oC}$	$L_c - 10.16 \text{ cm}$
$L_e - 10.16 \text{ cm}$	$d_w - 2 \text{ cm}$
	$N - 100 \text{ in}^{-2}$

power inputs. The liquid front recedes from its initial position, corresponding to a partial dryout of the wick. In most cases, the front reverses direction and returns to its original position, corresponding to a complete rewetting of the wick. The recession of the liquid front occurs when the rate of evaporation of liquid is greater than the maximum liquid flow-rate that the capillary pumping can supply. Reversal of the liquid-front movement occurs when the capillary pumping is sufficient to supply more liquid than is depleted through evaporation.

Experimental Investigation

Experimental Setup

To examine the transient phenomena exhibited during pulsed start-up, tests were performed utilizing a simple screen wicked

copper/water heat pipe. The heat pipe shell is 45.72 cm (18 in) in length, with a 2.22 cm (7/8 in) inner diameter and a 0.165 cm (0.065 in) wall thickness. The wick is formed from 4 layers of 100-mesh copper screen which were wrapped on a mandrel and inserted into the shell so as to conform to the inner diameter.

Heat input to the pipe was provided by an Inconel-sheathed, nichrome heater wire coiled around the 10.16 cm (4 in) long evaporator section. Electrical power input to the heater was provided by a regulated dc power supply. Forced-air cooling was supplied by a squirrel-cage fan. A schematic of the test is shown in Fig 12. Temperatures were measured with copper/constantan thermocouples at eight locations. Wall temperatures, ambient air temperature and power input rate to the heater were monitored and recorded with a data logger.

The two types of pulsed start-up tests performed were those with and without thermal energy storage in the heat pipe. For those tests with thermal energy storage, the condenser section was 10.16 cm (4 in) in length. For those tests without thermal energy storage, the condenser section was 20.32 cm (8 in) in length.

Heat losses from the apparatus were reduced by wrapping the heater and transport sections with ~ 6 cm of ceramic fiber insulation and 3 layers of foil radiation shielding. Heat losses were estimated at less than 10% of the power input to the heater.

Experimental Verification of Capillary Limit

The capillary limit for the water heat pipe used in this study is shown in Fig 13. This curve is calculated from the following equation for the capillary limit:

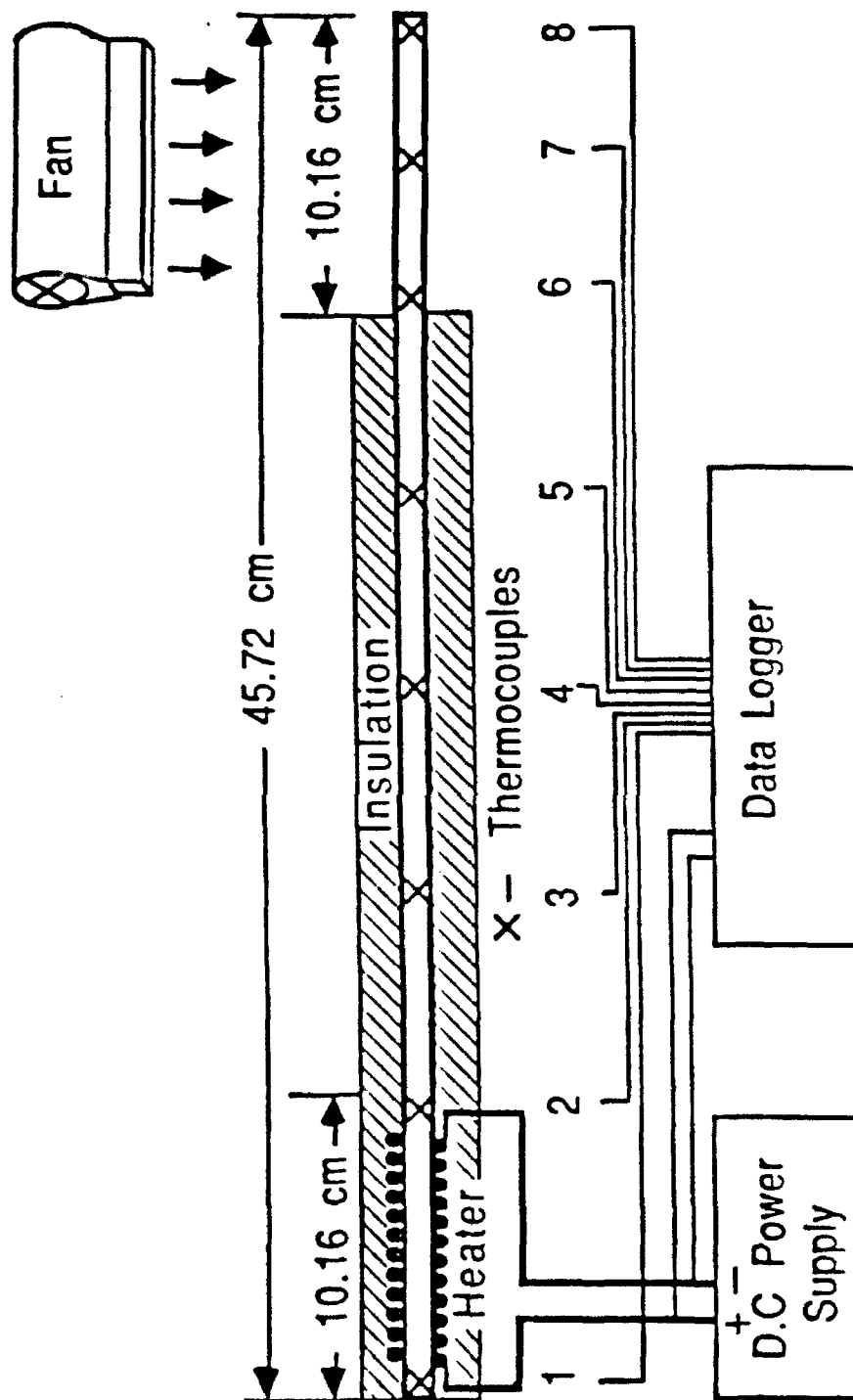


Fig 12 Heat Pipe Test Setup

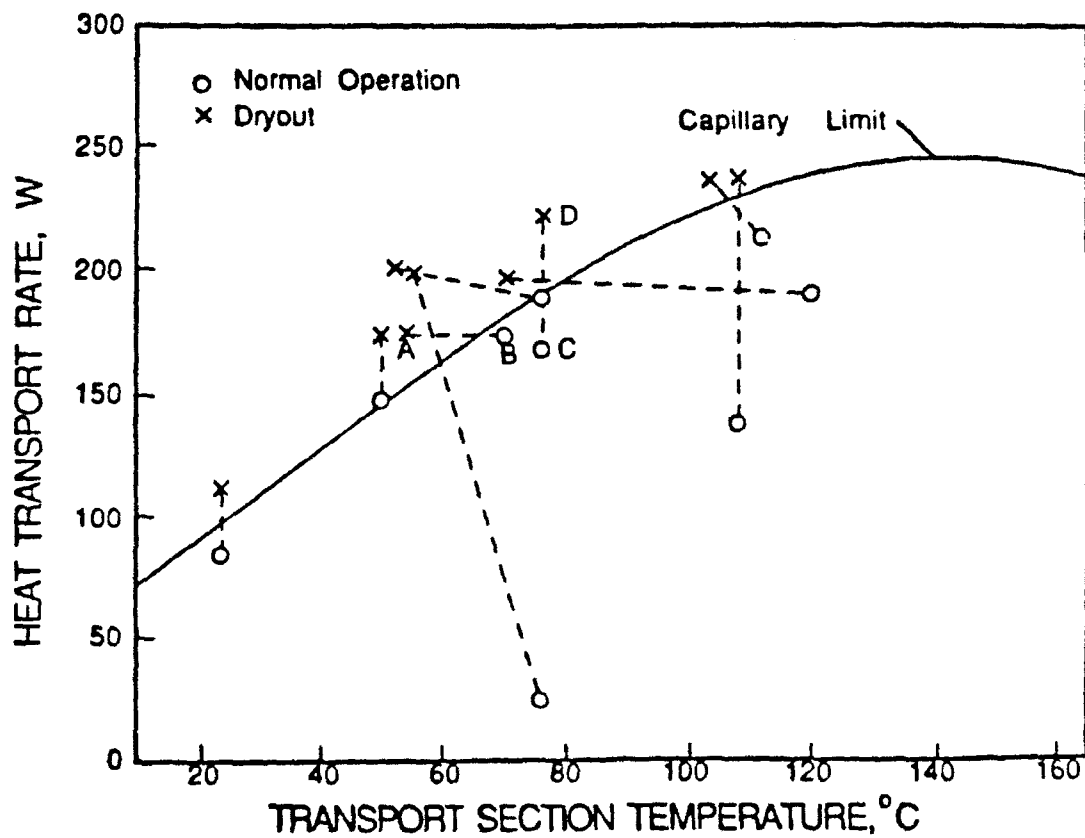


Fig 13 Verification of Capillary Limit

$$Q_{\max} = \frac{4\sigma N - \rho g d_w}{F_{\ell} L_{\text{eff}}} \quad (22)$$

where $F_{\ell} = \frac{\mu_{\ell}}{KA_w \rho \lambda}$ for the case of laminar liquid flow. This equation is a direct result of assuming Darcy flow with a linear pressure distribution in the liquid and ignoring the pressure drop in the vapor. Experimental verification of this curve was performed by moving the operating point across the curve at several temperatures by one of three methods. Either the cooling level was increased or decreased while maintaining a constant power input (line AB, Fig 13), or power input was increased while maintaining a constant temperature in the transport section (line CD). Points indicating normal operation correspond with steady-state data. The dashed lines connecting normal operation and dryout points are used only to relate the two points and do not indicate an actual series of operating conditions. Dryout of the evaporator wick was observed as an abnormal increase in the temperature in the evaporator. As is seen by the points indicating dryout in Fig 13, the capillary limit curve is reasonably accurate.

Pulsed Start-Up With Thermal Storage

When the heat pipe temperature changes significantly during the pulsed start-up, a drying of the wick may occur temporarily, followed by rewetting. For these tests, a sudden power input was applied to the heat pipe when it was initially in thermal equilibrium with the ambient and sustained until the pipe was near steady-state temperature. Typical transient temperature profiles are shown in Figs 14 and 15 for two power levels, 125 and 225 W, respectively. At 125 W, the heat-

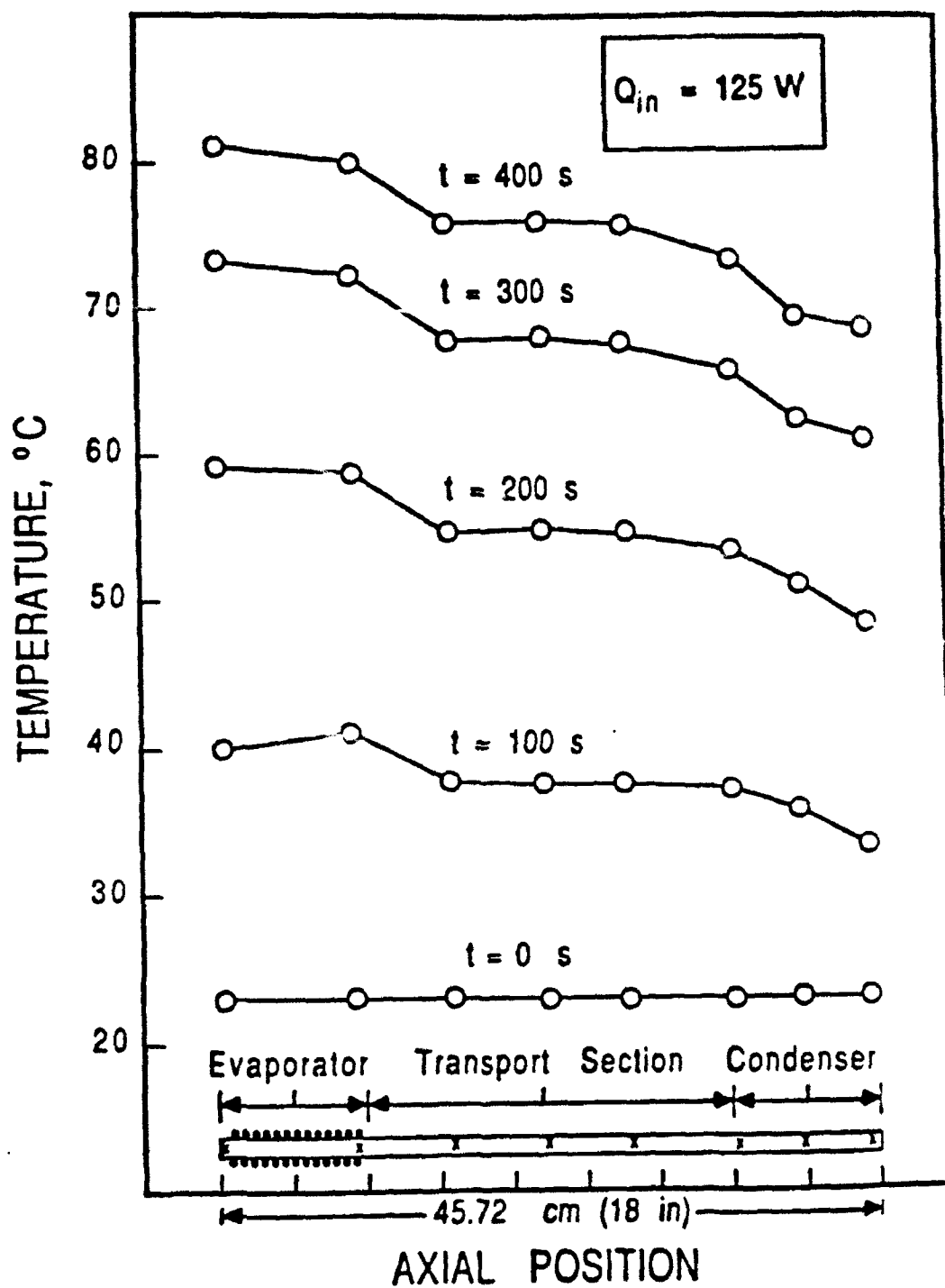


Fig 14 Transient Temperature Profiles ($Q_{in}=125 \text{ W}$)

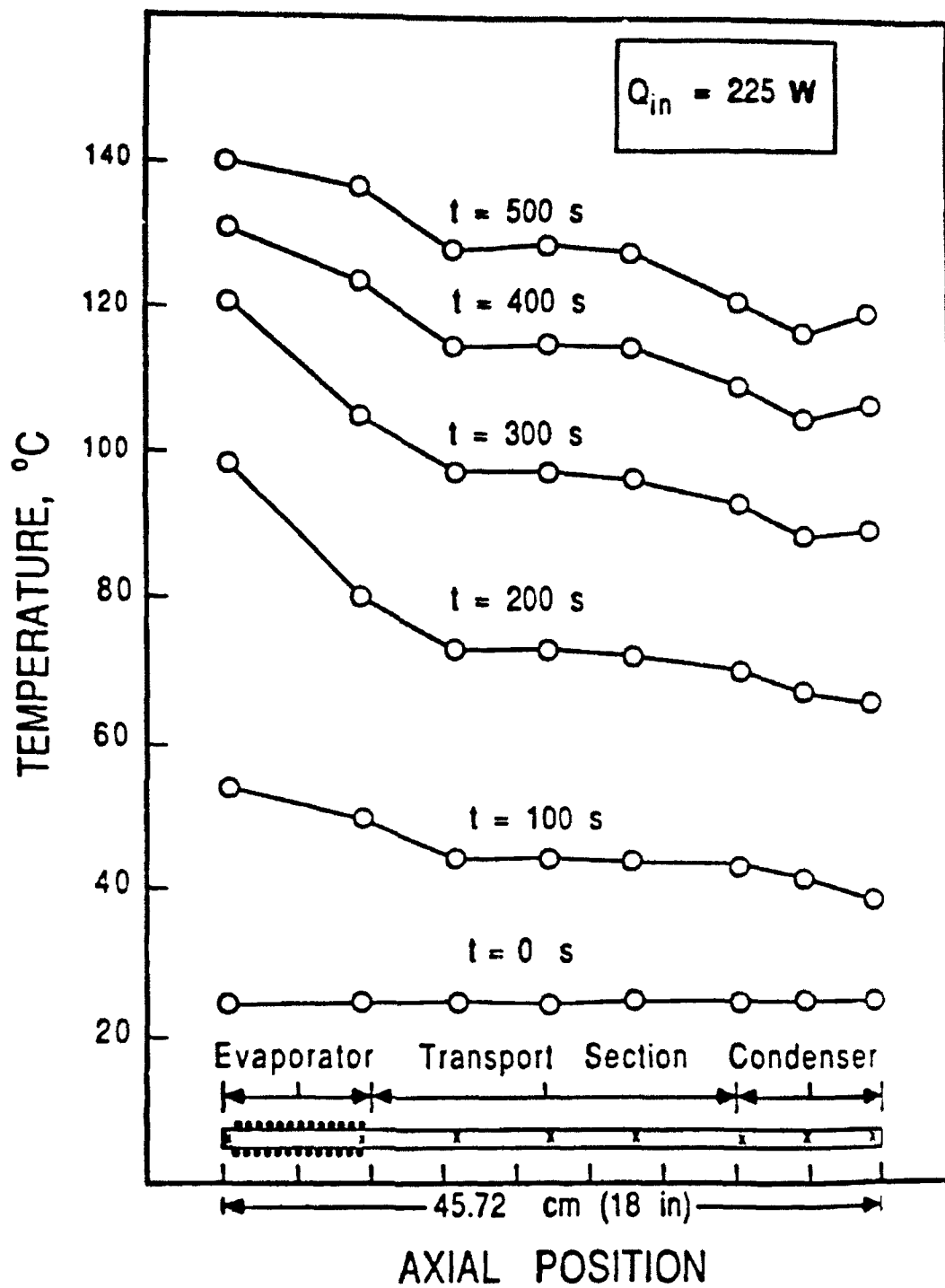


Fig 15 Transient Temperature Profiles ($Q_{in} = 225 \text{ W}$)

transport rate remains below the capillary limit for the entire response period. The heat pipe can transport the heat load without dryout. This is indicated by the absence of large temperature gradients in the evaporator. However, at 225 W, the heat-transport rate temporarily exceeds the capillary limit and a partial dryout occurs. A large temperature gradient exists across the evaporator at 200 seconds. Rewetting of the wick is exhibited as a decrease in the temperature gradient at 500 seconds.

Drying and rewetting of the wick are also shown in Fig 16 for two heat-input rates. Outside evaporator and inside evaporator refer to temperatures measured by thermocouples 1 and 2, respectively (see Fig 12). When the outside temperature increases more quickly than the rest of the heat pipe, it is because this region is partially dry. Without liquid supply in the region, the local evaporative heat transfer is reduced. The reduction in heat transfer requires that some of the additional thermal energy be stored, which raises the temperature in the region. It is seen that the magnitude of the dryout increases with heat flux. This is caused by either an increase in the size of the dried region, an increase in the thermal energy storage in the dry region, or both.

Pulsed Start-Up Without Thermal Storage

Pulsed start-up tests with negligible thermal storage were performed to verify that the liquid flow in a screen wick can respond quickly to a change in pressure gradient. Without thermal storage, the heat pipe must immediately transport the entire heat load to the condenser. If the transport limit is exceeded, the wick will not rewet

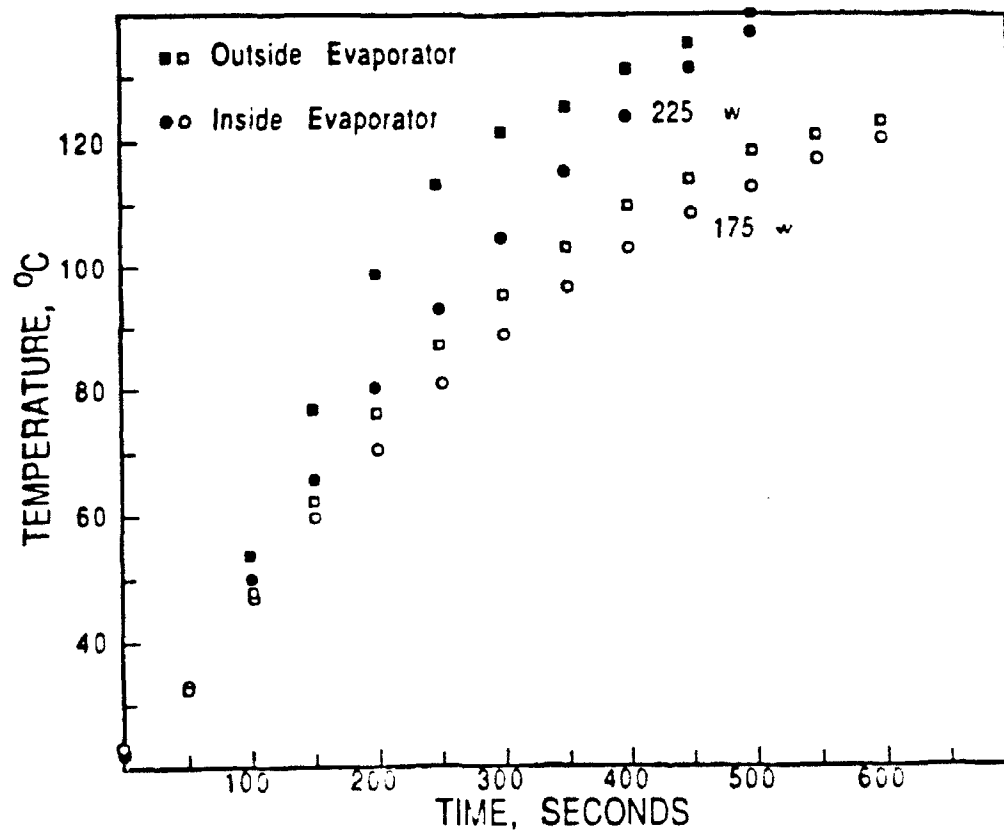


Fig 16 Pulsed Start Up with Thermal Storage

itself but will continue to dry out as long as the power input is maintained.

Pulsed start-up without thermal storage was accomplished by applying a sudden power input to the heat pipe via the electric resistance heater and varying the cooling rate so that the transport section remained at the same temperature. For these tests, the condenser section was 20.32 cm (8 in) in length to accommodate a radiant heater used only to raise the heat pipe temperature uniformly prior to a test. The tests were conducted at four different initial temperatures. At each temperature, power inputs above and below the capillary limit were applied.

For tests performed at room temperature, the radiant heater was not used, and cooling was accomplished by a combination of forced air and cold-water drip. The drip rate was increased gradually to maintain the transport section at room temperature. For the elevated temperature runs, the condenser of the heat pipe was surrounded by a clamshell-type radiant heater so that the entire pipe could be heated uniformly. When the heat pipe was isothermal at the desired elevated temperature, the clamshell heater was quickly removed. The desired pulse load was applied at the evaporator and the condenser was cooled by forced air. Cooling level was varied by changing the distance of the fan from the condenser.

Dryout was observed only for those pulses which exceeded the predicted capillary limit to heat transport at the given pulse temperature. The tests verify that the liquid flow can respond quickly to a change in pressure gradient.

Comparison of Results

Analytical results as shown in Fig 11 are similar to experimental results shown in Fig 16. Both show a drying of the wick and rewetting due to increasing liquid return flow. Both indicate a more substantial dryout of the wick at higher heat fluxes. The time required for the wick to rewet is on the order of several hundred seconds. Rewetting time is somewhat longer in the experimental data and is nearly independent of heat flux. Theoretical results indicate that no rewetting will occur for pulses of 225 W or greater, while the experimental results show rewetting for 225 W. The flat-front nature of the liquid flow model requires that the wick begins to dryout immediately after the pulse is applied. Any depletion of liquid will cause dryout, i.e., the liquid front recedes along the wick. In the actual heat pipe, some depletion of liquid in the evaporator wick can occur without causing dryout. Increased thermal storage in the dry region of the wick is ignored in the model because only the average heat pipe temperature given by the lumped parameter solution is used in the transient liquid model. The dryout in the heat pipe will thus occur more slowly and the heat pipe will reach higher temperatures. This explains the observed rewetting of the wick at 225 W.

Saturation Dependence of Liquid Flow

The transient response depends on the capillary pumping, the mechanism of cooling, and the heat capacity of the heat pipe. Three

possible responses to a pulsed power input can occur. The wick in the evaporator may either accommodate the heat input without dryout, dryout partially followed by rewetting, or dryout without rewetting.

Predictions of the dryout and rewetting behavior were made using a lumped parameter model and fair agreement with experiments was shown.

Liquid in a screen wick can respond almost instantaneously to a change in pressure gradient. This is verified by the ability of the heat pipe to transport a pulsed heat load equal to the capillary limit without dryout while maintaining the heat pipe at a constant temperature.

The major shortcomings of the flat-front liquid flow model are its failure to allow for the variation of saturation with axial location. The actual capillary pressure developed by the wick and the permeability will vary with the saturation and thus with axial location. The maximum capillary pressure which is used in the model is a limiting value. In the actual heat pipe, the capillary pressure will vary between zero and this maximum value. The flat front is a simplification that is probably approached only in extreme cases of dryout. The actual conditions are then decidedly more complex, and a higher level of sophistication is required for a more accurate model.

Possible modifications must take into account the variation in saturation, and relate this to the local capillary pressure. A crude approach was first taken, by modeling the pores in the wick as a bundle of circular capillary tubes. This allowed, through geometrical considerations, development of an expression relating the capillary pressure to the amount of liquid in the wick. However, as expected, the results of this approach were extremely inaccurate. This is because the

porous structure develops the capillary pressure in a different manner than a simple capillary tube. The reduction in amount of liquid required for the maximum pumping to be developed can be significantly different.

The only reasonable approach left was the empirical determination of the saturation dependence of the flow properties. This approach was expected to be difficult because of the need for saturation measurements in a thin layer of porous wick. The following chapters describe the development of the experimental technique, the measurement of the flow properties and the development of the liquid flow model.

Chapter 3.

SATURATION MEASUREMENT IN HEAT PIPE WICKS

The present chapter describes direct saturation measurement techniques. The problem of measuring the saturation in the screen wicks is far from trivial, and only a few previously published studies involving saturation measurements in actual heat pipe wicks were located. This chapter also describes the system installed for obtaining saturation measurements and the design of the heat pipe which allows direct saturation measurements during operation.

Continuous Saturation Model

In the previous Chapter, it was determined that a detailed model of the liquid flow in the heat pipe wick was necessary to obtain more accurate and detailed predictions of transient behavior. The capillary pumping and permeability which control the local movement of liquid in the wick were both known to be functions of the amount of liquid present locally, or the saturation. Based on this knowledge it was felt that in a realistic model, the saturation dependence of the liquid flow could not be ignored. This hypothesis was supported by the extensive research efforts to model fluid flow in geological formations.

Although the simplified model provided useful information, it is important to obtain a more detailed understanding of the mechanisms involved in transient response of a heat pipe. The actual heat and mass transfer processes occurring in the heat pipe wick during transient operation are undoubtedly more complex than those of the simplified model. At the very least, the detailed model must account for the

saturation dependence of the capillary pumping and permeability.

Because the geometry of the screen wicks are complex, these properties must be determined experimentally even for the fully saturated case. To model accurately the saturation dependence of these properties requires a difficult experimental determination of the saturation dependence of the flow properties. If the detailed local model is to be useful for modeling heat pipe behavior, it must first be compared with experiment. Thus a detailed measurement of the liquid movement in the wick of an actual heat pipe during operation is also necessary.

Saturation measurements in heat pipes have been made in the past using radiography. However, these measurements were all limited to the case of steady-state operation. Moss and Kelly [6] imaged water in a thick, stainless-steel mesh wick, including the area in which evaporation took place. Merrigan et al. [20] imaged lithium working fluid in a heat pipe using neutron radiography. Shishido et al. [8] also measured saturation distributions in a heat pipe with wicks of glass spheres or crushed brick powder using an electrical capacitance technique. Several studies have used X-ray radiography to measure steady saturations in geological formations [22,23,24].

Real-time neutron imaging techniques are still under development and these present the most promise for imaging of water and lithium in metal heat pipes during transient operation. Recent advances have been made to allow a reduction in the required neutron intensity [25]. X-ray radiography is generally not as useful because most metals attenuate X-rays strongly while most liquids attenuate X-rays very weakly.

Alternative Methods

Several methods of obtaining direct measurement of the saturation in a heat pipe wick were considered. The relative difficulty and merits of each of the methods were assessed. A major consideration was whether a given method could be implemented while still utilizing an apparatus which resembled an actual heat pipe in operation. The different alternatives which were considered are outlined below. Advantages and disadvantages of each method are discussed.

Neutron Radiography

Neutron radiography is an excellent candidate for imaging of particular fluids enclosed within metal containers. This is a result of the very high absorption of thermal or "slow" neutrons by fluids such as hydrogen, water and lithium. Neutron images of water and lithium heat pipes have been used successfully in the past to determine position of the liquid working fluid [6,20]. These were steady-state operating conditions. To obtain satisfactory measurements under transient conditions would require either very large fluxes of neutrons or improved methods of detection with higher sensitivity to neutrons. Real-time neutron imaging is still in the developmental stages, and high neutron fluxes are impractical. A pulsed nuclear reactor located at General Atomic Inc., San Diego CA, was considered for transient imaging. However, exposure times of the order of 1 second were not considered attainable. Thus neutron radiography was ruled out as a viable candidate for transient measurements. It was also considered impractical for numerous steady-state measurements because of the

complexity of the required equipment.

Capacitance

Capacitance measurements have been used to measure working fluid distribution [8] in a specialized heat pipe. They have also been used to track the wicking height as a function of time in a copper screen wick [3]. This method relies on the change in capacitance between two electrodes produced by the presence of a dielectric fluid. This method allows good transient response because the instantaneous capacitance values are measured. It is difficult to obtain detailed local measurements with this technique because it would require many electrodes within the heat pipe. The major problem is the requirement that the wick must form a nonconducting path. This requires the use of dielectric materials for the wall, wick and working fluid. The dielectric wall materials are poor conductors of heat and thus would not be representative of actual heat pipes.

Attenuation of Laser Beams

This method would allow local, transient measurements to be made in a very specialized heat pipe. The method would require transparent wall and wick materials. The probable boiling which would occur in the wick with low-temperature working fluids would seriously affect the accuracy of such a measurement. Vapor bubbles in the wick would provide many reflecting interfaces oriented at arbitrary angles to the incident beam, making accurate measurement of liquid amounts impossible.

Ultrasonic Waves

This method would involve reflection of high frequency acoustic waves from the liquid/vapor interfaces within the wick. It would allow very good sensitivity even with thin layers of liquid. However, because it involves reflection of the waves from liquid/vapor interfaces, the method would suffer the same limitations as the laser attenuation method regarding boiling or vapor bubbles in the wick.

X-ray Radiography

This method has been utilized to image fluids in a porous structure [22]. Because of the low attenuation of X-rays by most liquids, the method does present difficulties. Conventional heat pipe wall materials such as steel, copper and aluminum attenuate X-rays much more than the working fluid. However, if a weak attenuating wall and wick material were selected, an accurate measurement of the working fluid distribution could be obtained.

X-ray Diffraction

X-ray diffraction has long been used for the measurement of thin coatings on metals [26]. The collimated beam of X-rays is directed at an angle onto the surface and is partially reflected from the substrate material. The beam is attenuated as it passes twice through the coating material. This method could be applied to measuring liquid amounts within a wick. Disadvantages of the method include both: a) low diffracted intensity, requiring longer counting periods in order to obtain a statistically significant number of quanta; and b) difficult to extend to simultaneous measurements over an area, because a separate

counting device is required for each point measurement.

Experimental Evaluation of X-ray Techniques

Based on overall criteria for the measurement technique, the two X-ray techniques were selected for further study. Important aspects to the selection were insensitivity to vapor bubbles in the wick, transient capability and relative cost/availability of necessary equipment. The two methods were evaluated experimentally using mock-up samples of heat pipe wick and wall materials.

X-ray Diffraction:

To evaluate the feasibility of X-ray diffraction for obtaining saturation measurements in a heat pipe wick, small samples of wicking material clamped to a flat copper substrate were used. These samples were placed in the holder of a Philips X-ray diffraction unit. Diffracted X-ray intensity was scanned over a small angle of incidence about the Bragg angle of the copper substrate. The Bragg angle corresponds to the incidence angle resulting in the maximum diffracted intensity. When X-rays incident at this angle enter the material, the photons diffracted from the first few layers of the atomic lattice structure leave the structure in phase. The scans were performed for three cases, a bare substrate, a substrate covered by a dry wick, and a substrate covered by a wick either partially or fully saturated with water. Sample results are shown in Fig 17. It can be seen that the working fluid in the wick causes a significant decrease in the diffracted intensity which is measured at the scintillation detector. This decrease is due to the attenuation of both the incident and

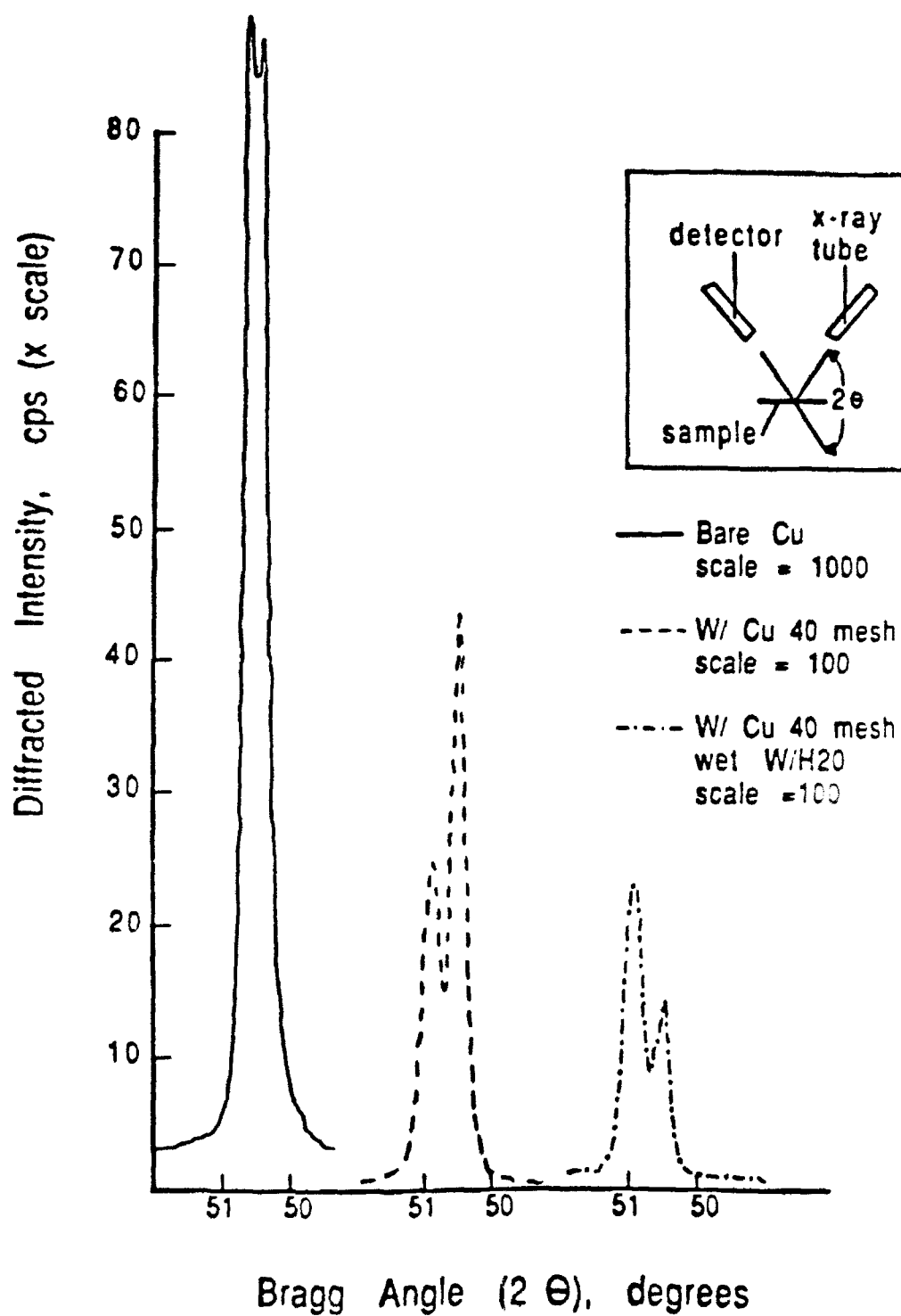


Fig 17 X-ray Diffraction Results

diffracted beams by the working fluid, and the intensity reduction could be calibrated against known thicknesses of working fluid. The measurement area, corresponding to the X-ray spot size at the wicking sample, is of the order of 1 mm^2 .

X-ray Radiography

To evaluate the use of X-ray radiography for the measurement of saturation in a heat pipe wick screen wick samples were placed between flat samples of wall materials. The samples were then radiographed under various conditions of saturation and various X-ray energy, intensity and exposure times. It was found that imaging of water was poor for most metallic screens unless they had a large percentage of open area. Also, steel and copper wall materials attenuated too strongly to be of use. Successful imaging of the working fluid was performed with synthetic mesh wicks of teflon, polyester and polypropylene, provided the wall material was a weak attenuator. The thickness of the wick samples used for the experiments was of the order of 1 mm. Graphite and aluminum wall samples were used and the attenuation measured in thicknesses of aluminum was of the order of 0.1 mm.

After successful imaging of the working fluid in the synthetic wick materials, more radiographs were obtained in the vertical wicking mode. For these tests, the wick samples were placed in a vertical position and the lower end was placed in a pool of working fluid. The X-ray tube was rotated to point horizontally at the sample and radiographs were taken. The resulting radiographic film was scanned using an automatic recording microphotodensitometer. This device passes a beam of light through the

film and records the optical density as a function of position. Fig 18 shows the graph resulting from such a test. One prime advantage of the radiographic technique is illustrated here. This is the ability to obtain a picture which contains local information over an area of interest. The plot is significant because it yields the saturation as a function of capillary pressure. The saturation profile is obtained by calibrating with radiographs of known thicknesses of working fluid. Because the pressure gradient in the liquid is hydrostatic, the capillary pressure is a linear with height.

Selection of Measurement Technique

Of the alternative methods described previously, four could be used to obtain saturation measurements in a wick structure, given the distinct likelihood of boiling heat transfer in the wick. These are: neutron radiography, X-ray radiography, X-ray diffraction and capacitance. Neutron radiography was found to be impractical due to the complexity of the required equipment. It was also determined not to be applicable for short duration, transient measurements and was thus ruled out. The capacitance technique was ruled out for two reasons. First, to obtain detailed saturation measurements would require a distributed system of many capacitance sensors. This would limit the detail of the saturation measurements and complicate the overall hardware involved. Second, the technique requires the use of dielectric wall and wick materials. These materials are also generally poor conductors of heat and thus are unrepresentative of most actual heat pipe materials.

The two remaining methods were evaluated experimentally and found to work. X-ray diffraction was not selected because of the difficulty

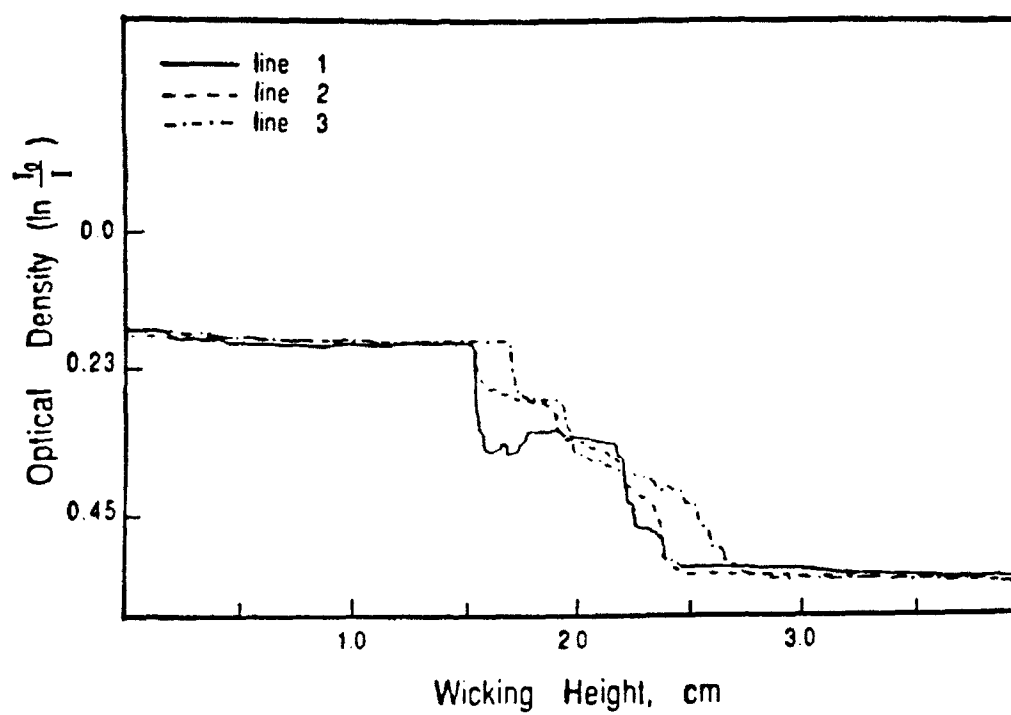


Fig 18 Optical Density Data

associated with overall measurements using this techniques. As described in the previous section, the method could give only point measurements as a function of time, instead of the desired measurements as a function of both position and time. To obtain many point measurements over the wick area would require an extremely elaborate apparatus.

After considering the relative merits of the aforementioned methods for obtaining the transient saturation measurements, X-ray radiography was selected as the simplest and most feasible for obtaining saturation as a function of both position and time.

System for Measurement of Saturation using X-Ray Radiography

Development of the liquid flow model relies on measurements of saturation distributions in heat pipe wicks. Preliminary investigation using this method utilized the X-ray facility located at the Air Force Materials Laboratory. It was desirable to develop a system which could be dedicated full time to this effort, and which was more suitable for the low-energy radiography used for imaging liquids. For these reasons, a facility was developed at UK specifically for the measurement of saturation in heat pipe wicks. This section describes the various components which include an X-ray tube and power supply, radiation shielded chamber, X-ray shutter system and X-ray film digitizing system.

Selection of X-ray Equipment

Several experiments involving saturation measurements were

performed using X-ray equipment located at the Air Force Materials Laboratory. From these experiments the energy requirements of the X-ray source were well defined. All of the early work was accomplished with X-rays produced at an operating tube voltage of 12 to 25 kV. This energy level is well below the rated limits of the various machines which were available at the Materials Laboratory. An X-ray source better suited to these low energy levels was purchased. The Kevex model K3052S X-ray tube operates at 5-30 kV and 0-6.7 mA tube current and hence is ideal for low-energy X-ray imaging.

During evaluation of the various options for X-ray systems, a real-time X-ray imaging system was also evaluated. There are many advantages to the use of real-time X-ray imaging instead of conventional X-ray radiography. Because the image may be digitized and stored using a digital video device, the saturation measurements are not only continuous in time but position also. The tedious process of scanning radiographs with a photodensitometer would be unnecessary.

The disadvantages to using real-time X-ray imaging are losses of resolution and cost. The loss of resolution was not considered to be of major importance to the present study because resolution of fine details is unnecessary. However, cost proved to be a deciding factor. A real-time system uses an image intensifier which is quite expensive (\$10,000-\$20,000). In addition, the intensifier will not operate effectively at X-ray energies below 30 kV. This put the system at the upper limit of the useful range of energies for the present study. In all, the real-time system would cost at least twice as much as the conventional system. Because the proposed work involved many steady-state measurements, the additional expense of the real-time

system could not be justified.

Transient measurements are obtained using conventional radiography by taking multiple exposures at very low exposure times. Good results have been obtained with exposure times as low as one second using direct exposure film.

X-ray Radiography System

Before receiving the X-ray tube and power supply from Kevex, a lead-lined chamber was fabricated. This was necessary so that the X-ray tube could be operated in the existing laboratory room without subjecting workers to unsafe radiation levels. The chamber is shown in the diagram in Fig 19. It consists of a steel chamber with a single latched door and a secure feedthrough. Safety measures include approximately 1 mm of lead shielding over the entire exterior, a safety interlock on the chamber door and a red warning beacon on the top of the chamber. Two positions for the X-ray tube have been used, to provide either a horizontal or vertical beam. A lead shutter system is employed to provide very accurate control of the exposure time. This removes the initial transient increase in power associated with the power supply. Once the X-ray source has been activated, the power source takes anywhere from 10-40 seconds to reach the set power level depending on power level. Since the exposure times are sometimes of the order of seconds, to achieve accurate exposure times the X-ray tube should be operating at the desired power level at the start of the exposure period. Details of the shutter system are shown in Fig 20. The two lead shutters are driven by a stepping motor, which is controlled by a computer. Exposure time is set using the onboard clock of the computer. For each exposure

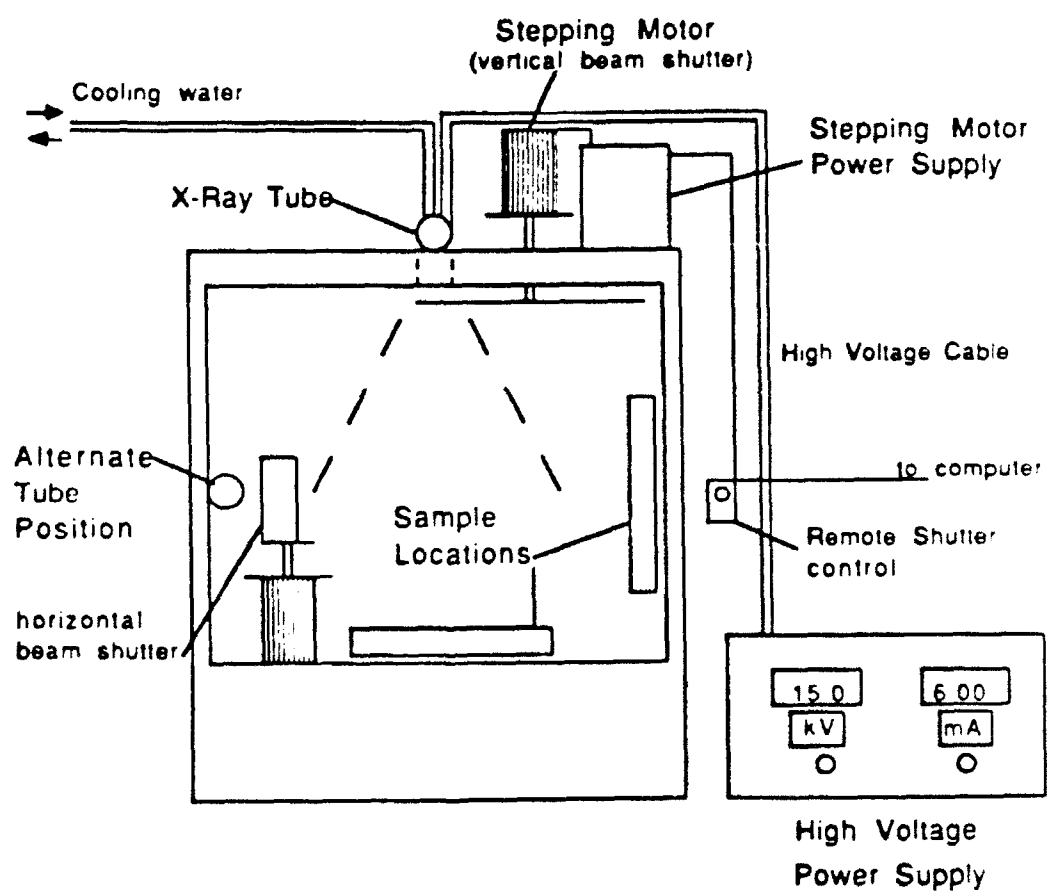
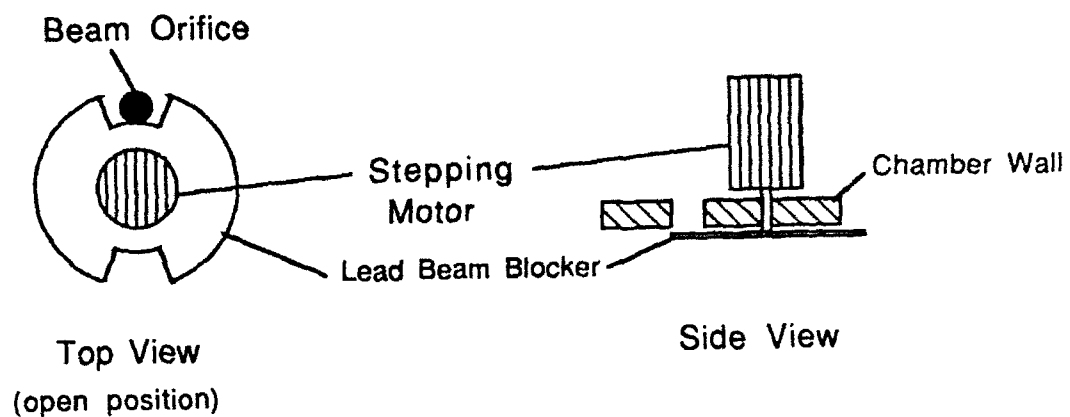
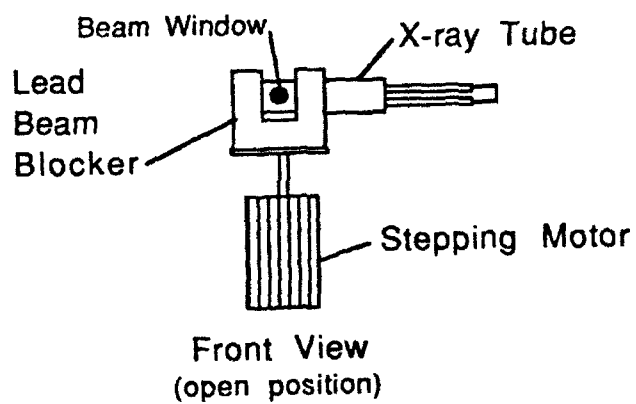


Fig 19 X-ray Chamber



Vertical Beam Shutter



Horizontal Beam Shutter

Fig 20 X-ray Shutter System

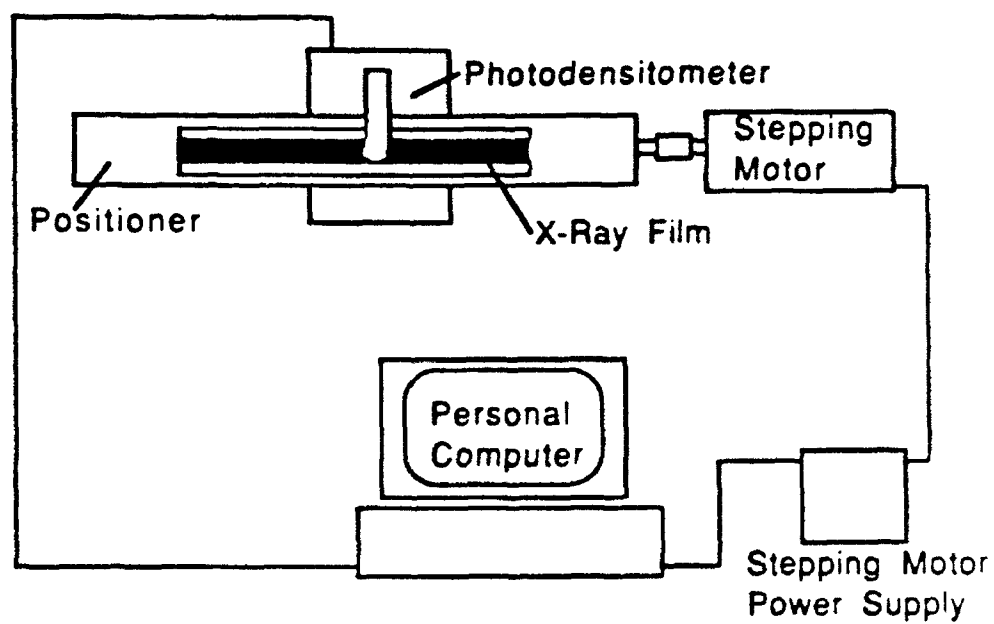
the X-ray tube is allowed to operate at the desired constant power level and then the shutter is activated by a remote switch.

X-ray Film Digitizing System

In preliminary work saturation values were obtained using either a automatic recording microphotodensitometer located at Wright-Patterson Materials Laboratory or a manual photodensitometer at the University of Kentucky. Because it is desirable to obtain optical density values for as many locations as possible on each of many films, partial automation of the system was deemed necessary. The photodensitometer at UK was already equipped with a RS232 communications port option. An x-y positioner for the film was fabricated to be used with the photodensitometer. The x-axis motion of the positioner is controlled by a stepping motor, which is driven by a data acquisition and control board on a personal computer. A schematic of the system is shown in Fig 21. Since the size of the films is 12 in x 1 in, the one axis automation is sufficient. The computer program positions the film along the x-axis, reads the optical density from the photodensitometer and then repeats with a variable distance increment. After a complete scan along the 12-in length of the x-direction, the manual y-direction positioning mechanism is advanced one increment, and the scan is repeated. An average scan consists of a 0.1 inch by 0.1 inch grid and approximately 150 readings per 3 inch section of film.

Calibration of Saturation Measurement

The saturation measurement must account for the variation of transmitted intensity with the thickness of material penetrated. For a



Film Digitizing System

Fig 21 Film Digitizing System

given exposure time, the optical density of the exposed film is a measure of the intensity of the radiation incident on the film. This is the radiation intensity transmitted through the sample. However, because the radiation is not monochromatic, the attenuation coefficient is not a constant value. A rigorous calibration would require measurement of the optical density of the film for many known values of the saturation at each location on the film. This is impractical in the present experiment. However, an abbreviated procedure was undertaken. Radiographs were obtained for each wick structure in both the fully saturated and dry conditions. The saturation at each point was calculated from:

$$S = \frac{D_d - D_{ps}}{D_d - D_{fs}} . \quad (23)$$

The values of the optical density were taken from the location of interest on the three films. This procedure is equivalent to assuming that the attenuation coefficient can be approximated as linear over the range of transmitted intensities of the experiment. To verify this assumption, measurements were obtained of the variation of the optical density with thickness of liquid layer penetrated. These show that the deviation from linear behavior is not large and thus the above assumption is valid. Details of the uncertainty introduced through the use of this calibration procedure are given in Appendix A.

Heat Pipe With Saturation Measurement

Because part of the proposed effort was comparison of the detailed liquid flow model with measured saturation distributions in an actual heat pipe, the saturation measurement technique and the heat pipe must be compatible. The X-ray radiography method imposes rather severe requirements on the wall and wick materials. Because of the extremely low attenuation of X-rays by most liquid heat pipe working fluids, low energy X-rays must be used to image them successfully. These low energy X-rays would be completely absorbed by common heat pipe wall and wick materials. Beryllium was determined to be a useful material for the heat pipe wall. Beryllium is an exotic metal used for X-ray windows in X-ray sources. It is extremely transparent to X-rays because of its low atomic number (#4). It is also quite brittle, but recent advances in the hot vacuum pressing technique of forming very pure metal powder into solid stock have produced a material with very high strength and moderate elasticity. Use of beryllium for the wall material, with its extremely low attenuation of X-rays and high thermal conductivity (roughly one-half that of copper), would satisfy the most important requirements imposed on the heat pipe wall material. The other consideration is compatibility with the working fluid. Limited data are available for compatibility of beryllium with water, showing it to be resistant to corrosion by very pure water. A working fluid desirable for the present study is Freon, which is chemically inert and thus probably will not react with beryllium at the low temperatures involved.

The wick material must also be relatively transparent to X-rays. Two materials were determined to be suitable wick materials for use with

X-ray saturation measurements. The first is synthetic meshes of polyester and polypropylene. These materials are geometrically identical to the wire meshes commonly used for heat pipe wicks. The use of synthetic wicks, which possess relatively low thermal conductivity, would appear to be unrepresentative of most heat pipe applications. However, Phillips et al. [27] have shown that the thermal conductivity of fluid-saturated, layered screen wicks is relatively insensitive to the thermal conductivity of the solid material of which the screen is made.

In order to maintain a planar wick using multiple layers of the synthetic mesh wick materials, retaining springs of some form are necessary. Sewing the layers of the wick structure together increases the likelihood of uniform contact between layers. Therefore, the mesh wick structure used in the heat pipe was sewn together at many locations. By using a very fine needle and polyester thread finer in diameter than that composing the wick material, it was possible to sew the wick while minimizing deformation of the pores.

A second material initially selected for use was porous graphite. The porous graphite material, like the synthetic meshes, is commonly used for purposes of filtration. A range of pore sizes and permeabilities was found to be readily available. The porous graphite material has the additional advantage of being mechanically rigid, which allows a more uniform geometry when placed in the actual heat pipe. The porous graphite materials were later found to possess capillary properties significantly different from the more common mesh materials. The difference is a result of the degree of interconnectedness of the pores. For this reason these materials were not used.

Chapter 4

DETERMINATION OF CAPILLARY FLOW PROPERTIES

This chapter describes the experimental determination of the properties of capillary pressure and relative permeability. Three types of experiments were performed: steady-state wicking rise, transient wicking rise and steady flow. The steady-state wicking rise gives both the rising and falling capillary pressure distributions. The transient wicking rise gives allows calculation of the relative permeability. The steady flow experiment gives a more direct measure of the relative permeability, but is a more complicated experiment.

Although much information has been published on the flow properties of wick materials, relatively little information can be found regarding the saturation dependence of P_c and K_r . Fluid flows in wicks are generally modeled by assuming a fully saturated structure (constant properties).

Because the capillary pressure depends on saturation, surface tension, contact angle and wick geometry while relative permeability depends on saturation and wick geometry alone, it is desirable to separate the two flow properties and study them independently.

Wicking Rise Experiments

An experimental study of the saturation dependence of the capillary pressure and permeability in mesh wicks has been conducted. Both transient and steady state wicking tests were performed. The key

feature of these experiments is the use of X-ray radiography for the measurement of saturation.

The wicks were radiographed using the 30kV, 6.7 mA Kevex tungsten target X-ray source (tube voltage set at 15 kV). The saturation distributions were determined using the special digitizing system described in Chapter 3. Saturation measurements were taken on a 2.54-mm by 2.54-mm grid, and then averaged in the direction perpendicular to the pressure gradient. This yields an entire capillary pressure/saturation curve from a single test.

The wick materials used were all square mesh synthetic fabrics obtained from Tetko, Inc. Their relevant properties are given in Table 2. The wick structures were formed by pressing several layers of material tightly between two flat beryllium plates. This was required to maintain the wicks in a planar geometry and ensure good contact between layers of wick material. Two points need to be addressed concerning the geometry of the wick structures so formed: clamping pressure and boundary influence.

Table 2. Wick Properties

Material Type	N, in^{-1}	$d, \mu\text{m}$	$\delta, \mu\text{m}$	$K, \times 10^{-10} \text{m}^2$	ϵ	$w, \mu\text{m}$	n
polypropylene							
5-280	58	160	320	7.88	0.7	280	5
polyesters							
HC7-200	84.7	100	165	4.18	0.73	200	12
HC7-85	203.2	40	67	0.74	0.73	85	25
HC7-51	302.4	33	65	0.26	0.68	51	25

Clamping Pressure

To provide a uniform structure, each multilayer wick was clamped with approximately 5-10 pounds of force over the approximately 77 cm² area. The pressure exerted on the layers was enough to press them tightly together but not enough to cause significant deformation of the fibers as determined from subsequent examination. The beryllium plates are extremely rigid and were clamped in several locations to ensure a uniform pressure. In previous attempts spacers were used to provide a uniform thickness of the clamped wick. The obvious choice for this spacing was the total thickness of the layers. However, when the space between the plates was made equal in thickness to n times δ , it was found that the wick layers were still somewhat loose and pockets of gas would be trapped in the open spaces. This occurs because the layers tend to intermesh and occupy less space. When the layers were clamped together, a much more uniform structure was obtained as evidenced by the equilibrium distributions of liquid and gas in the structures.

Influence of the Wall

The present wick geometry (bounded on both sides) is different than that in a heat pipe, where the wick is bounded on only one side by a solid surface. The other side is usually open to provide for vapor escape. However, it is felt that the influence of the wall on the flow properties can be neglected in the case of a multilayer wick structure with uniformly clamped layers. Most wick structures are constructed of multiple layers in order to provide sufficient flow area. The influence of the boundary on flow is known to be confined to a very small region near the wall. In Darcy flow, the momentum boundary layer is of the

order of $\sqrt{K/\epsilon}$ [28]. For the wicks used in the present experiment, this value is of the order of 10 μm or less (less than 0.1% of the wick thickness). In addition, the effective pore size is not thought to be significantly changed by the presence of the additional wall. The pumping is controlled by the smallest voids in the mesh material in which two-phase interfaces are present. The size of such voids depends mainly on the filament diameter and spacing of the filaments. It is commonly assumed that reductions in saturation in a mesh wick occur by a uniform recession of the liquid/vapor interface into the first layer of the wick. Saturation measurements made during the present work show that in the actual wick the interfaces are irregular and the nonwetting phase penetrates deep into the wick structure at various locations. Thus the nonwetting phase is more evenly distributed over the cross section of the wick. The mesh structure is not perfectly uniform (at the micron scale) and liquid recession occurs more readily at some locations than others. For this reason the macroscopically observed wick properties depend much more on the wick material than on the boundary conditions or number of layers. This is similar to the case of a uniformly random porous packing of sand in a container. If the walls of the container do not alter the packing geometry, then they have little, if any effect on the capillary properties of the bulk material of the bed.

Steady-State Tests

The steady-state wicking apparatus is shown in Fig 22. A closed system was utilized to minimize the effects of evaporation of the liquid on the final equilibrium distribution. The design is similar to that

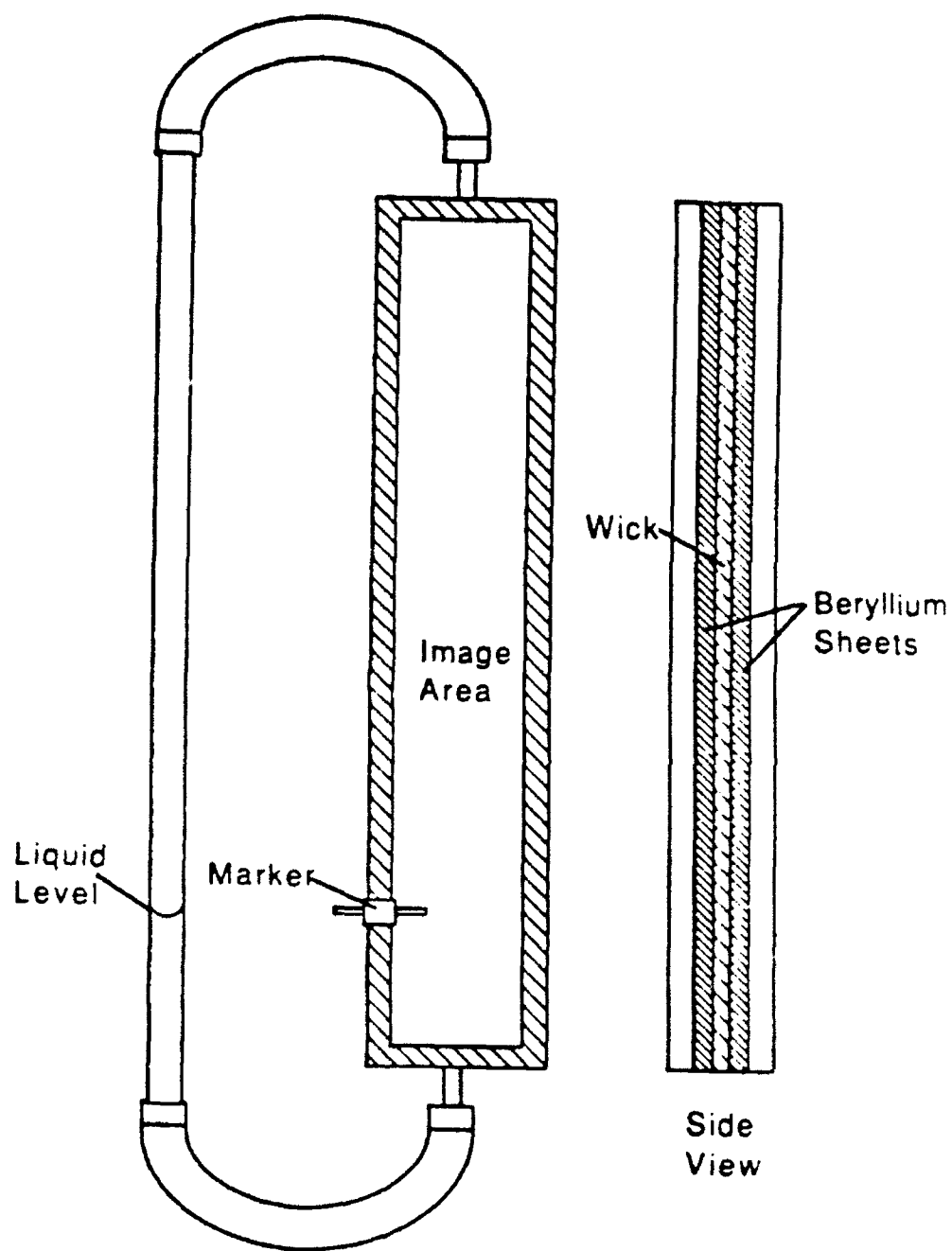


Fig 22 Steady-State Wicking Apparatus

used by Shibayama and Morooka [29] with the addition of the saturation measurement. A metal marker was used to show, on the radiograph, the location of the free liquid interface in the glass tube. For each test, the wick was cleaned in acetone, rinsed with methanol filtered through a 0.2- μ m filter and dried with filtered air. It was then assembled into the holder and the beryllium plates were sealed in place with silicone sealant.

The nonwetting phase for the steady-state tests was a mixture of air and methanol vapor. An equilibrium concentration of vapor would be reached in the apparatus within a short period of time, after which evaporation would become negligible.

The steady-state tests were to be performed with Freon 113 because of its stronger attenuation of X-rays. However, Freon 113 was found to be incompatible with the sealant, so doped methanol was used in its place. The methanol was doped with a small amount (0.0375 g/ml) of potassium iodide to increase X-ray absorption. Rise tests were conducted in capillary tubes to verify that the small amount of impurity has a negligible effect on surface tension and contact angle.

Rising Case

A radiograph was taken of the assembly with a dry wick. Liquid was added to the glass tube. More liquid was added as necessary to maintain the liquid level in the glass tube. Equilibrium was assumed to have been reached when the liquid level in the tube stopped falling, and another radiograph was taken to determine the rising saturation distribution. The duration of the steady state tests was of the order of 1 hour. After the test, the wick was completely filled and a

radiograph was taken of the fully saturated wick.

Falling Case

A radiograph was taken of the dry wick. It was then filled completely with working fluid. Another radiograph was taken to calibrate for the fully saturated case. Then a substantial portion (about 50-60%) of the liquid was poured out. As the liquid redistributed itself under the force of gravity, the liquid level in the tube rose. Equilibrium was reached when the level stopped rising and a final radiograph was taken.

Transient Tests

Transient wicking tests were conducted with an open system. The wick structure was placed with one end in a reservoir of liquid as shown in Fig 23. Because of the much shorter duration of these tests (of the order of 1 minute), evaporation is assumed to be negligible compared to the liquid flow rates. The wick layers were clamped between the two beryllium plates, with the sides open to the atmosphere. Each test consisted of placing the wick in contact with a constant head reservoir of liquid at time $t=0$. For the HC7-51 material, the wick was in a vertical position. For the other materials, the wick was inclined at a small angle to the horizontal. Freon-113 was used in the transient tests.

Each radiograph taken during the transient tests yields the saturation as a function of position. The saturation distributions were measured at intervals of 15 to 45 seconds with a 1-second exposure time. The short exposure times were made possible through use of high speed.

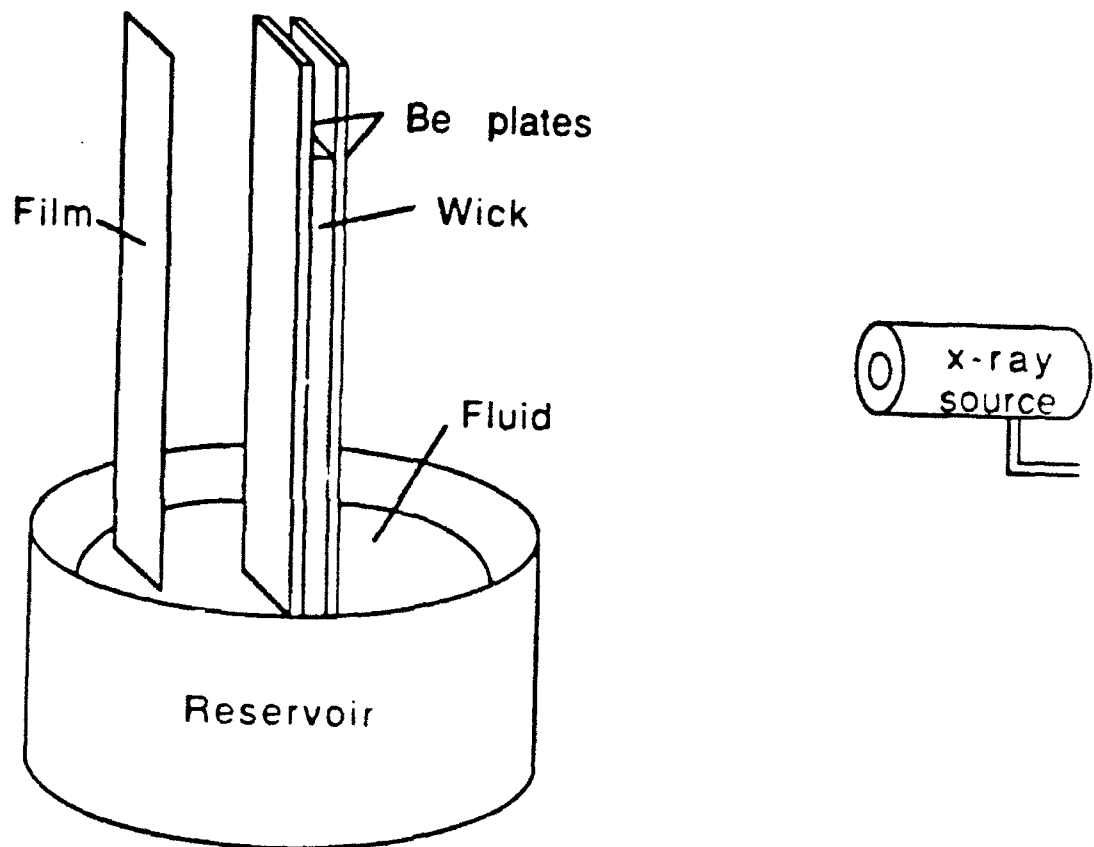


Fig 23 Transient Wicking Rise Test

Kodak direct-exposure X-ray film. The flow in this case is a moving front characteristic of that which occurs when a previously dry wick structure is rewetted with liquid. This behavior is shown in Fig 24. After equilibrium has been established, the pressure gradient is hydrostatic, and the usual curve of static capillary pressure versus saturation may be obtained.

Transient saturation distributions for the four wick materials in Table 1 are shown in Figs 25-28. The angle of inclination to the horizontal is indicated for each material. The time values correspond to seconds elapsed since filling and distances are measured along the wick from the free liquid surface.

The transient saturation curves of the finer mesh wicks (HC7-51, HC7-85) are smoother than those of the coarser wicks (5-280, HC7-200). These wicks behave more uniformly because of the greater number of pores (many layers, small pore size). Because of the lower permeability of the finer mesh, the flow velocity is much less. This increased the distance between the wicking front in the successive images and allowed better resolution. For the 5-280 wick, the wicking front quickly approaches its maximum height. In the present experiment, the successive images could not be obtained quickly enough to show this initial surge.

The present results are in qualitative agreement with measurements of Beam [3] for copper screen wicks. Both show a rapid rise to near equilibrium, followed by a very slow creeping flow. It appears that the shape of the saturation profiles do not change markedly with time. All show a sharp drop in saturation corresponding to the moving front. A much larger saturation gradient is required to sustain the flow at this

Freon-113 in 203 square mesh polyester 15 layer wick.
Vertical wicking rise. Liquid introduced at time $t=0$.
Elapsed time in seconds.

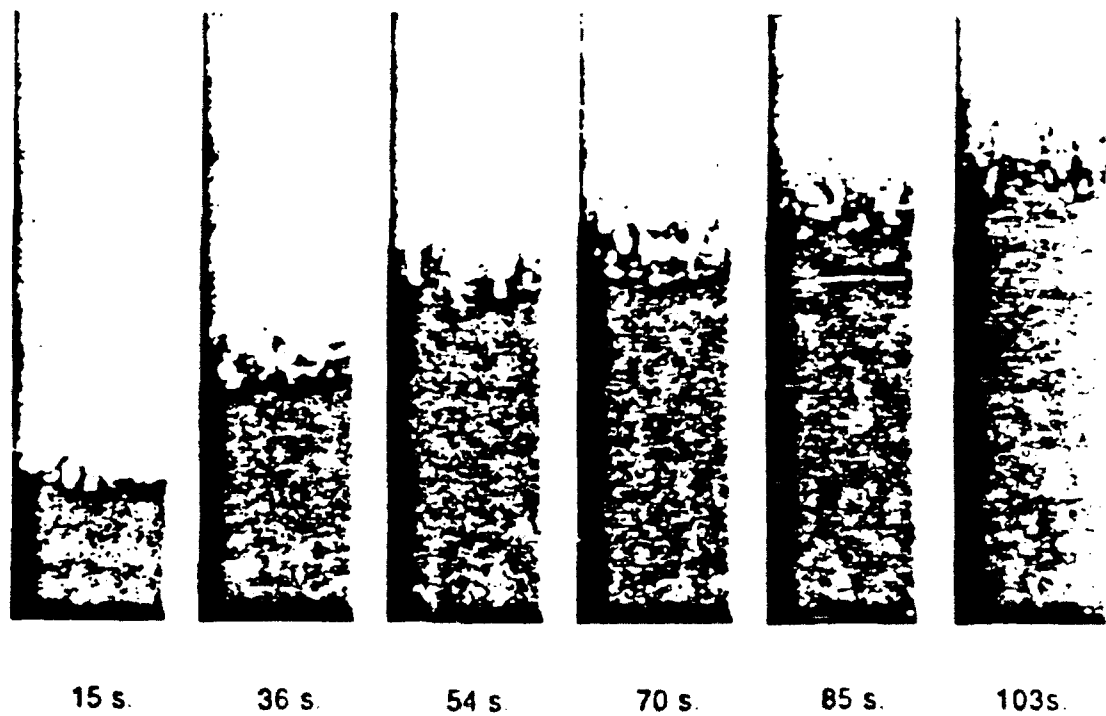


Fig 24 Images of Wicking Front

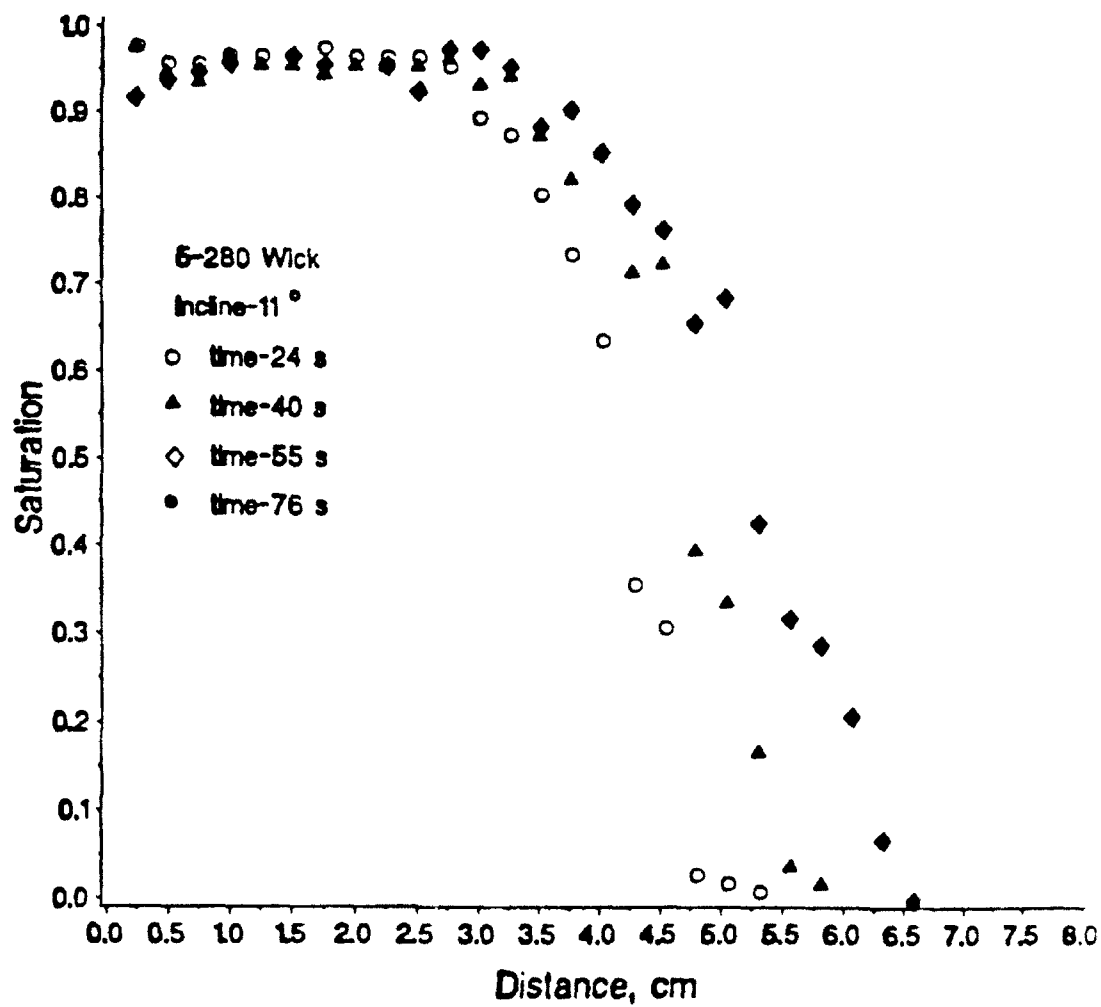


Fig 25 Transient Wicking Rise, 5-280 Wick

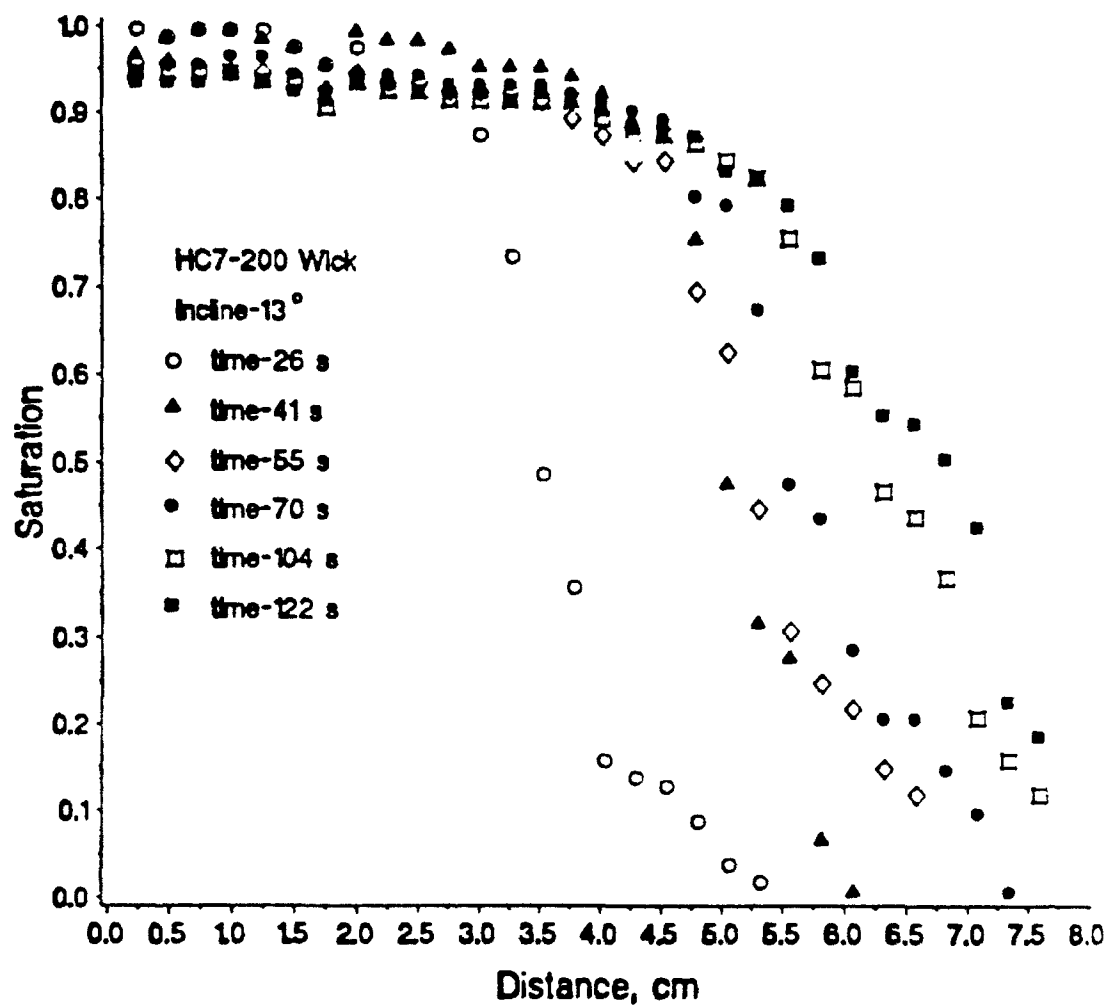


Fig 26 Transient Wicking Rise, HC7-200 Wick

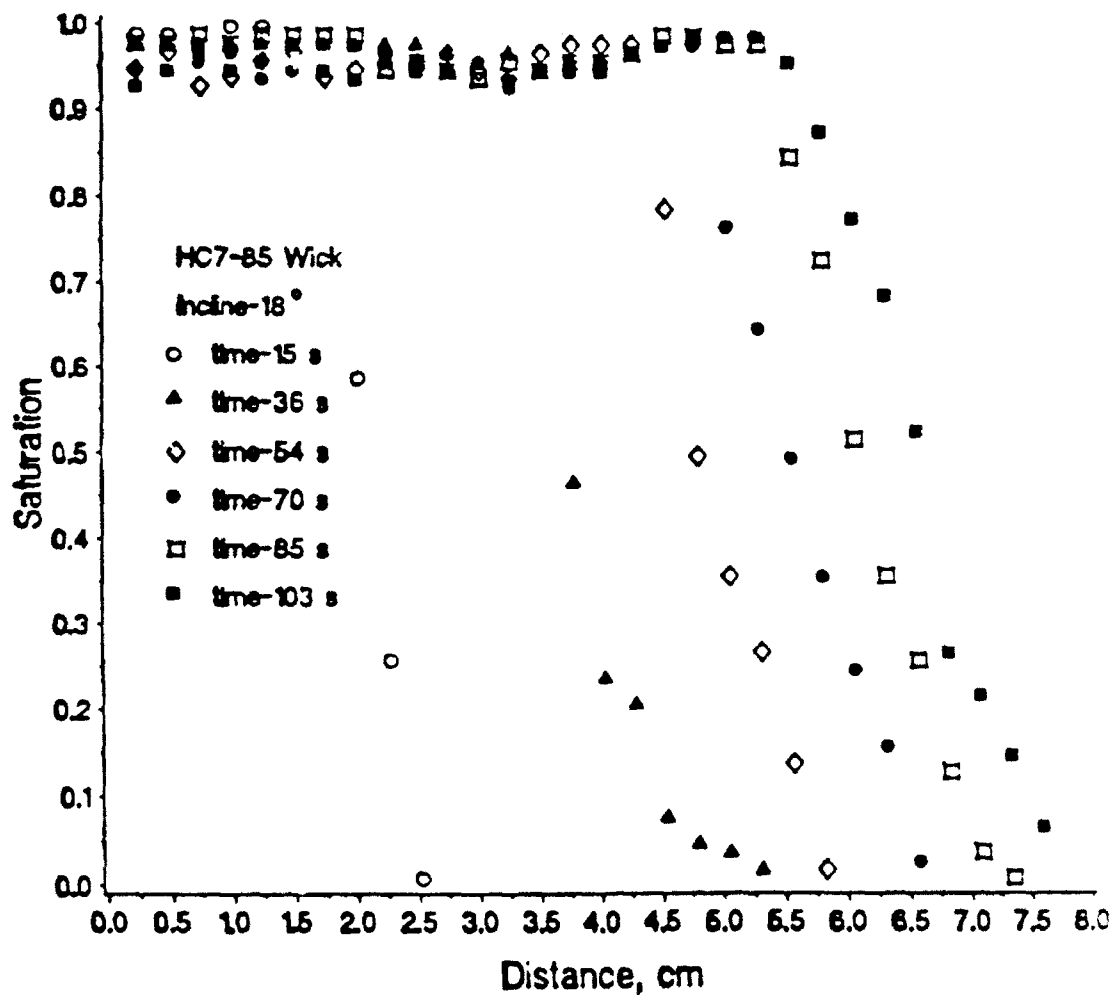


Fig 27 Transient Wicking Rise, HC7-85 Wick

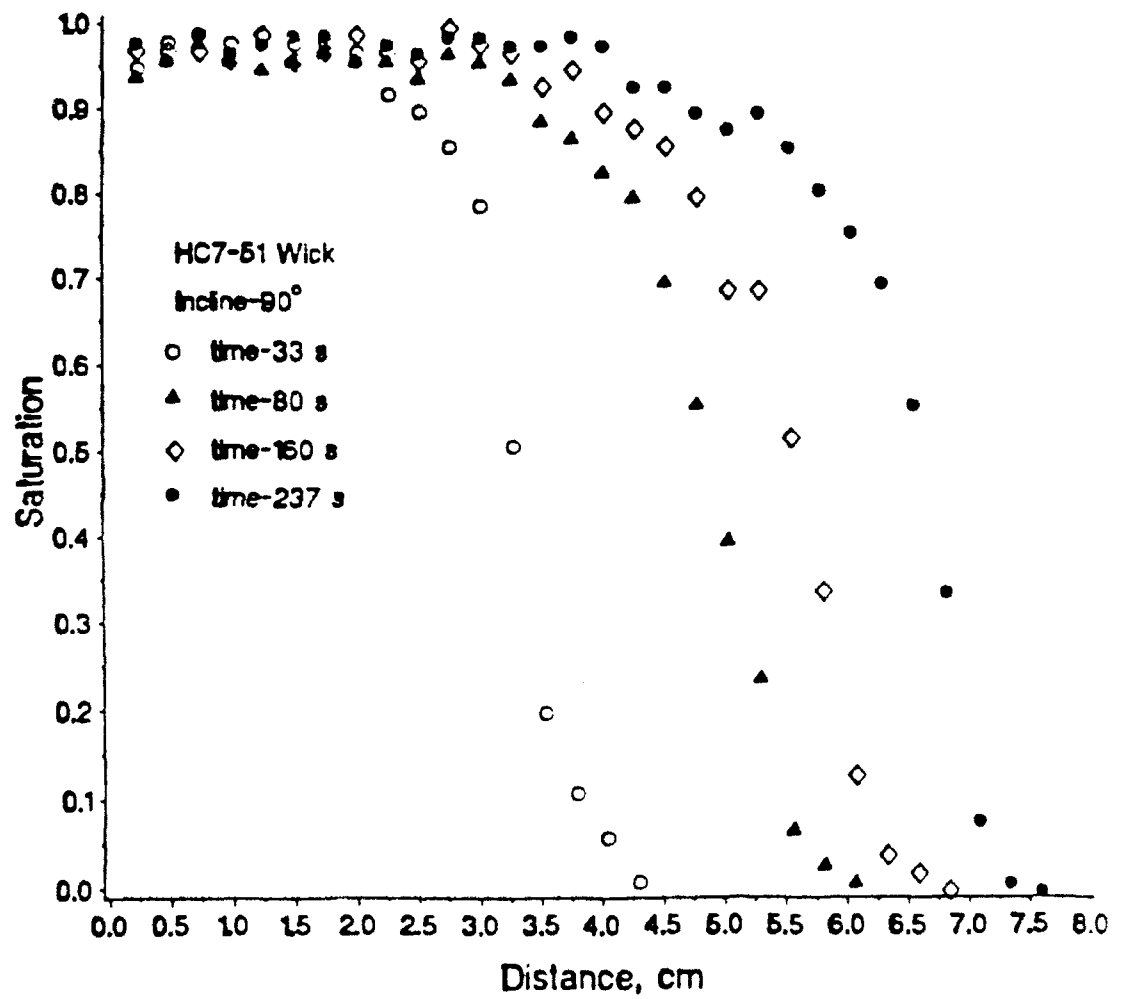


Fig 28 Transient Wicking Rise, HC7-51 Wick

front than in the fully wetted portion of the wick.

Analysis and Discussion of Results

Dimensionless Capillary Pressure

The steady-state data for the four different wick materials of Table 1 are shown in Fig 29. The rising and falling data are shown. These values have been nondimensionalized using the Leverett function [11]:

$$P^* = (P_c/\sigma)\sqrt{K/\epsilon} . \quad (24)$$

The permeability was calculated based on the Blake-Kozeny equation [13]:

$$K = \frac{\epsilon^3 d^2}{122(1-\epsilon)^2} . \quad (25)$$

The porosity is based on the equation of Marcus [13]:

$$\epsilon = 1 - \frac{\pi c N d}{4} \quad (26)$$

where the "crimping factor" c is taken to be 1.05. This value is suggested by Chi [13] for multilayer wicks where the layers are pressed tightly together. Values of full permeability and porosity calculated using Eqs(25 and 26) are given in Table 1.

Further rising data for a metal felt wick [7] and for clean sands [11] are compared with the present data in Fig 30. The good agreement

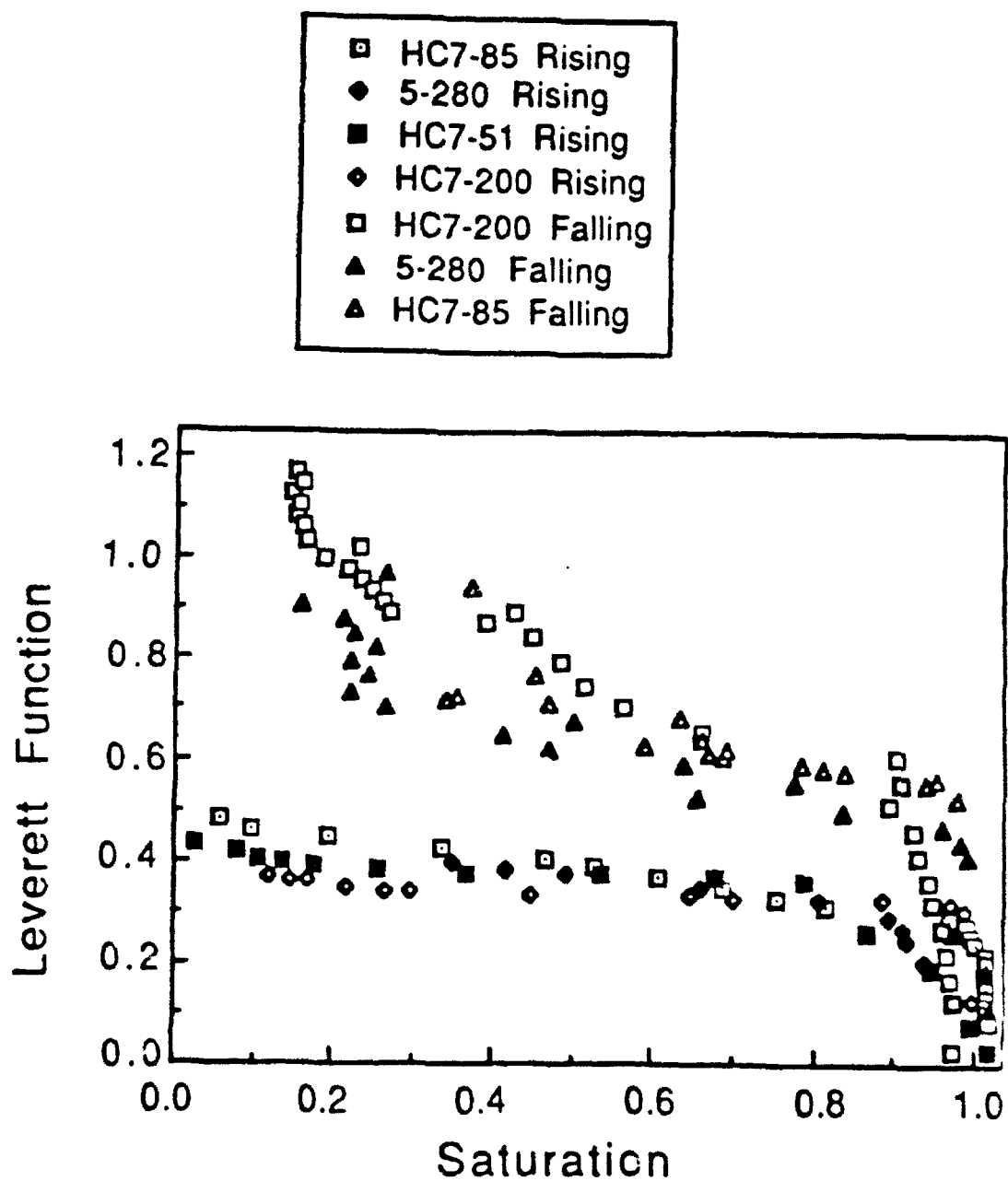


Fig 29 Steady-State Rising and Falling Capillary Pressure

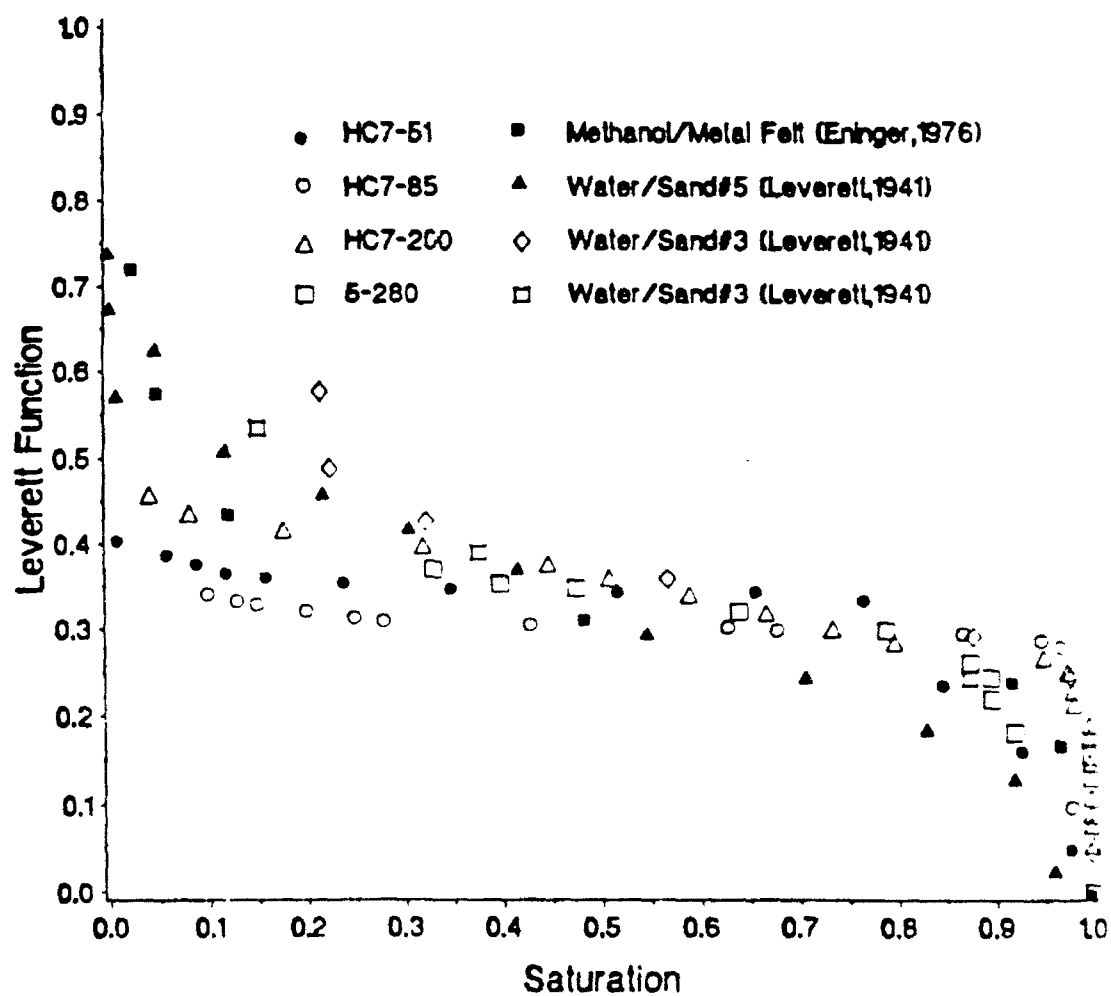


Fig 30 Comparison of Capillary Pressure with Other Materials

for saturations between 0.1 and 0.9 is surprising, given both the differences in geometry of the porous materials and the additional uncertainty introduced by using Eqs(25 and 26). The good correlation of the capillary pressure data means that the relationship can be extended with confidence to other mesh materials without further measurements, provided of course that the contact angle is near zero and the porosity and permeability are known.

Calculation of Relative Permeability

Data for transient saturation distributions given in Figs 25-28 were used to calculate relative permeabilities. In order to obtain the relative permeability from the data, Darcy's law is used:

$$U(x) = - \frac{KK_r}{\mu} \frac{dP}{dx} . \quad (27)$$

Here x is measured along the wick in the direction of the flow, with $x=0$ at the reservoir. In the transient case P is not known directly, so it is written in terms of saturation:

$$P = P_0 - (P_c - \rho g x \sin \gamma) , \quad (28)$$

$$\frac{dP}{dx} = \rho g \sin \gamma - \frac{dP_c}{dS} \frac{dS}{dx} . \quad (29)$$

Here P_0 is the liquid pressure (atmospheric) at the level of the reservoir. The function dP_c/dS is a property of the wick structure and is obtained from a curve fit of the rising data shown in Fig 31. The

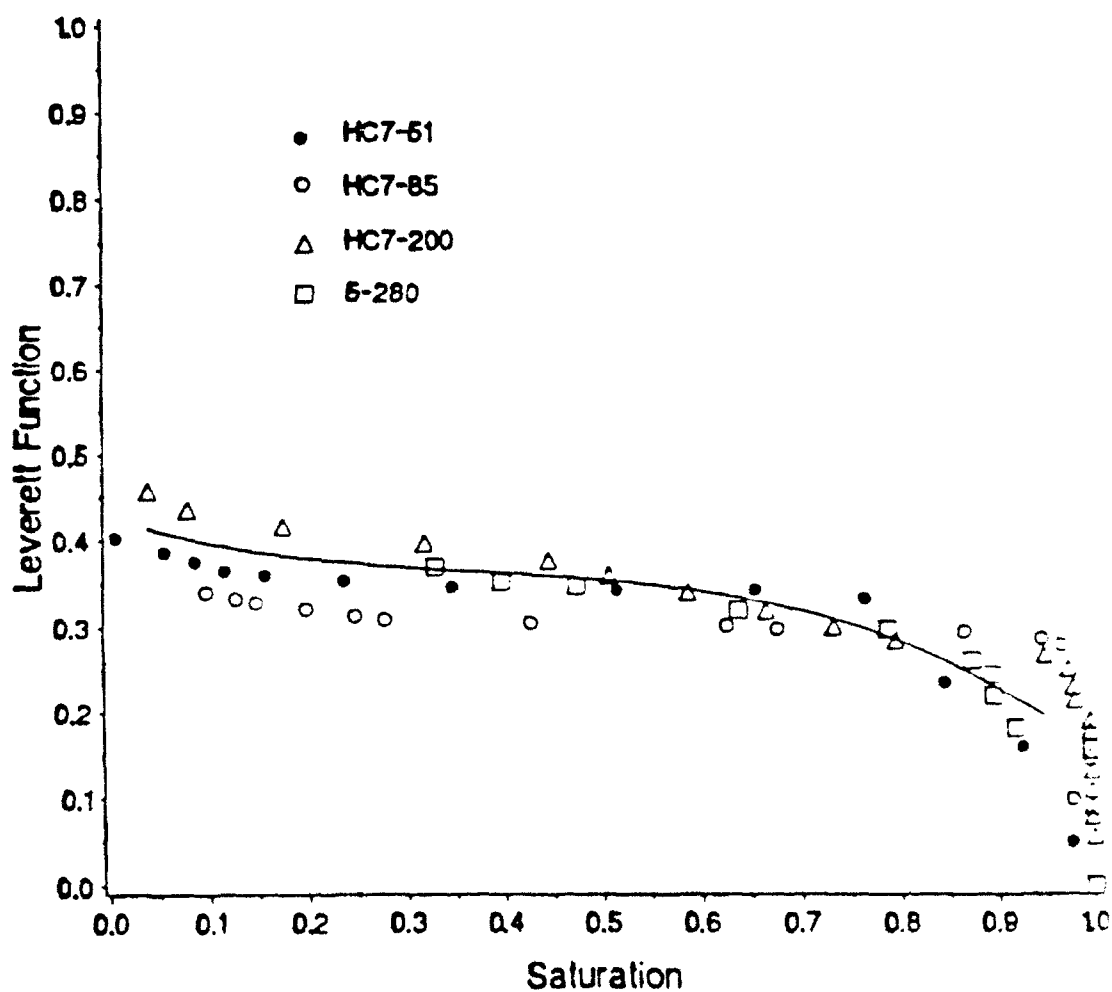


Fig 31 Steady-State Rising Capillary Pressure

saturation gradient and flow velocity are obtained from the transient saturation distributions as follows. Let $S_1(x)$ and $S_2(x)$ represent the saturation distributions with distance at times $t=t_1$ and $t=t_2$, respectively, where $t_2-t_1=\Delta t$. The saturation gradient used in the calculation of relative permeability is:

$$\frac{dS}{dx} \bigg|_{x_0} = \frac{1}{2} \left[\frac{dS_2}{dx} \bigg|_{x_0} + \frac{dS_1}{dx} \bigg|_{x_0} \right] \quad (30)$$

The flow velocity is given by:

$$U(x_0) = \frac{\int_{x_0}^{x_\infty} S_2(x) dx - \int_{x_0}^{x_\infty} S_1(x) dx}{\Delta t / \epsilon} \quad (31)$$

where x_∞ is the position at which $S=0$ and the saturation of interest is $S(x_0) = \{S_2(x_0) + S_1(x_0)\} / 2$. Reynolds numbers based on the velocity calculated from the data and the pore opening are of the order of 0.1. Darcy's law is, therefore, valid in this regime.

The calculated relative permeability is given in Fig 32 as a function of reduced saturation for the four different meshes. The solid line represents reduced saturation to the second power. The dotted lines show the deviation of $\pm 30\%$ from this line. The significant amount of scatter in the data is to be expected because of the uncertainty associated with both the raw saturation data and the calculation procedure. An additional uncertainty is introduced when calculating gradients from the raw saturation data. For a detailed discussion, see Appendix A.

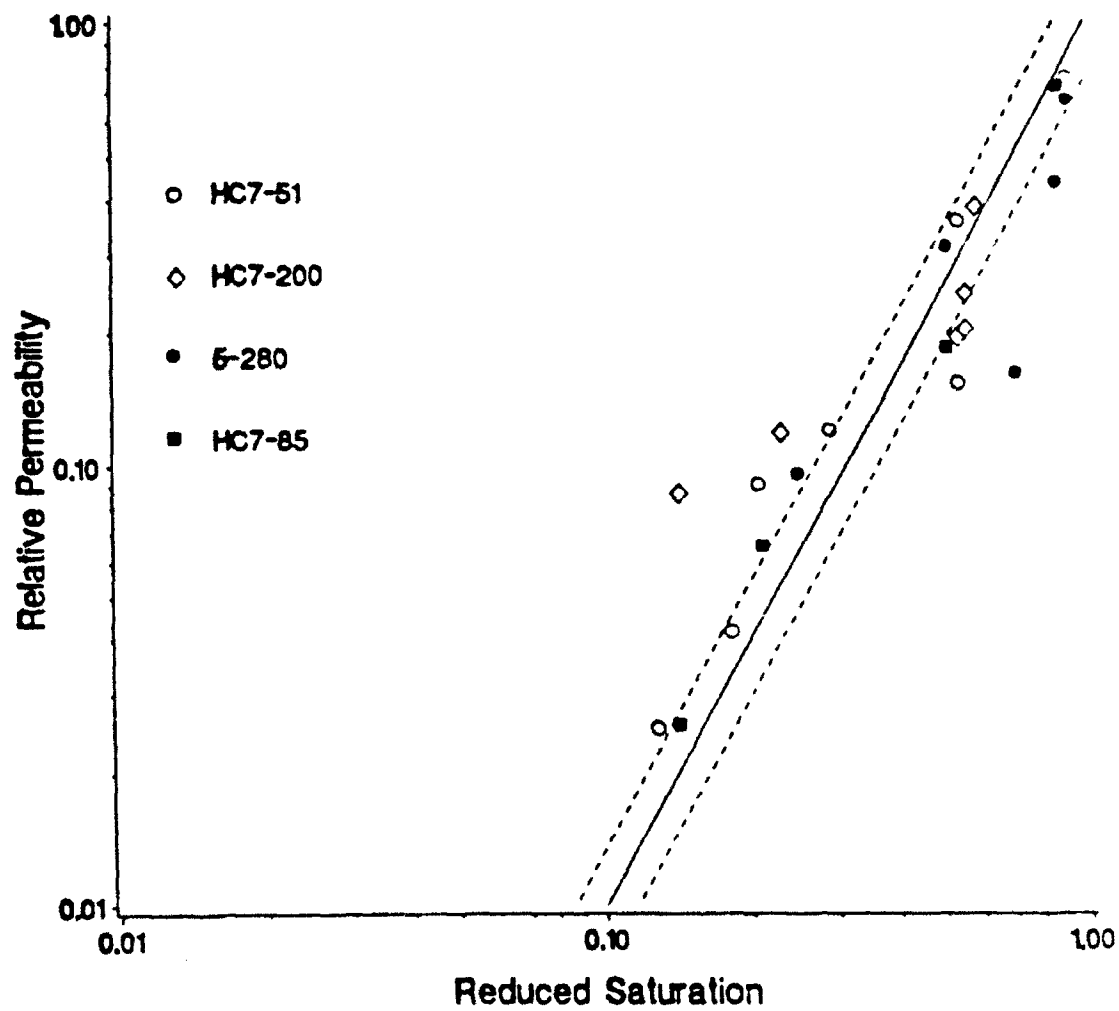


Fig 32 Relative Permeability Calculated from Wicking Tests

The relative permeability values calculated for the HC7-51 and HC7-85 wicks show less scatter than those for the coarser meshes. This is expected because of the nature of the transient wicking curves, discussed earlier. The curves for the finer meshes were smoother and farther apart, allowing a more accurate determination of the relative permeability. Because these results were considered to be more accurate, they were weighed accordingly when the exponent was estimated. The relative permeability data follow roughly the same trend as those for geological materials.

Steady Flow in a Partially Saturated Structure

In order to obtain a direct measurement of the saturation dependence of the relative permeability, an additional experiment was performed. In this experiment, the pressure gradient, mass flow rate and saturation were all measured simultaneously in a capillary flow. A special, two-part wick structure was utilized for this experiment. The two-component wick structure was utilized previously by Eninger [7], who was able to measure slight reductions in permeability, but not saturation distributions. The purpose of the two layer structure is to provide a fully wetted surface at which the pressure taps are joined to the wick structure.

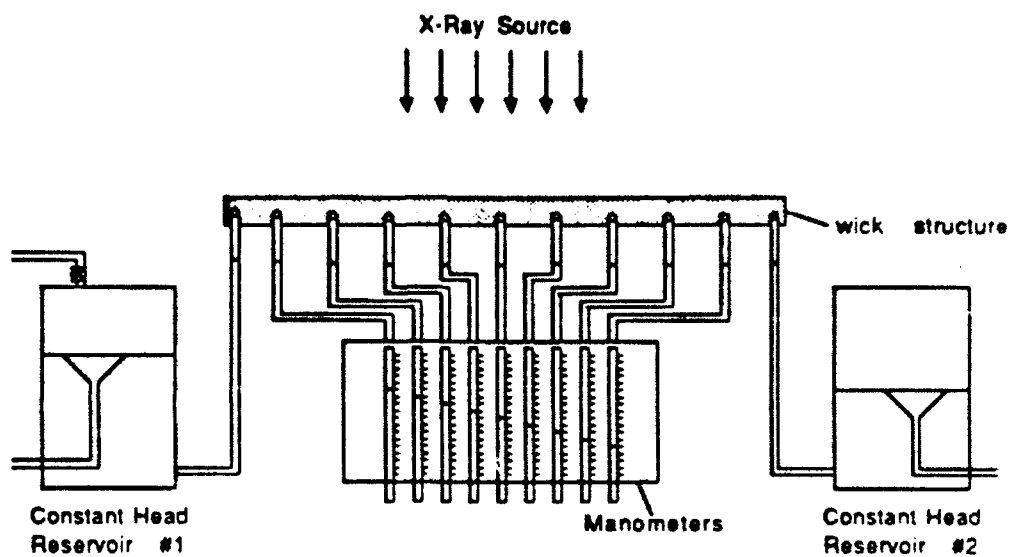
Relative Permeability Experiments

An apparatus was designed and fabricated specifically to obtain direct measurements of the relative permeability in a

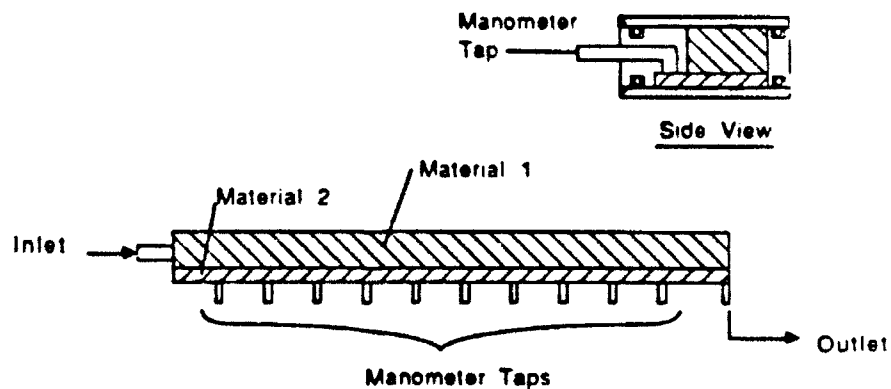
partially-saturated screen wick. These measurements are necessary to verify the validity of the transient wicking rise results. The new apparatus is designed to allow a larger pressure gradient (greater than the maximum capillary head) across the wick structure without depriming the manometer or outlet taps.

The design of the apparatus is shown in Fig 33. Two different wick materials are used to form the wick structure. The upper wick is of larger pore size than the lower wick. As such, it develops a lower capillary pressure. It also has a larger full permeability and a larger cross-sectional area. When an axial pressure gradient is applied across the composite structure, it is the same in both wick materials provided the liquid wets both materials. The flow occurs mainly in the upper wick because of the higher permeability and larger flow area. As the pressure in the outlet portion of the wick structure is reduced, the upper wick will become partially saturated first, because it cannot support the capillary head. The lower wick remains fully saturated because of its higher capillary pumping. Since the manometer taps and flow outlet originate in the lower wick, these remain wetted. Thus the pressure distribution in the partially saturated upper wick may be measured provided the lower wick remains fully saturated.

The total mass flow rate through the composite structure is measured. When both wicks are fully saturated, >95% of the flow is through the upper wick. But as the upper wick desaturates, its permeability becomes lower, and more flow occurs in the lower wick. The relative permeability of the upper wick is given by:



Schematic of Relative Permeability Test



Detail of Wick Structure

Fig 33 Relative Permeability Apparatus

$$K_{1r} = \frac{\frac{\dot{m} \nu}{dP/dx} - K_2 A_{w2}}{K_1 A_{w1}} \quad (32)$$

where the correction accounts for the flow through the fully saturated lower wick of known full permeability.

Saturation measurements are obtained as in the previous experiments by radiographing the composite wick structure. The procedure is slightly more complicated than previous arrangements because of the composite structure. Instead of radiographing only a dry wick structure as a baseline, the baseline optical density must include the effects of the dry upper wick and the fully saturated lower wick, as well as the wall material.

Results

Initial tests were conducted to verify that the flow was occurring mainly in the upper wick (material #1) for the fully saturated case. For these tests, the upper wick (material #1) was 5-280, the lower wick (material #2) was 7-51 and both water and methanol were used as working fluids. To ensure that the wick structure was fully saturated, the head in both reservoirs was maintained at a level well above the actual level of the wick structure and gas bubbles were bled from all taps. Several determinations of the full permeability were made and all values from these tests were within 20% of the predicted value in Table 2.

Further testing of the apparatus was conducted using the same wicks and Freon-113 as the test fluid. For the earliest tests, the X-rays were taken at 15 kV. This energy level gives the best contrast in the radiographs of Freon. Exposure time was set based on the dry apparatus

such that these radiographs had nearly the highest measurable optical density (5D). However, with these exposure parameters, the working fluid blocked nearly all of the X-rays, resulting in insufficient optical intensity on the radiographs. Several different pressure distributions and resulting mass flow rates were measured nonetheless.

To allow for accurate saturation measurements, it was decided to use methanol instead of Freon. Because of the thickness of the wick, a sufficient difference in optical density was obtained using undoped methanol. Several runs were made, and it was found that the variation in saturation was not more than 10% (i.e., saturations were greater than 90%). At this point an over pressure line was installed so that air could be forced through the apparatus in a concurrent flow with the methanol. With this addition, a much larger variation in saturation was obtained. The results of the measured relative permeability are shown in Fig 34. Again, the scatter in the experimentally determined relative permeability is large. This is not unexpected given the large uncertainty in the saturation measurement for the thick wick structure. (see Appendix A) The values given in Fig 34 are compared with the results determined from the transient wicking rise tests in Fig 35. It is seen that both sets of data follow the same general trend.

Both sets of relative permeability can be described satisfactorily by using the reduced saturation raised to the second power. The commonly used relationship for granular material, obtained from extensive experimentation on packed beds of sand [30] is reduced saturation to the third power. The difference may be a result of experimental uncertainties in the present findings and/or error in the values of full permeability used to calculate the relative permeability.

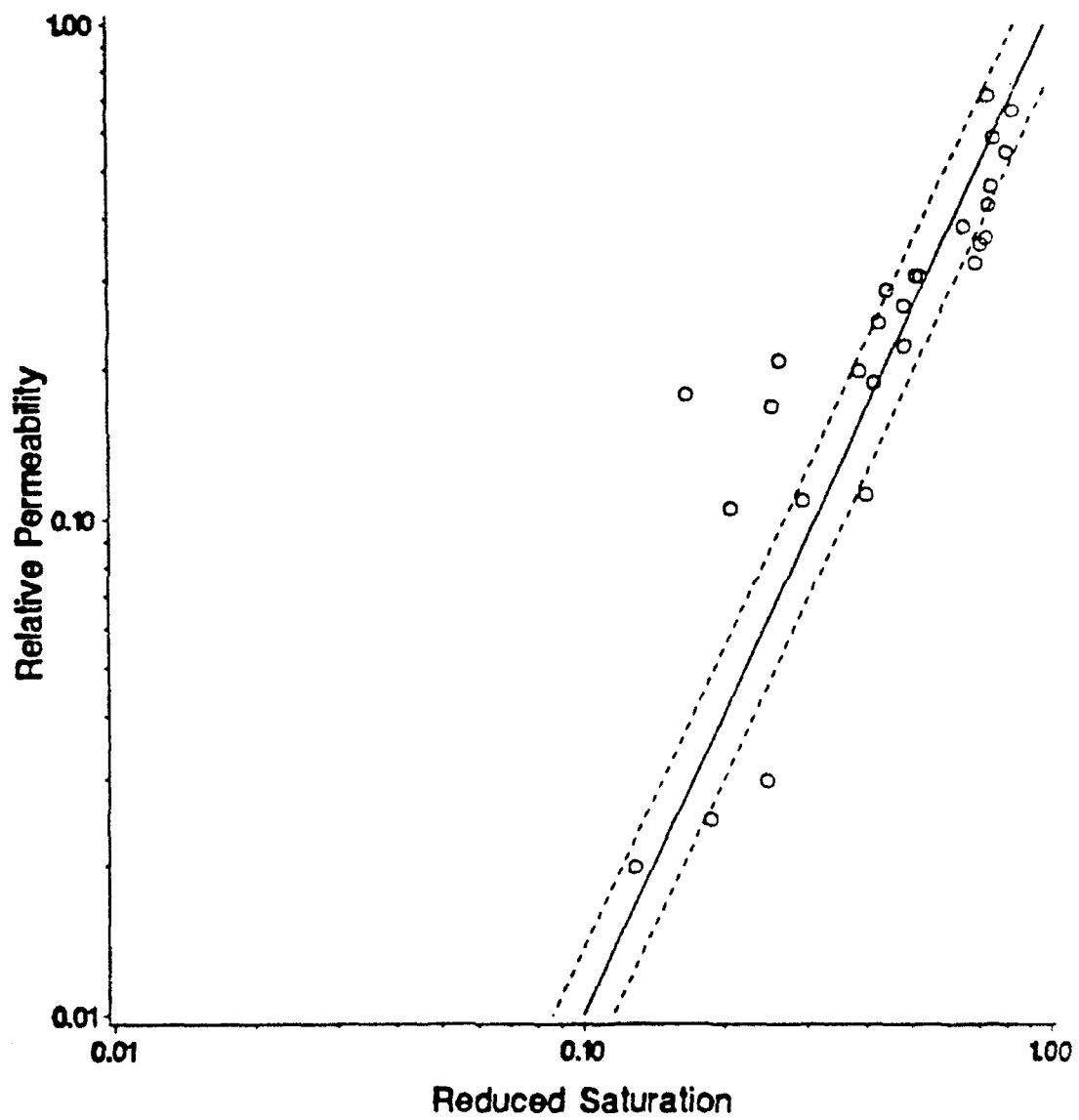


Fig 34 Relative Permeability from Steady-Flow Experiments

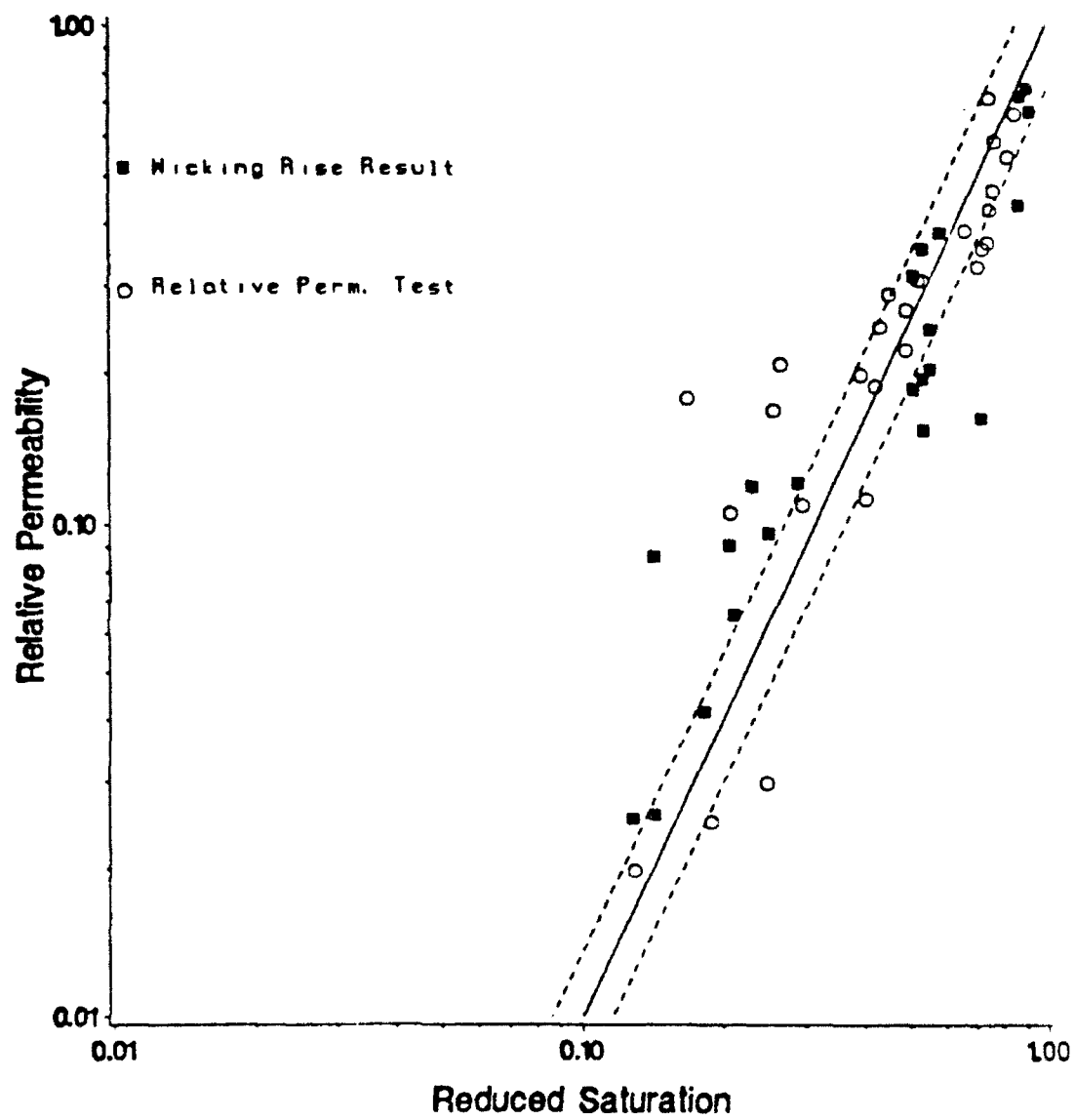


Fig 35 Comparison of Relative Permeability Data

The difference between using an exponent of two or three is not great and in any case is within the experimental uncertainty of the present measurements.

Chapter 5

DETAILED STUDY OF TRANSIENT LIQUID FLOW

This chapter describes the development and evaluation of the transient liquid flow model. A one-dimensional, transient liquid flow model is presented here. Results of experiments with a beryllium-wall heat pipe are also presented. The heat pipe allows direct measurement of the transient saturation distribution in the wick.

Although one-dimensional, the model derived here is more sophisticated than that of Chapter 2, in which saturation could only assume values of zero or 1. A continuous distribution of saturation along the length of the heat pipe will be modeled. The transient liquid flow model is based on conservation of mass and momentum. The momentum balance is introduced in the form of Darcy's Law with saturation as the dependent variable. Mass flow rates of vapor into and out of the wick are assumed known from a decoupled energy balance.

Consider the control volume shown in Fig 36, representing a small element of a wick structure. This control volume has a mass of liquid associated with it. The mass conservation equation is written for the control volume:

$$\dot{m}_{in} - \dot{m}_{out} + \dot{m}_v = \frac{\partial m}{\partial t} \quad (33)$$

where \dot{m} is liquid mass flow rate across the boundaries of the control volume, m is mass of liquid residing in the control volume and \dot{m}_v is the mass flow rate of vapor entering or exiting the control volume due to evaporation or condensation. Darcy's Law is written with saturation as

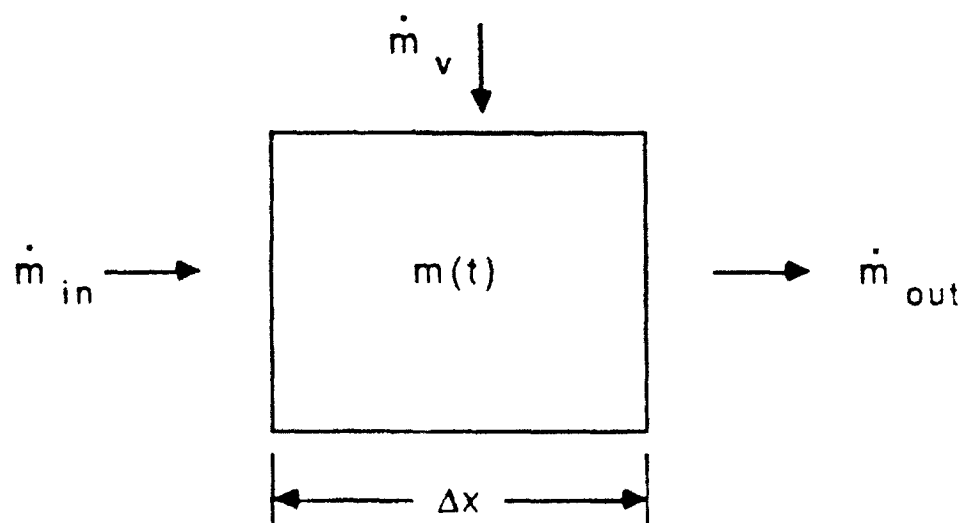


Fig 36 Wick Control Volume

the dependent variable:

$$\dot{m} = \frac{\rho A_w K K_r}{\mu} \frac{dP_c}{dS} \frac{\partial S}{\partial x} \quad (34)$$

The relationship between the mass of liquid in the control volume and the saturation is:

$$m = \rho \epsilon A_w \Delta x S, \quad (35)$$

where ϵ is the wick porosity and $A_w \Delta x$ is the volume of the control volume. When Eq(34) and Eq(35) are substituted into Eq(33) we obtain:

$$\dot{m}_v = \rho A_w \left[\epsilon \Delta x \frac{\partial S}{\partial t} + \frac{K}{\mu} \left[K_r \frac{dP_c}{dS} \frac{\partial S}{\partial x} \right]_{x+\frac{\Delta x}{2}} - K_r \frac{dP_c}{dS} \frac{\partial S}{\partial x} \right]_{x+\frac{\Delta x}{2}} \quad (36)$$

Dividing by $\rho A_w \epsilon \Delta x$ and taking the limit as Δx tends to zero, we obtain the equation for the transient saturation distribution:

$$\frac{\partial S}{\partial t} = \frac{\partial}{\partial x} \left[f \frac{\partial S}{\partial x} \right] + J \quad (37)$$

Eq(37) has the same form as the one-dimensional, nonhomogeneous heat equation. Here the moisture diffusivity is given by:

$$f(S) = - \frac{K K_r}{\mu \epsilon} \frac{dP_c}{dS} \quad (38)$$

The moisture diffusivity $f(S)$ is calculated from Eq(38) based on the

measured capillary flow properties of Chapter 4. A curve fit of the falling capillary pressure data shown in Fig 37 gives dP_c/dS . The relative permeability is estimated from Fig 35 as $K_r = \phi^2$.

It should be noted that the saturation has previously been defined as varying between zero and 1. In the present solution, saturation is allowed to take on values greater than 1 to account for mass storage in the condenser region. When a porous structure is fully saturated ($S=1$) and additional liquid is introduced to the exterior, the excess liquid cannot enter the pores. It, therefore, has no effect on the capillary flow properties of the structure. These remain at the (constant) fully-saturated values. In the present case the properties are evaluated at $S=1$ if S becomes greater than 1. Flow in the resulting puddle of liquid outside the wick is ignored.

Source Term

The source term is the mass flux of vapor normalized by the initial mass of liquid per unit area of the void space. The total mass flow rate of vapor is given by:

$$\dot{m}_{v,tot} = \frac{Q}{\lambda}, \quad (39)$$

where Q is the heat transport rate. This is equal to the heat input if there is no storage of energy. The normalized mass flux of vapor is obtained by dividing the total amount by a length. For the evaporator region, the $\dot{m}_{v,tot}$ is divided by the evaporator length. The source term in the evaporator region J_e is given by:

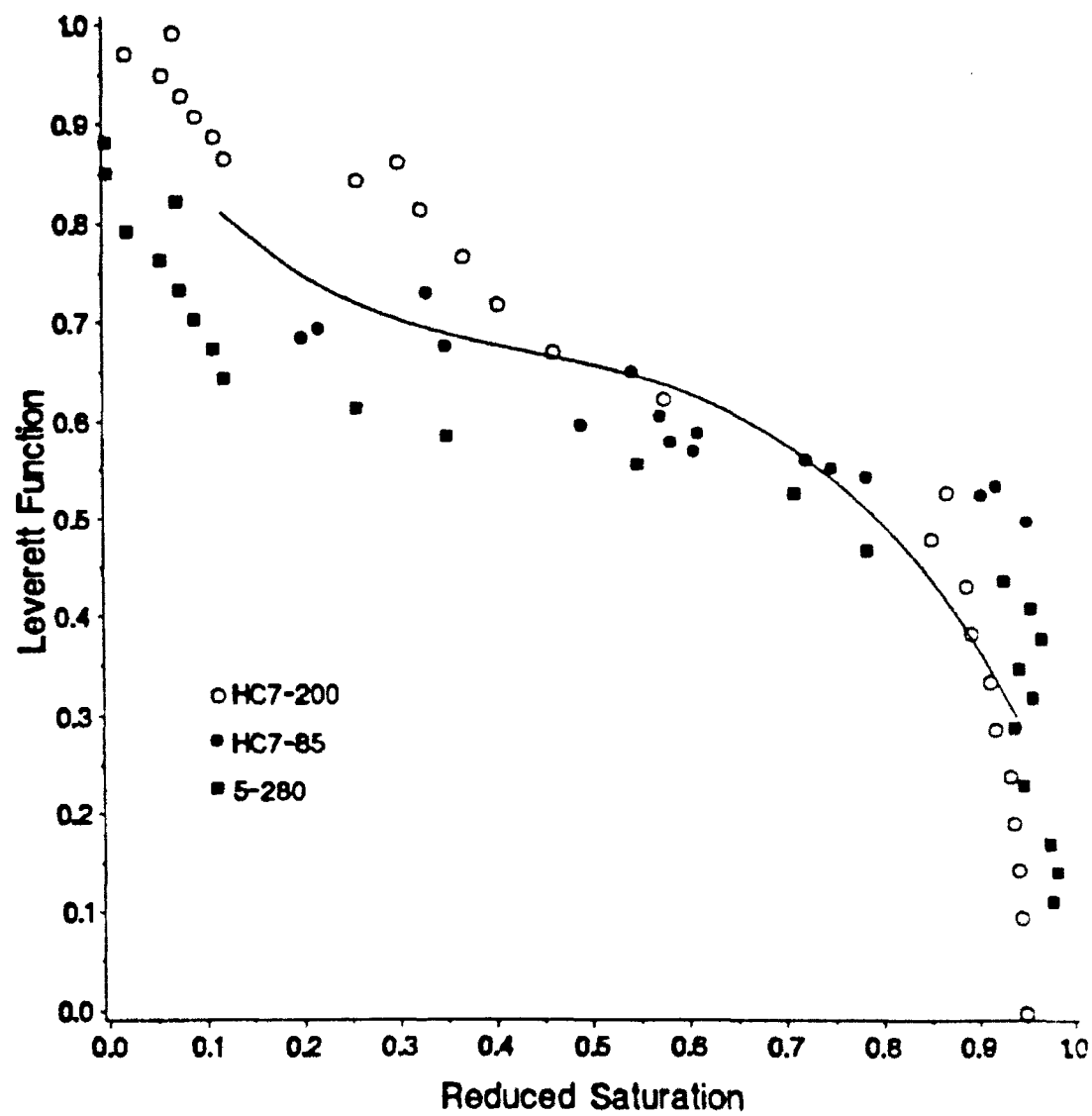


Fig 37 Falling Capillary Pressure Data

$$J_e = - \frac{Q}{\rho \epsilon \lambda_w \lambda L_e} . \quad (40)$$

Similarly for the condenser region:

$$J_c = \frac{Q}{\rho \epsilon \lambda_w \lambda L_c} . \quad (41)$$

Implicit in Eqs(40,41) is the assumption that the vaporization and condensation are uniform over the evaporator and condenser, respectively.

Boundary and Initial Conditions

The boundary conditions state that no mass flow occurs through the two ends of the wick structure. This is the case in the actual heat pipe where the ends are sealed and recirculation of fluid occurs due to evaporation and condensation. From Eq(35) this requires that $\partial S / \partial x = 0$ at $x=0$ and $x=L_T$.

The initial condition for this problem is a uniform saturation equal to unity. This is the case in an actual, fully-charged heat pipe assuming that the pipe has had sufficient time without heat loading and that the liquid wets the wick uniformly.

Numerical Solution

The complete problem specification is given as:

$$\begin{aligned}\frac{\partial S}{\partial t} &= \frac{\partial}{\partial x} \left[f \frac{\partial S}{\partial x} \right] + J, \quad 0 \leq x \leq L_T \\ S(x, 0) &= 1 \\ \frac{\partial S}{\partial x}(0, t) &= 0, \quad \frac{\partial S}{\partial x}(L_T, t) = 0 \\ J &= J_e; \quad 0 \leq x < L_e, \quad t \geq 0 \\ J &= J_c; \quad L_e < x \leq L_T, \quad t \geq 0 \\ J &= 0; \quad x = L_e, \quad t \geq 0\end{aligned}\tag{42}$$

The parabolic initial-boundary value problem Eq(42) was solved numerically using the SPRINT package [31,32], which is a general-purpose computer program for the numerical solution of mathematical models which involve mixed systems of time-dependent algebraic, ordinary and partial differential equations. This package contains two spatial discretization options and four routines for performing the time integration. In the present work, the finite difference module SPDIF was chosen for the spatial discretization and the time-stepping was performed using the SPGEAR module, which contains both the the family of Adams methods up to order 12 and the family of Gear/backward difference formula (BDF) methods up to order 5. Details of these modules are given in [31]. With these choices, SPRINT was run with various subdivisions of the spatial interval and various tolerances on the time integration. Results are given in tabular form in Appendix B. These results show that the solution is relatively insensitive to the tolerance placed on the time integration. Based on the results, a time step of 1 second and 120 spatial intervals were deemed sufficient for the present problem.

Numerical Results

Results were obtained with values of the source term corresponding to heat inputs from 15 to 35 watts. The input parameters used in the model are summarized in Table 3. The fluid properties were evaluated at a temperature of 40 °C for all results. Transient saturation distributions are shown in Figs 38-42.

The results from the numerical solution show a decreasing saturation in the evaporator region starting from $t=0$. At power inputs of 30 W or greater, the saturation drops below the irreducible saturation of 15%. This corresponds to dryout of the wick in an actual heat pipe.

Table 3. Input Parameters for Detailed Liquid Flow Model

Constants	Dimensions	Fluid Properties
$K - 7.88 \times 10^{-10} \text{ m}^2$	$A_w - 2.85 \times 10^{-5} \text{ m}^2$	$\mu - 5.5 \times 10^{-4} \text{ Ns/m}$
$\epsilon - 0.7$	$L_t - 30 \text{ cm}$	$\rho - 1530 \text{ kg/m}^3$
	$L_e - 13 \text{ cm}$	$\lambda - 1.5 \times 10^5 \text{ J/kg}$
	$\Delta x - 0.0025 \text{ m}$	$\sigma - 1.7 \times 10^{-2} \text{ N/m}$
	$\Delta t - 1 \text{ s}$	

Beryllium Heat Pipe Tests

The purpose of this research was to provide a detailed model for predicting transient liquid flow in heat pipes. To verify this model, direct measurements were obtained of the transient saturation

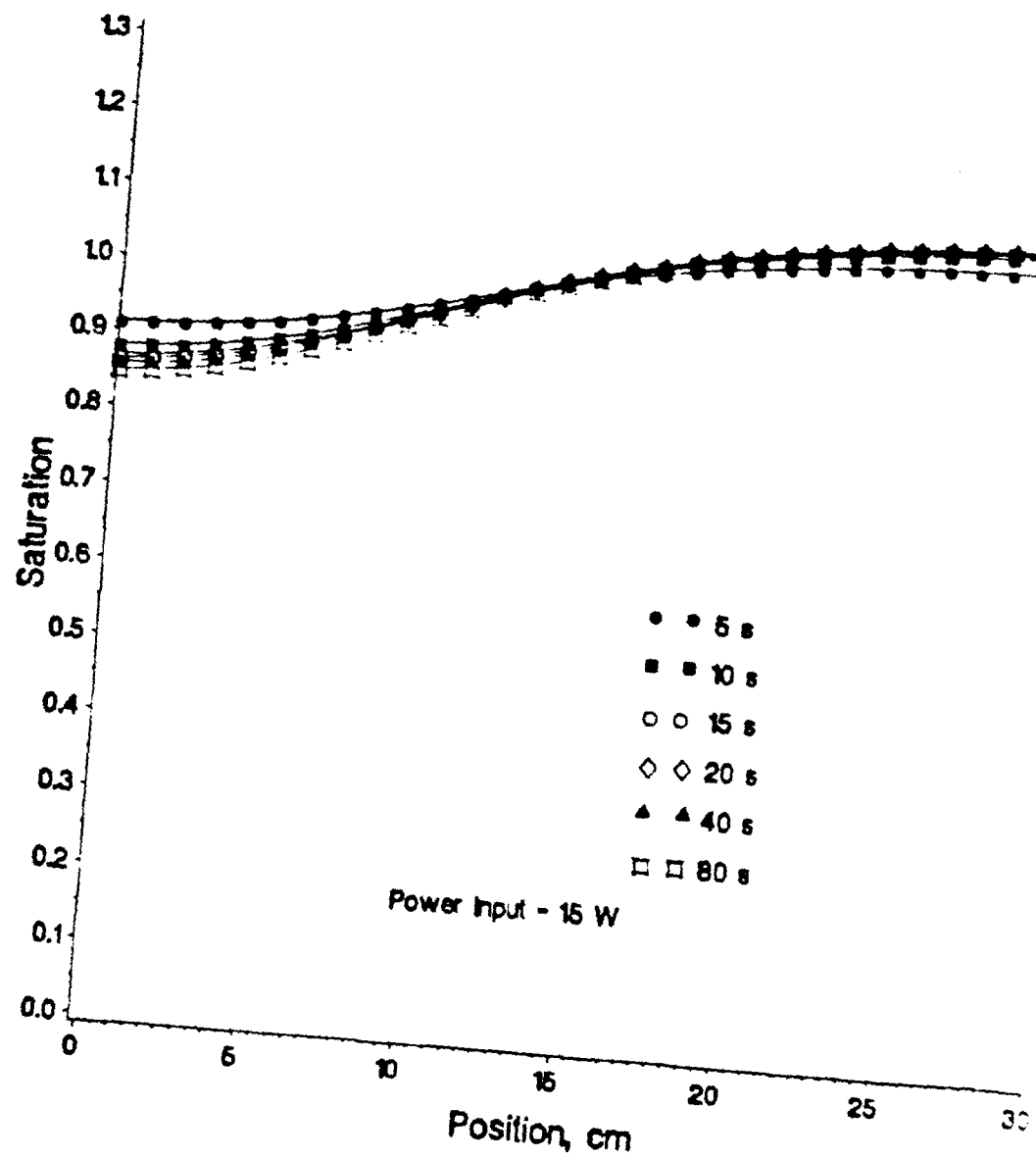


Fig 38 Transient Saturation Profile, 15 W

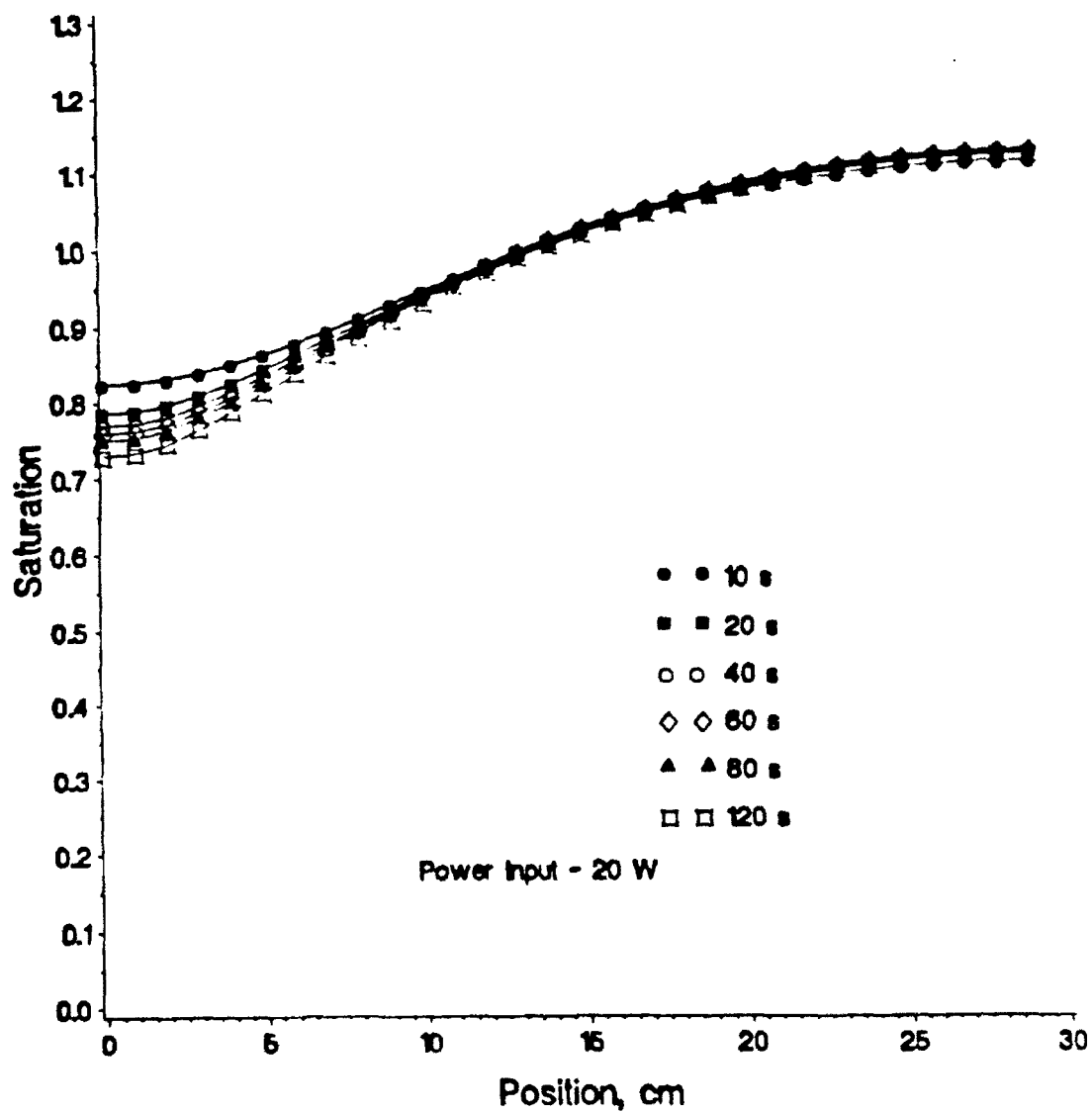


Fig 39 Transient Saturation Profile, 20 W

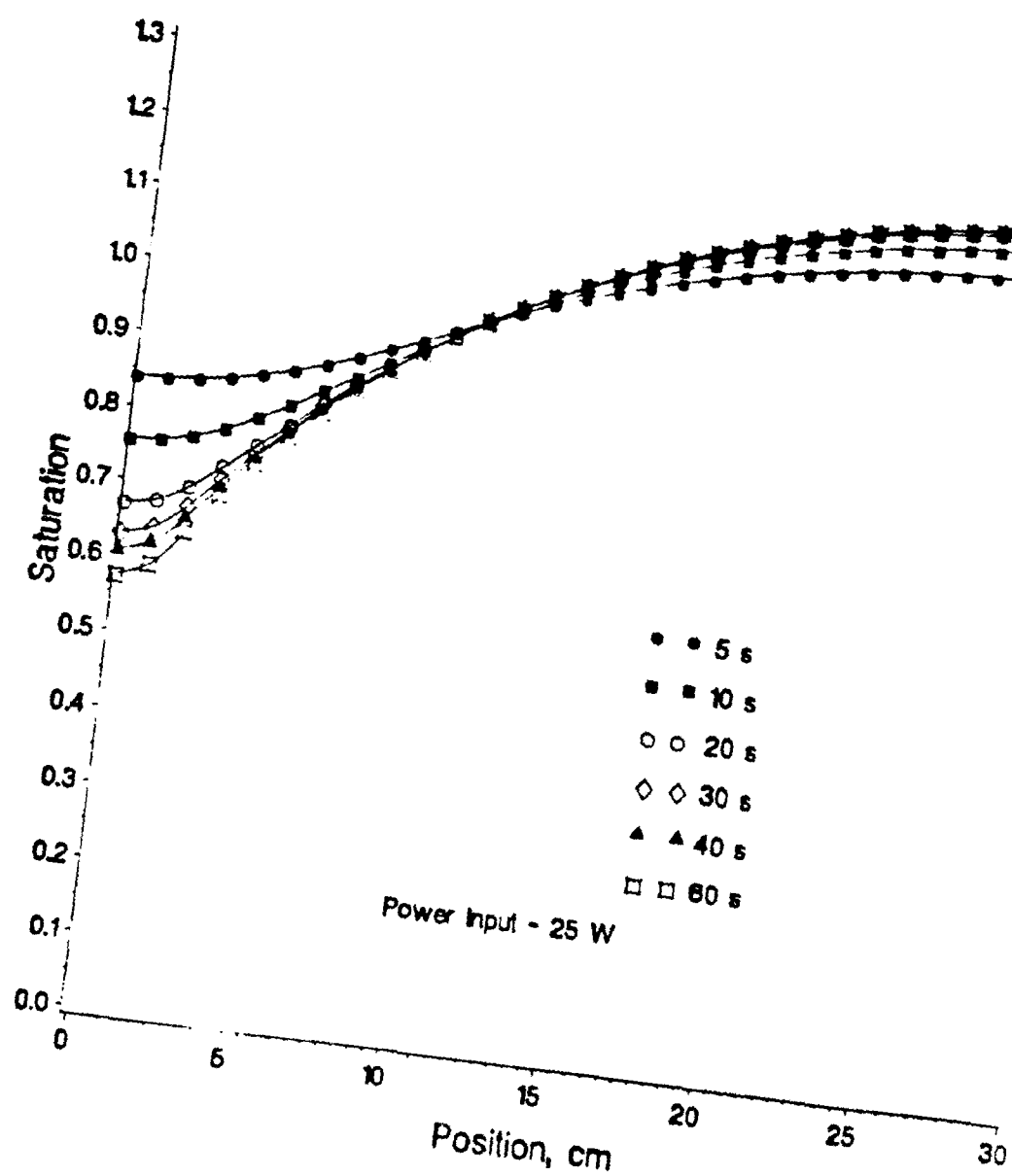


Fig 40 Transient Saturation Profile, 25 W

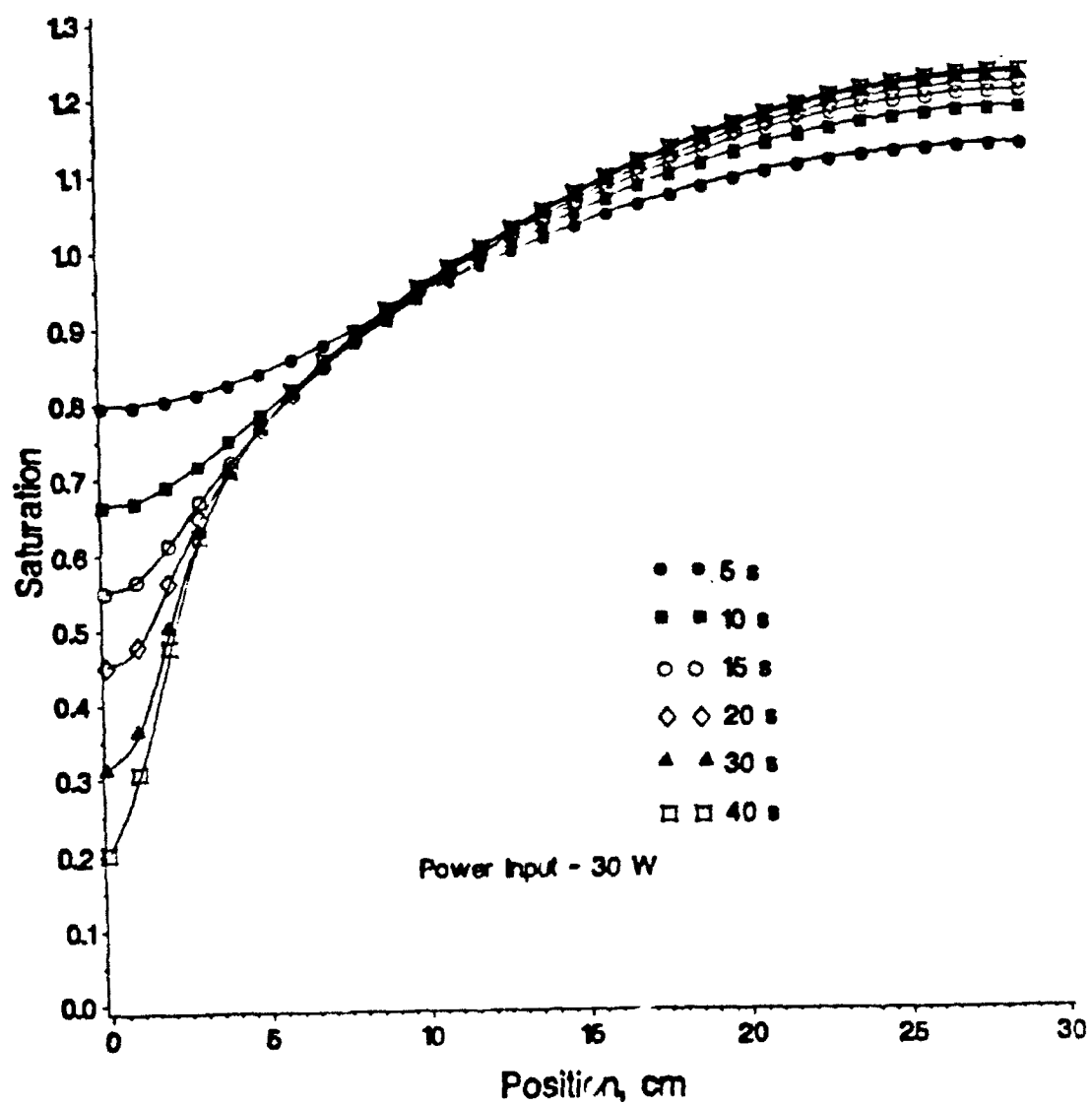


Fig 41 Transient Saturation Profile, 30 W

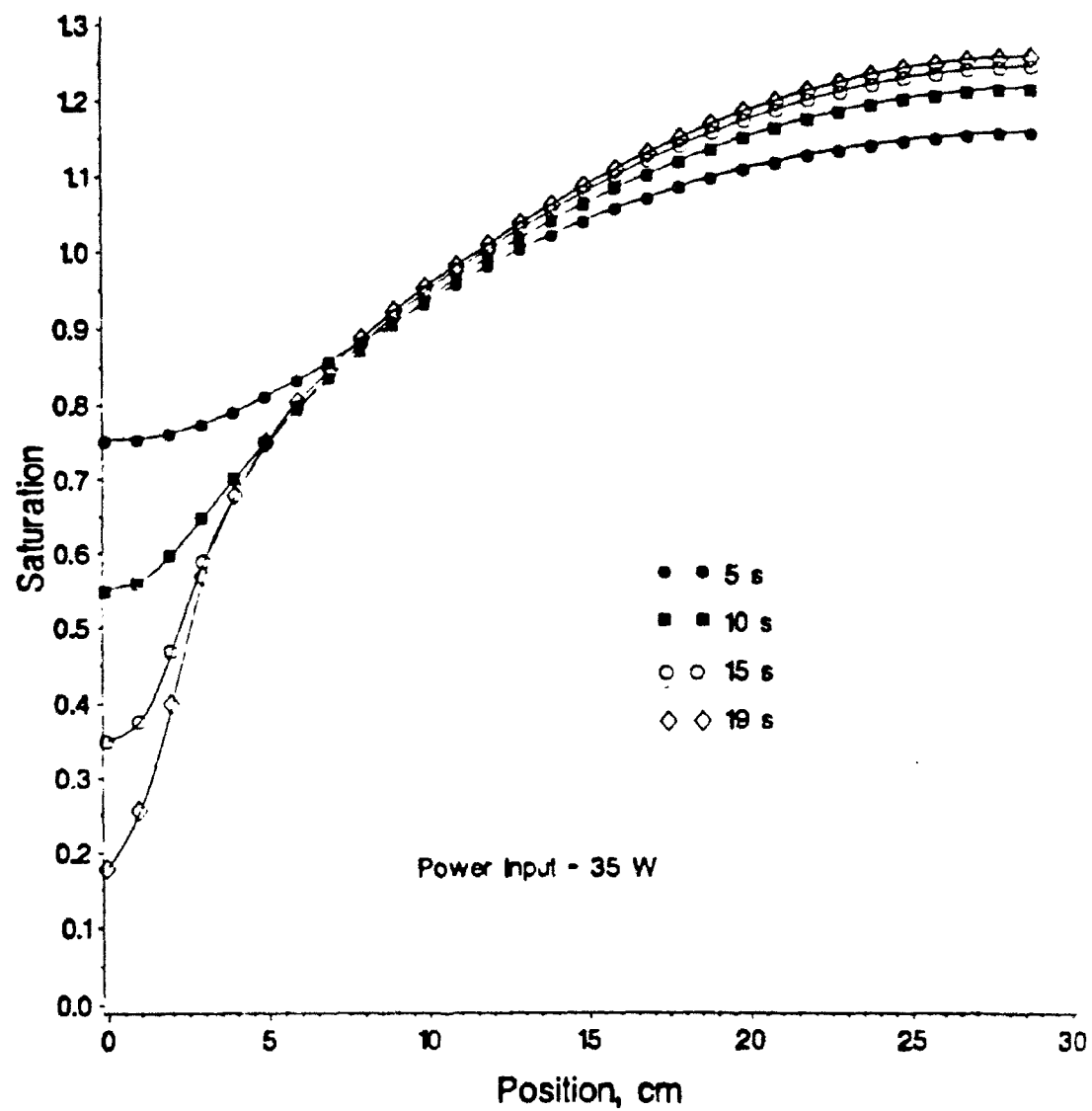


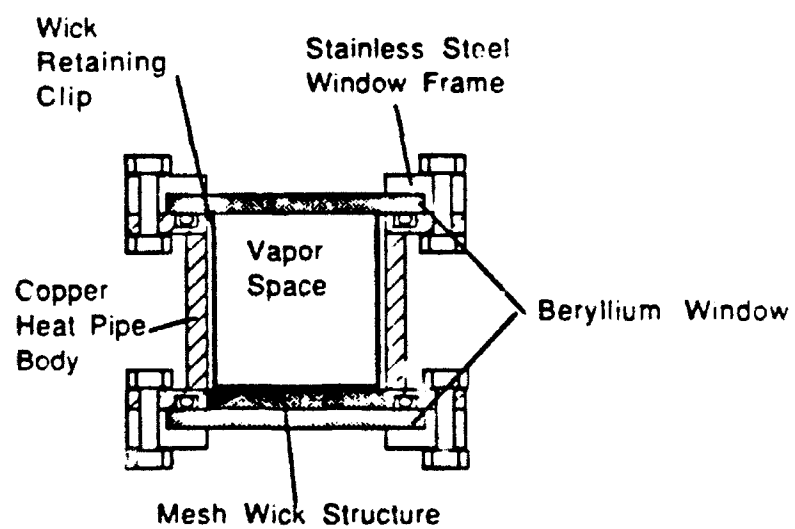
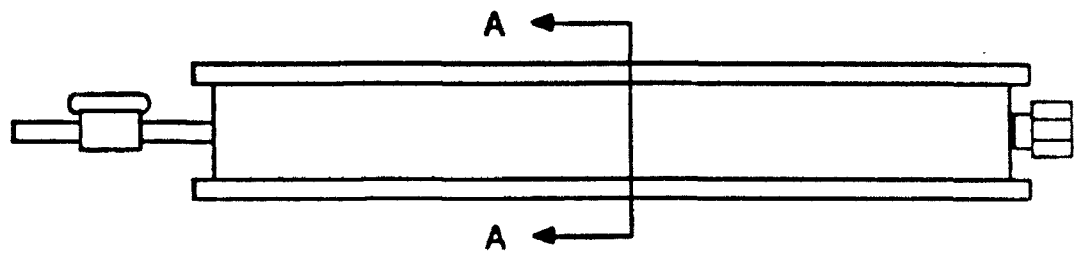
Fig 42 Transient Saturation Profile, 35 W

distributions in an operating heat pipe. A beryllium wall heat pipe was designed and fabricated for this purpose. The heat pipe is shown in Fig 43.

The heat pipe is constructed of copper, with two opposing beryllium walls through which the beam of X-rays may pass. The beryllium plates are sealed to the copper body with O-rings and held in place with top plates made of stainless steel. A copper tube is welded to one end of the body and attached to a valve used for evacuation and filling. At the other end is a brass feedthrough for the thermocouples used to measure interior temperatures during operation.

The wick material consists of five layers of the 5-280 mesh material, cut so as to fit snugly in the cavity of the pipe against the bottom wall. The layers of mesh material were sewn together at numerous locations, in the pattern shown in Fig 44, using polyester threads approximately 40 μm in diameter. In addition, it was necessary to use a wire mesh to provide uniform clamping pressure on the material so that it would remain planar and not develop excess space between layers. The wick is held tightly against the wall by a coarse stainless steel mesh (8 wires per inch). This in turn is held down with special springs. The springs, made of copper-plated steel, are designed to minimize intrusion into the X-ray imaging area of the heat pipe.

A special heater was designed for this heat pipe and is constructed of carbon. The heater, shown in Fig 45, is a thin slab of graphite with copper contacts inserted through holes in the ends. A direct current is passed through the carbon, which is insulated from the beryllium wall by an extremely thin sheet of mica. The thin carbon heater allows imaging of the working fluid in the evaporator region of



Cross Section A-A

Fig 43: Beryllium Heat Pipe Schematic

• Stitch Location



x Wall/Wick Thermocouple x Vapor Thermocouple

Fig 44 Diagram of Wick Structure



Top View



Electrical Contacts

Side View

Fig 45 Graphite Heater

the heat pipe.

Internal temperature measurements are obtained from fine (0.003inch diameter) copper/constantan thermocouples located inside the heat pipe. The wires have a fine coating of Isonel shellac insulation. There are 12 thermocouples, 10 located between the wall and the wick and 2 in the vapor space. The arrangement of the thermocouples is shown in Fig 44. The thermocouples are passed into the heat pipe through a 1/8inch copper tube and ferrule fitting. Epoxy was used to seal the thermocouple wires into the tube. This arrangement had been devised as the most feasible method of providing a leak-proof seal with such fine gauge thermocouple wires.

Heat Pipe Preparation

Prior to filling, the heat pipe was cleaned thoroughly in soapy water, followed by rinsing in methanol and then in Freon. It was closed, given a final rinsing with Freon, and then attached to the fill station. A glass heat pipe fill station was designed and fabricated specifically for this project. This fill station is shown in Fig 46. It includes a liquid nitrogen cold trap to facilitate flushing of the heat pipe. The heat pipe is evacuated to a pressure of approximately 100 microns of mercury and then filled with working fluid. The working fluid is then flushed into the evacuated liquid-nitrogen cold trap. The evacuation and fill procedure are then repeated. In this way, the level of noncondensable gases in the heat pipe is reduced to a negligible level.

The charge (amount of working fluid) is calculated based a fully saturated wick structure. If V is the total volume of the wick based on

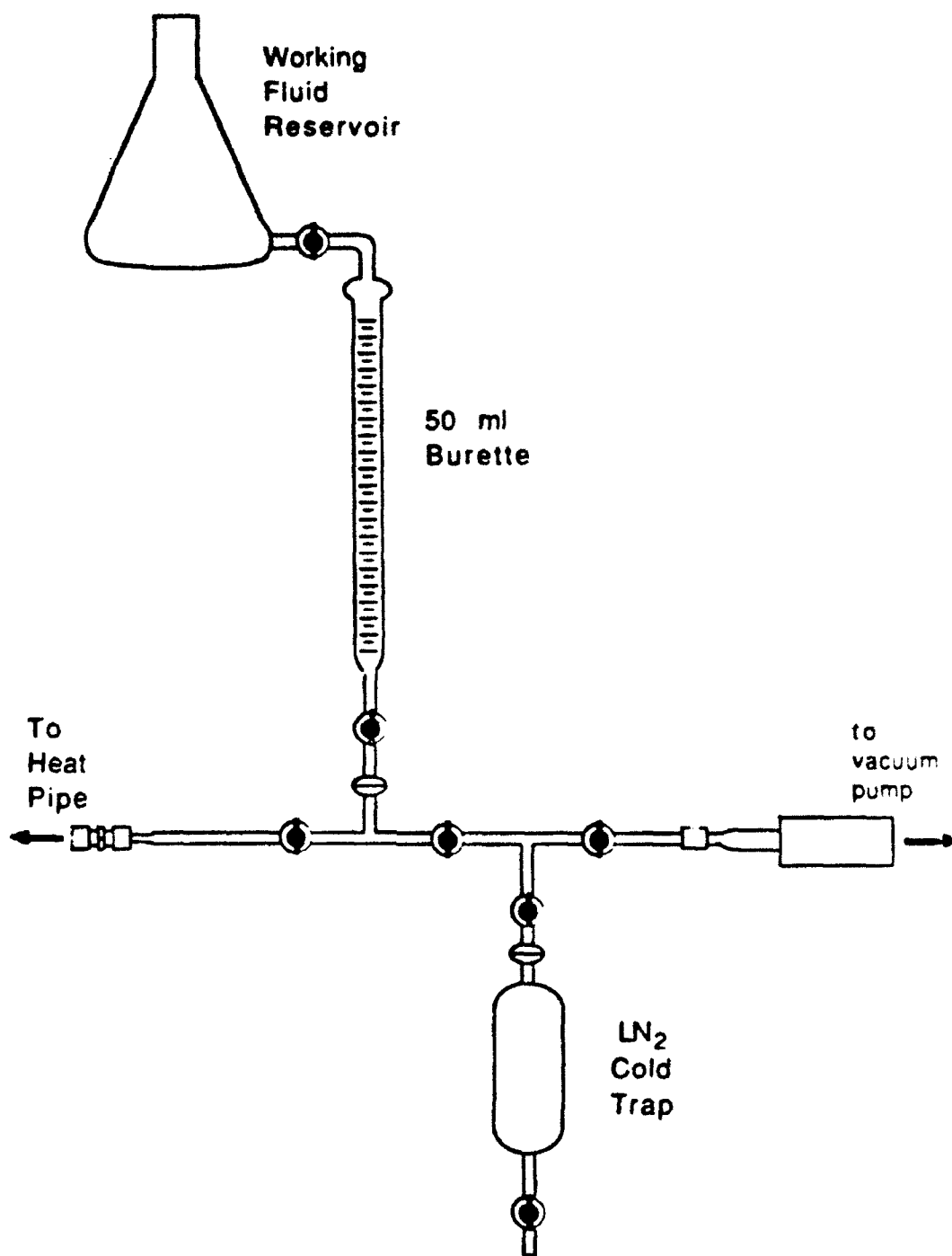


Fig 46 Heat Pipe Fill Station

its exterior dimensions and ϵ is the porosity, then the volume of liquid is ϵV . The charge for the mesh wick of dimensions 29.2 cm x 1.9 cm x 1.5 mm and porosity of 69.9% is 6.15 ml of Freon-113. On final filling, this amount of fluid is added to the heat pipe by noting the drop in liquid level in the fill burette (Fig 46) which is calibrated in 0.1-ml increments. Once the heat pipe is filled, the fill valve on the heat pipe is closed and the heat pipe is removed from the fill station.

The heat pipe was insulated with ceramic fiber insulation. Approximately 1/2 inch of the material covered all surfaces except the exposed beryllium windows. A thin layer ($\sim 1/8$ inch) of insulation was placed over the heater. This insulation was kept thin to reduce attenuation of X-rays, already at its greatest in the heater region.

Power input to the heat pipe was calculated from voltage and current measurements. The voltage drop across the heater was measured directly, and a calibrated, 4.6 m Ω shunt resistor was used to measure the current flow. Because the only available power supply was unregulated, the heat input to the heater fluctuated by up to 5 W. This problem was not considered to be critical, because, as will be discussed further, the heat-transport rate could only be estimated.

Heat Pipe Tests

The test setup consists of the heat pipe, the X-ray system, power supply, air flow system and data logger. A schematic of the setup is shown in Fig 47. The heat pipe is located in the X-ray chamber, with wires passed outside for the thermocouples and the heater. Two air lines are passed into the chamber, one hot and one room temperature. The hot air flows onto the upper surface of the heat pipe so that this

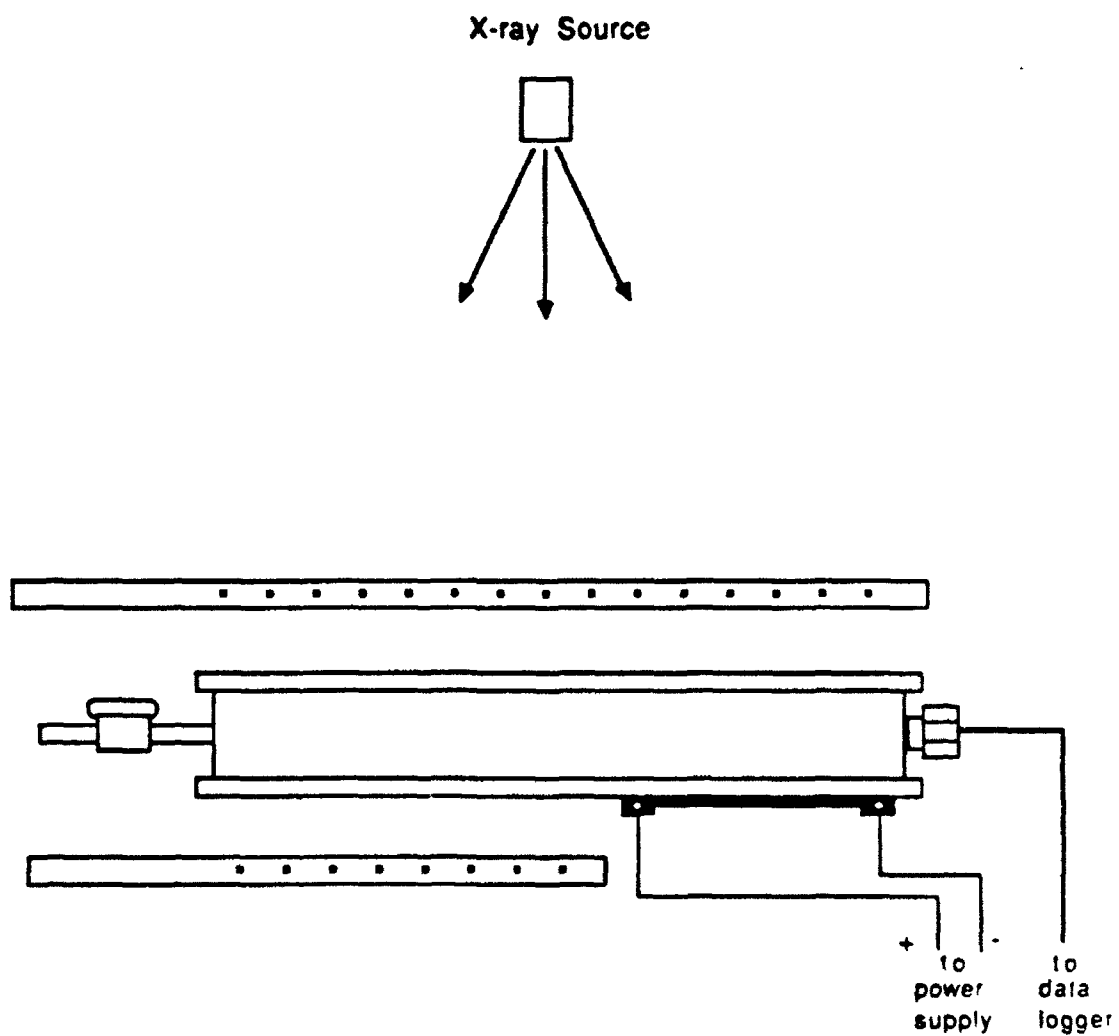


Fig 47 Heat Pipe Experiment Schematic

surface will remain at a higher temperature than the Freon vapor. This reduces the condensation on the upper surface which would decrease accuracy of the saturation measurement. The room temperature air is directed onto the lower surface at the condenser region. Because the heat pipe can transport only of the order of 10 W, natural convection or low flow rate forced air is sufficient to remove the heat.

Tests were conducted by first raising the temperature of the heat pipe using only the hot air. The objective was to minimize thermal energy storage during the test without affecting the initial saturation distribution. The heat transfer to the pipe is mainly by conduction through the wall with some heat being transferred directly to the vapor. Initial saturation distributions were checked to ensure that the procedure did not affect the saturation distribution. As discussed in Chapter 2, a pulse of heat applied to a heat pipe will result in significant thermal storage unless the cooling conditions can accommodate the load without increasing the rejection temperature. In the present case an attempt was made to minimize thermal storage by starting with the pipe at an elevated temperature. This procedure was supplemented by providing the cooling air on the bottom face starting at the same instant as the heat pulse.

Both steady-state and transient experiments were performed using the beryllium heat pipe. Experiments consisted of applying a fixed heat load to the evaporator of the pipe. At the same time, the power input and all temperatures were monitored using the data logger and X-rays were taken at discrete time intervals to determine the saturation.

Transient Tests

Prior to each transient test, the heat pipe was heated to an initial temperature of 35-50 °C using the hot air directed on the top surface. An initial radiograph was taken to verify a uniform saturation distribution prior to application of the heat load. The heat load was applied in one pulse. Radiographs were taken at intervals of roughly 15 seconds for the test duration, usually about 5 minutes. The exposure time in the tests was 2 seconds. For some tests, further radiographs were taken after heat input was removed to measure the increasing saturation in the evaporator zone. The results for the transient saturation distributions are shown in Figs 48-54.

It was found that thermal energy storage could not be negated even though the pipe was initially hot. The pipe temperature was seen to increase moderately after the pulse of heat was applied. This rise in temperature was not uniform along the heat pipe. The estimated heat capacity of the heat pipe is about 425 J/°C. Therefore, even a small rise in temperature can account for a substantial fraction of the heat input. Representative results for the heat storage are shown in Fig 55. The temperature of the vapor core, which is approximately equal to the average heat pipe temperature, is plotted versus time for two tests. From this graph, the heat storage was estimated for each test and subtracted from the measured heat input. The estimated heat storage for the tests was about 20-25 W. This correction provides a more accurate estimate of the heat-transport rate, but does not account for heat input from the hot air or heat losses from the pipe. The magnitudes of these are estimated to be lower than the thermal storage and the heat transport. The estimated heat-transport rate including the

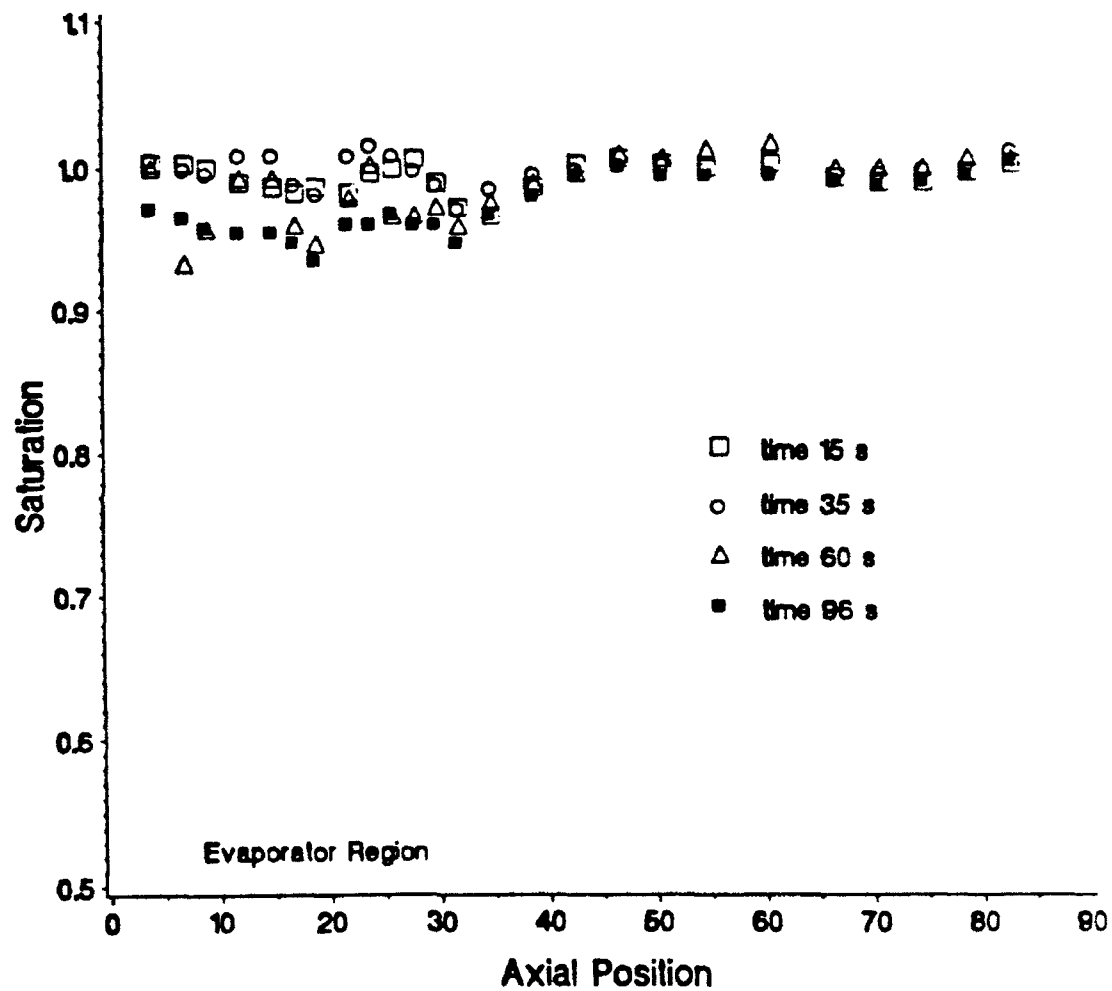


Fig 48 Transient Saturation Profile, Test 1141

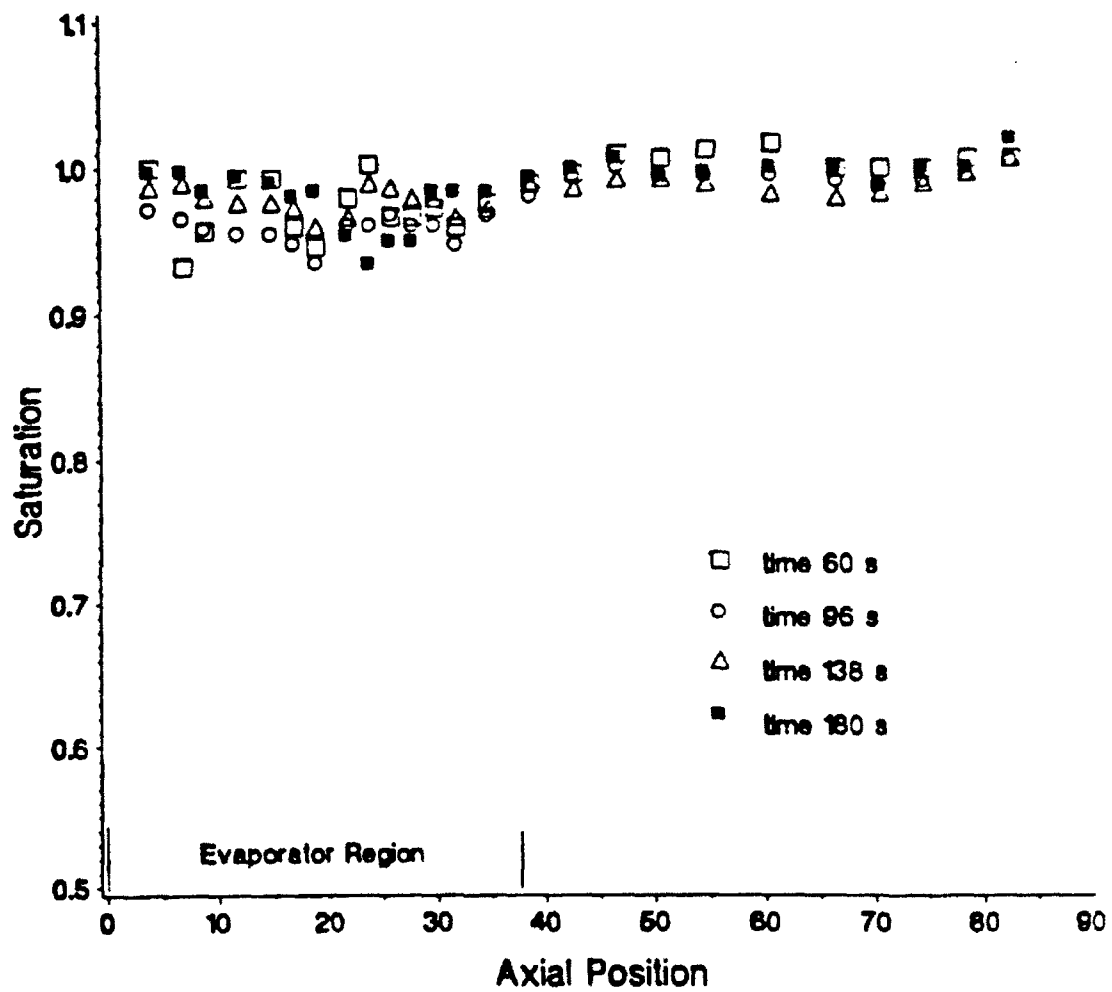


Fig 49 Transient Saturation Profile, Test 1141

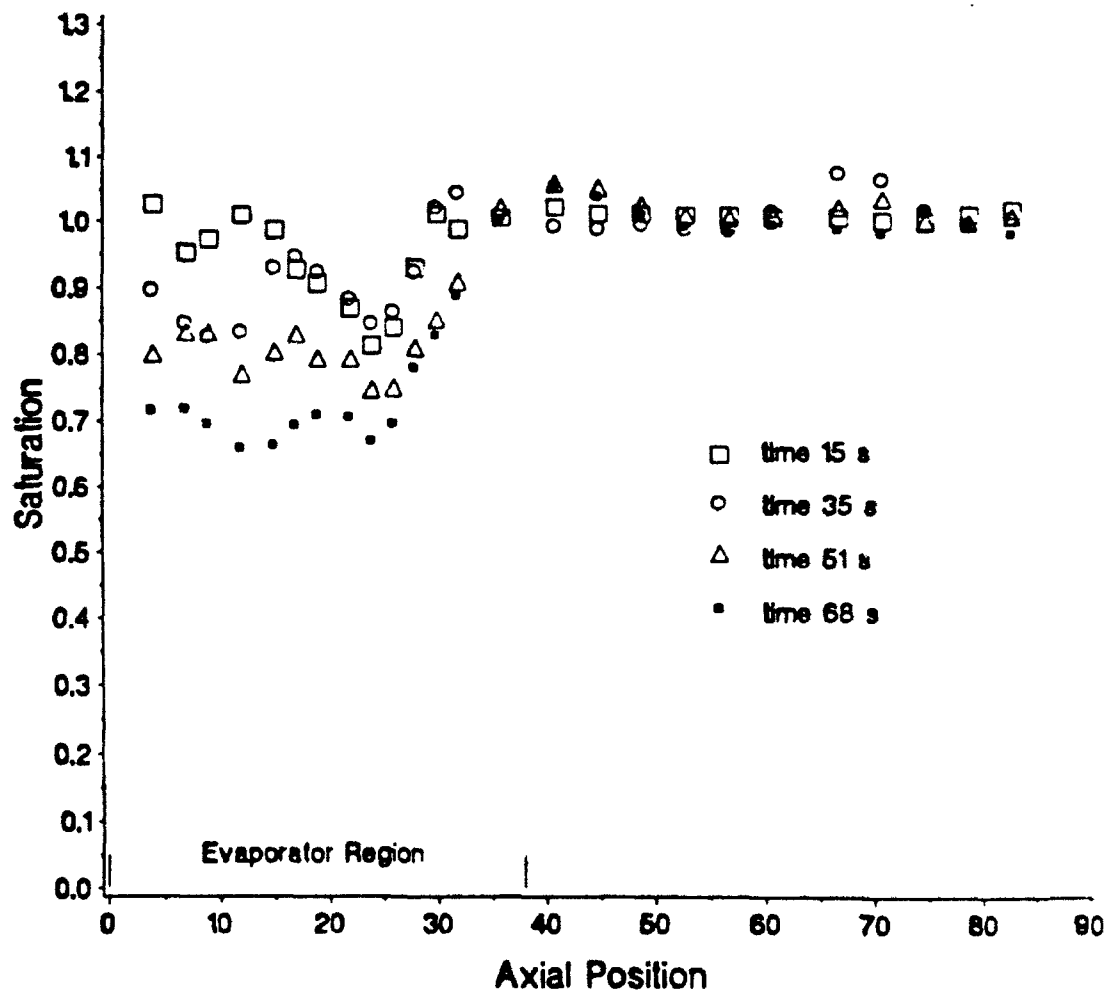


Fig 50 Transient Saturation Profile, Test 1142

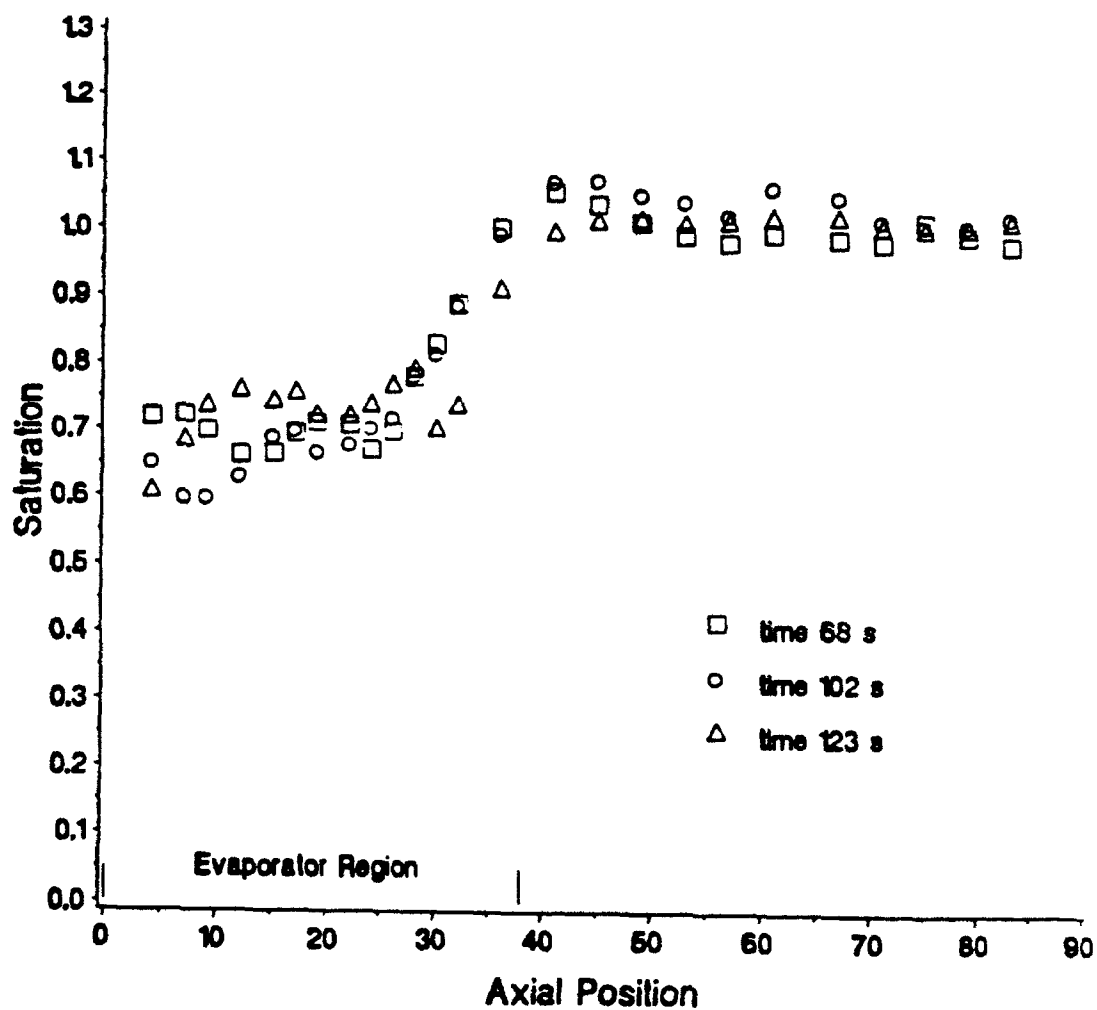


Fig 51 Transient Saturation Profile, Test 1142

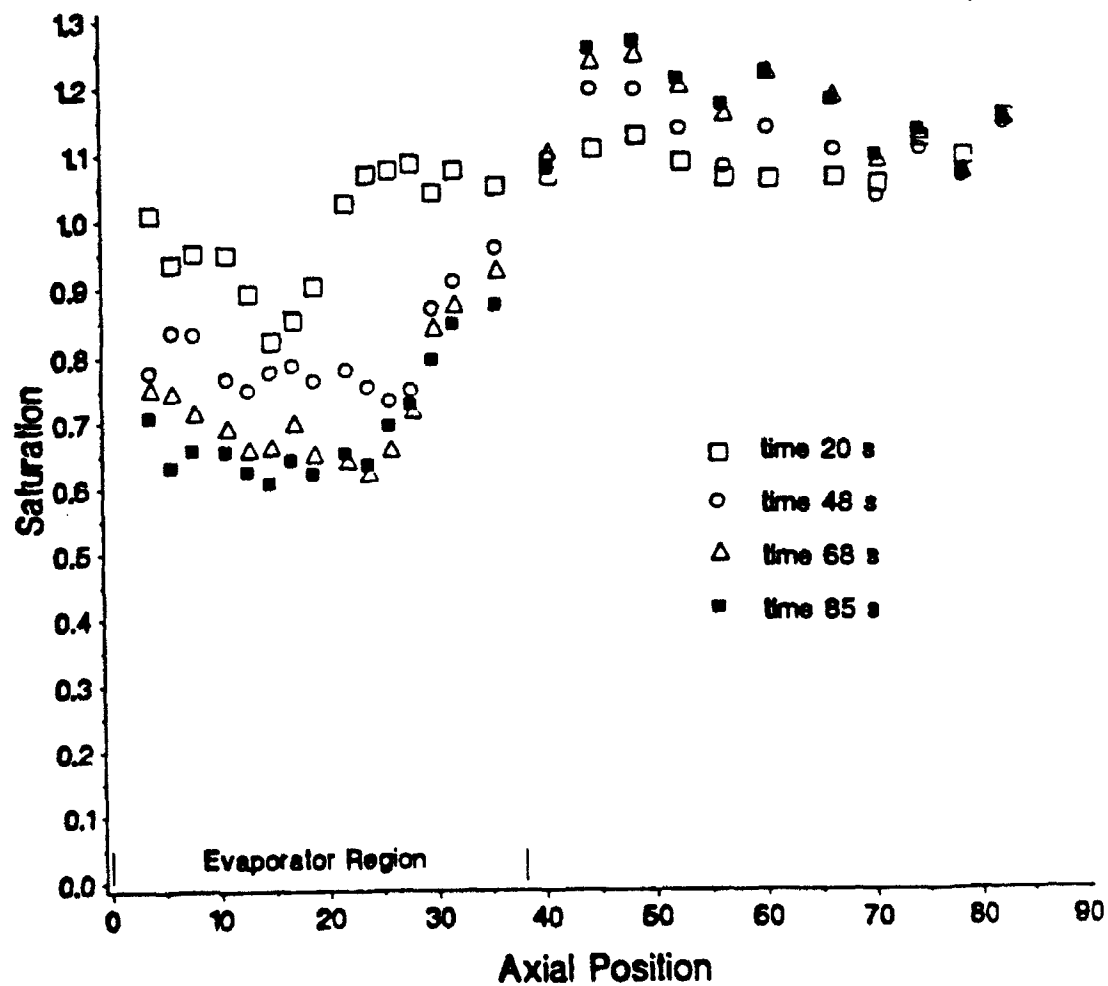


Fig 52 Transient Saturation Profile, Test 1171

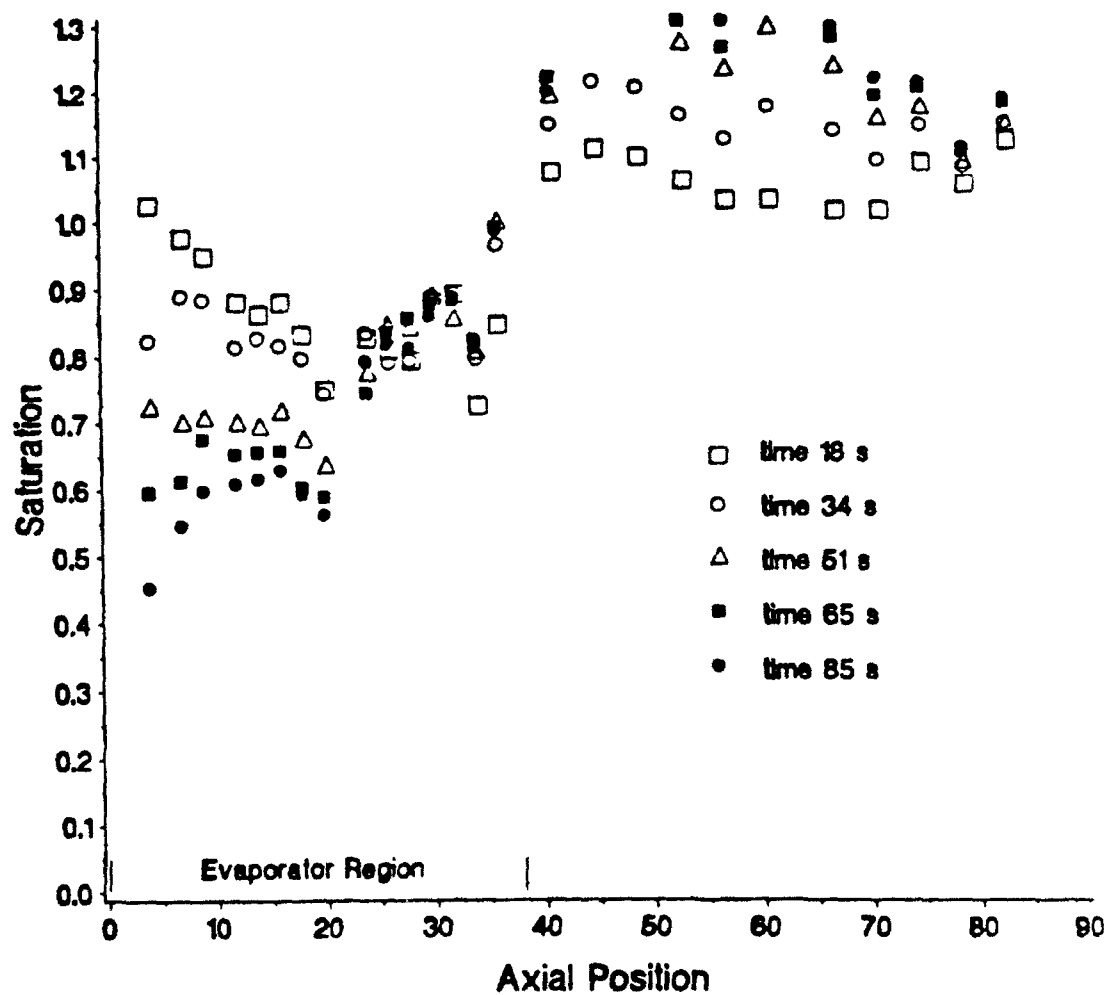


Fig 53 Transient Saturation Profile, Test 1172

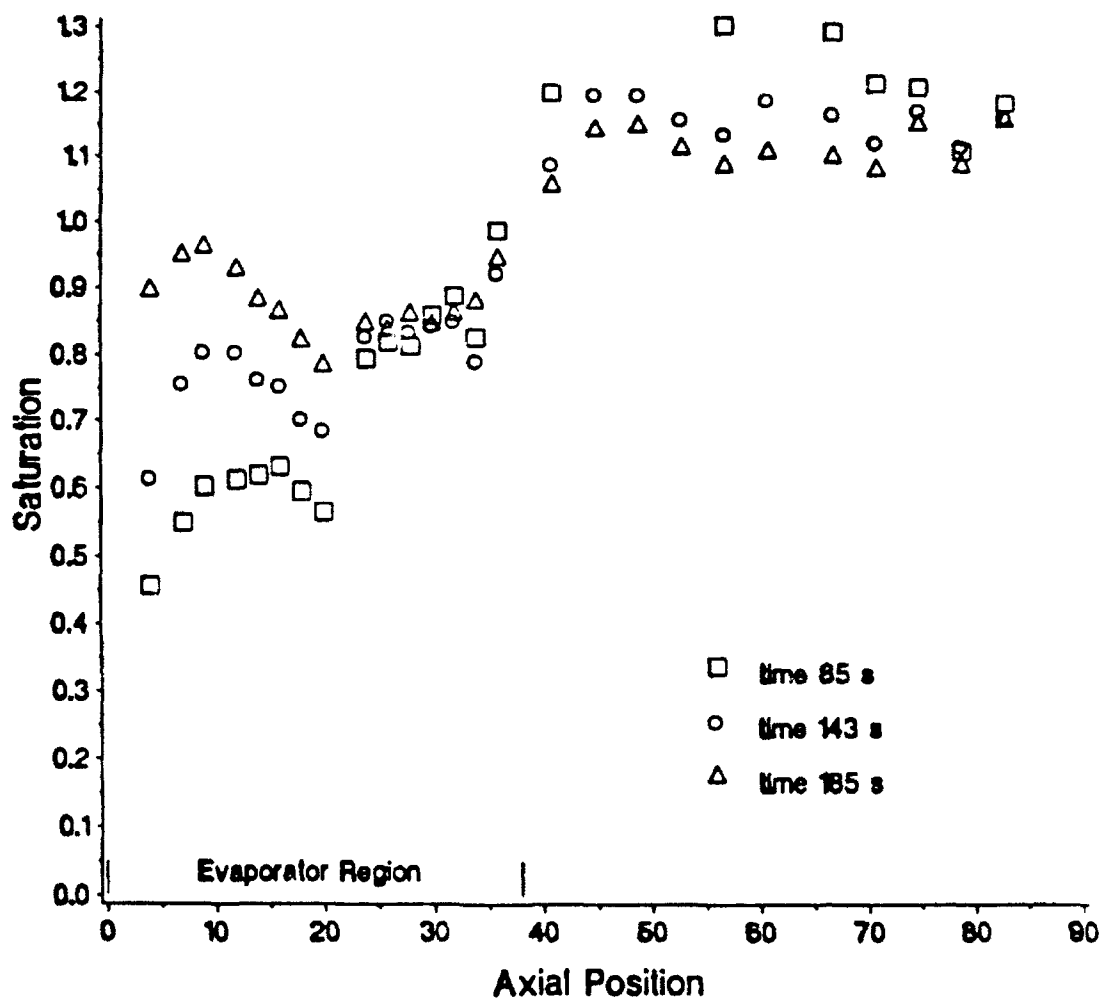


Fig 54 Transient Saturation Profile, Test 1172

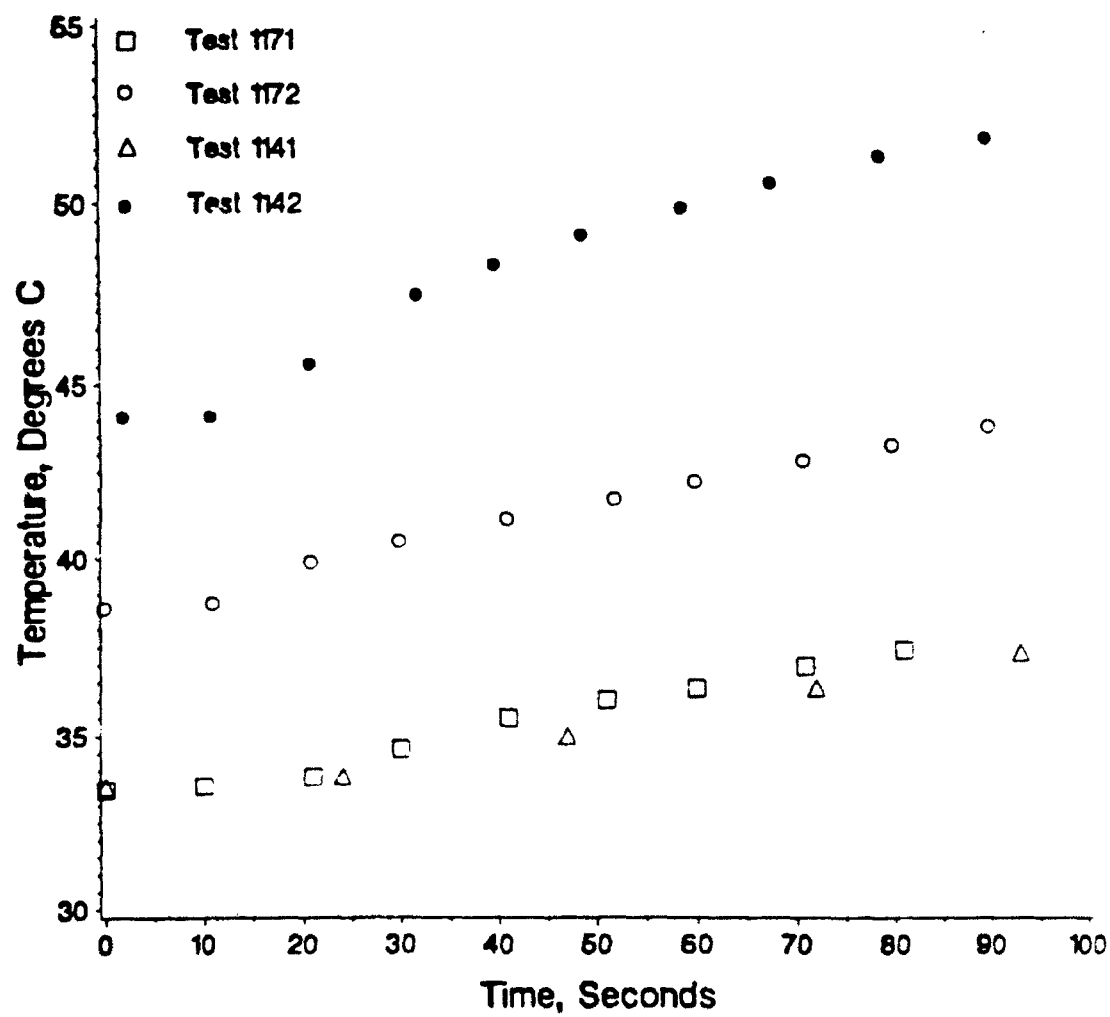


Fig 55 Transient Vapor Temperatures, All Tests

effect of storage is 20,25,30 and 35 W for tests 1141,1171,1172 and 1142, respectively.

The transient temperature profiles for the four tests are given in Figs 56-59. Both internal and external temperatures are indicated on the graphs. Temperature difference ΔT_e between the evaporator wall/wick and the vapor is a measure of the actual heat transport by the heat pipe. The values for ΔT_e agree well with values predicted using a correlation of boiling heat transfer [33], except for test 1172. It is obvious that drying of the wick was occurring during this test from the steady increase in ΔT_e . From the transient saturation profiles for this test (Figs 53,54), it is seen that the largest reduction in saturation occurred for this test. The measured reduction in saturation is not as great as predicted by the model for a power input of 30 W. However, considering the larger uncertainty of the saturation measurement for smaller values of the saturation, the measured reduction is (within experimental uncertainty) close to the dryout condition ($S=0.15$).

Steady-State Test

The steady-state test was an extension of a transient test. The heat input was continued for a period of about 30 minutes, or until no steady change in temperature was observed. A radiograph of the heat pipe was then taken to obtain a steady-state saturation distribution. The steady-state saturation distribution is shown in Fig 60. The estimated heat input for this test was about 30 W. After the test 114S it was found that about a third of the insulation on the heater had fallen off. This indicates that the heat losses were significantly larger for this test and transient tests 1141 and 1142. The forced air

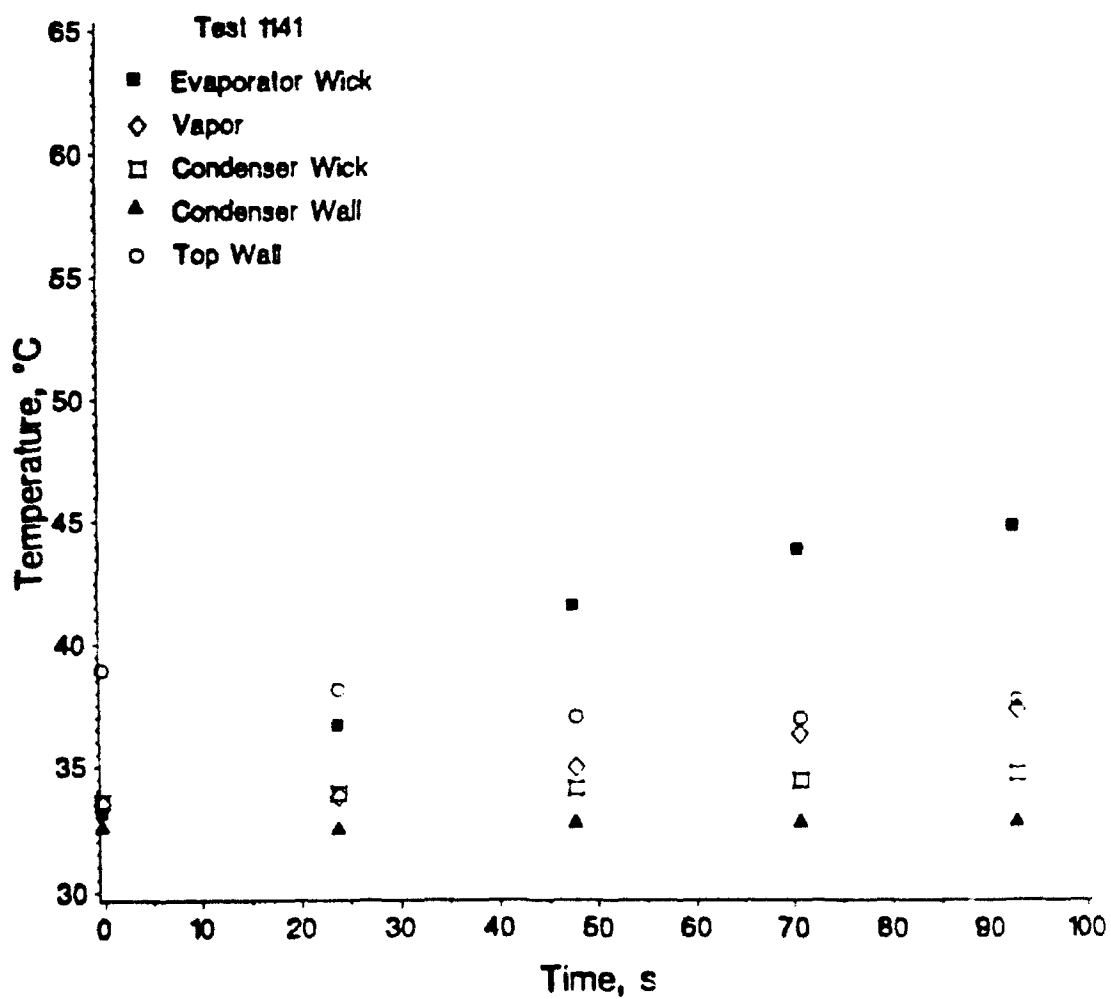


Fig 56 Transient Temperatures, Test 1141

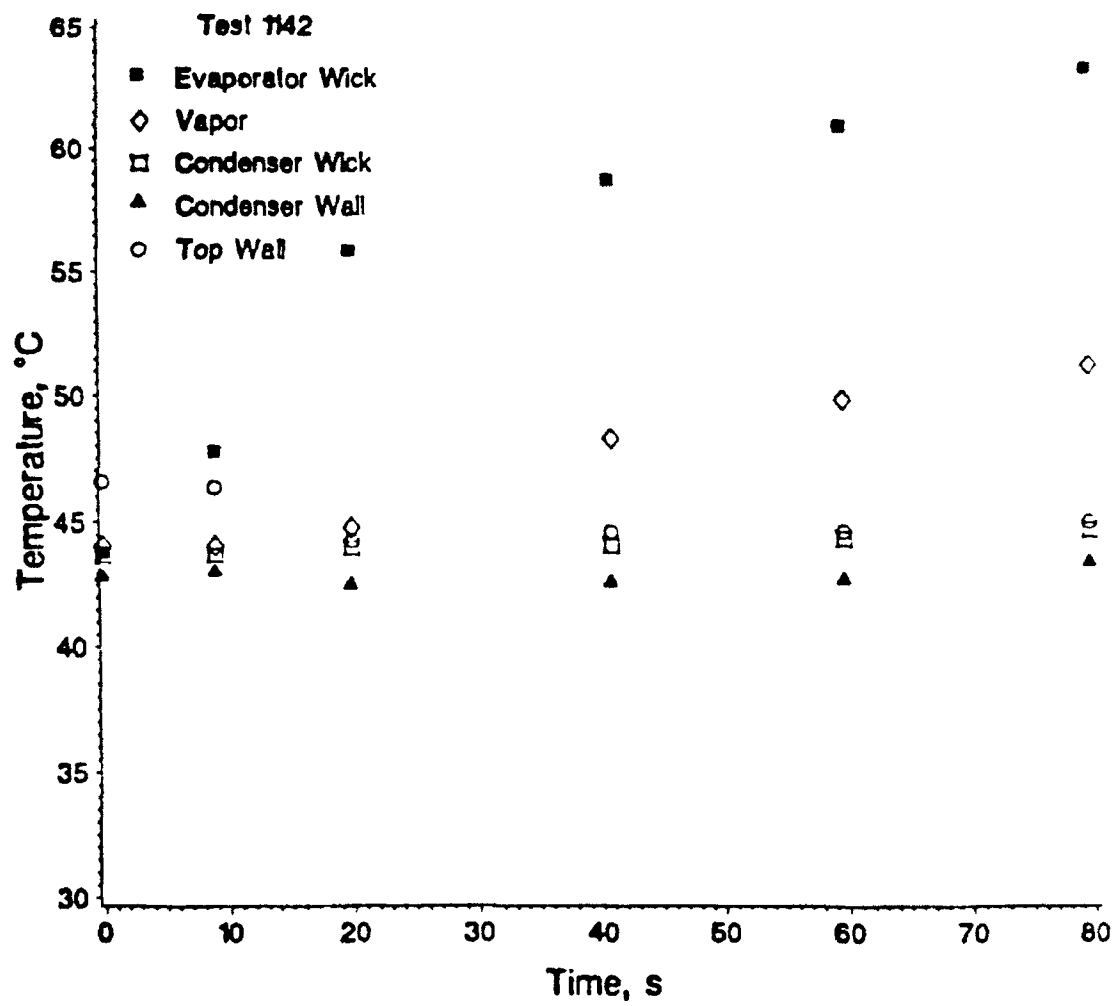


Fig 57 Transient Temperatures, Test 1142

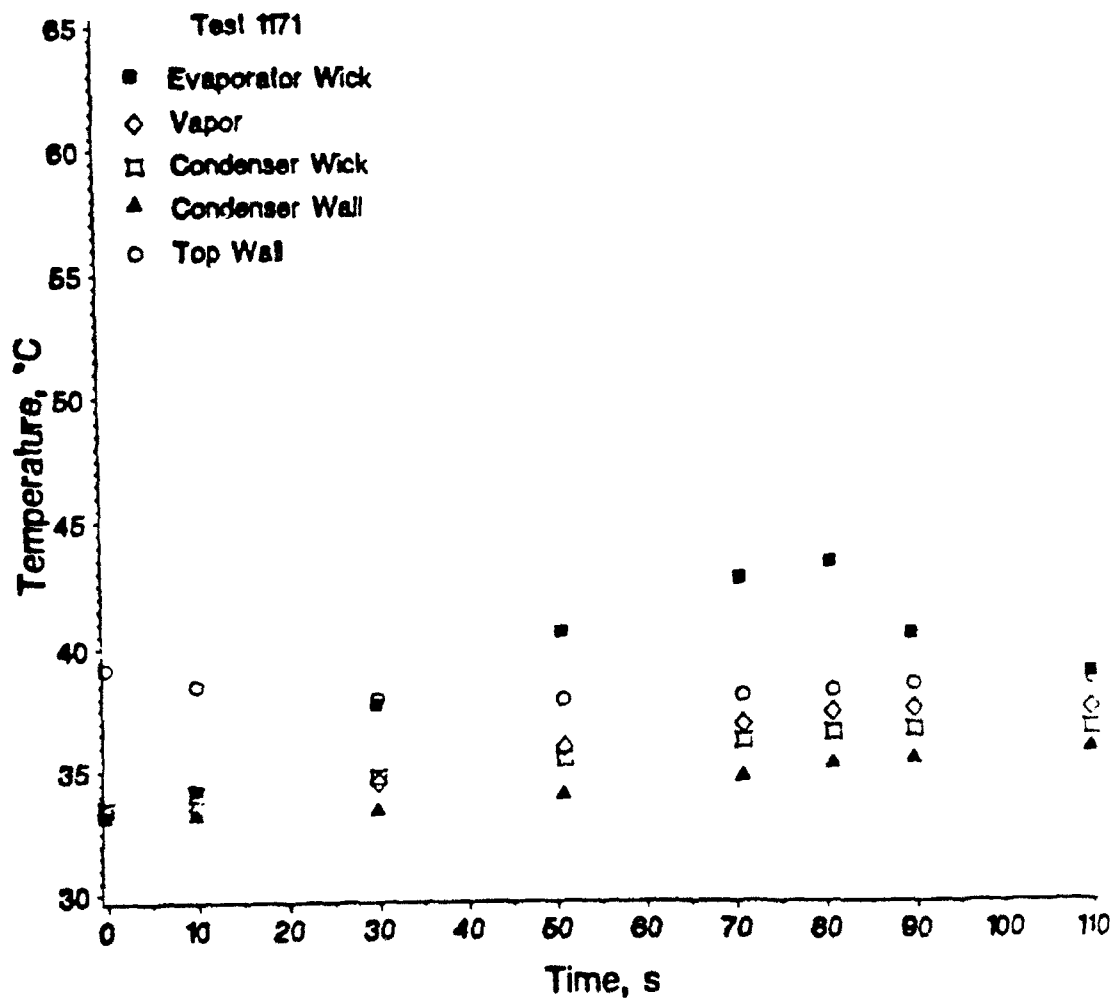


Fig 58 Transient Temperatures, Test 1171

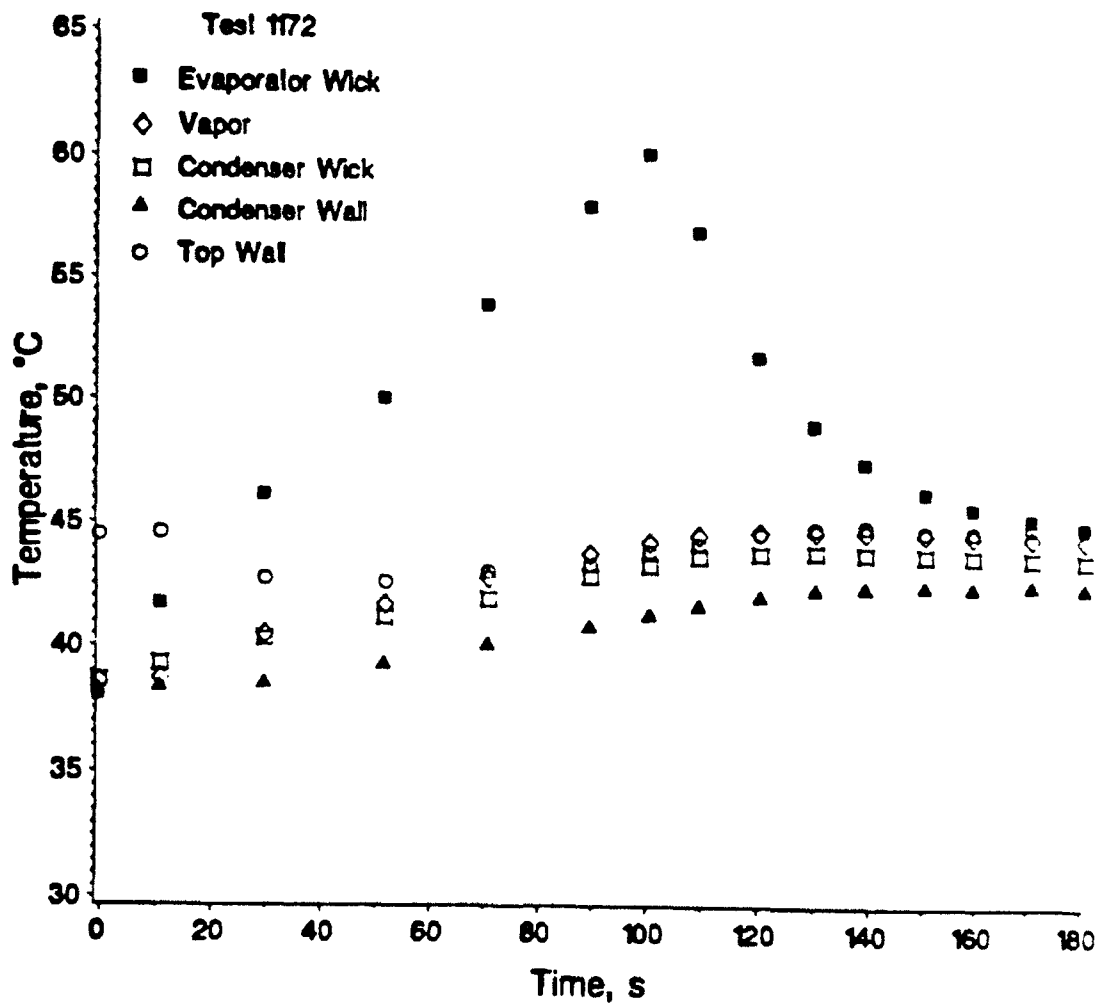


Fig 59 Transient Temperatures, Test 1172

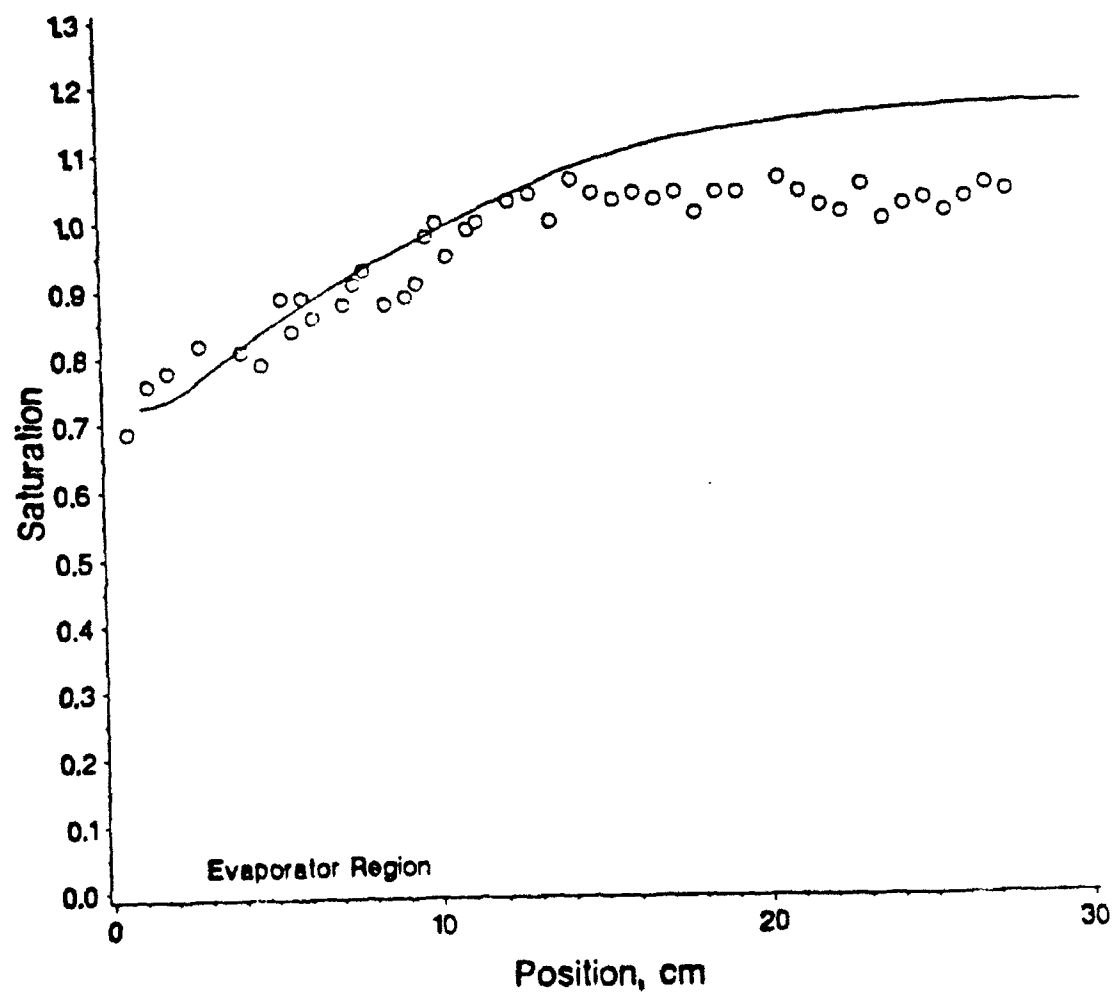


Fig 60 Steady-State Saturation Profile

on the condenser would provide some cooling of the heater in this case.

The temperature measurements for test 114S are shown in Fig 61. Again ΔT_e agrees well with the predicted value for the estimated evaporator heat flux. The temperature of the wall measured near the heater (but in the condenser region of the wall) is much larger than the average condenser wall temperature. This indicates that some heat is conducted along the wall to the condenser region. Because of this and the nonuniform thickness of the heater (Fig 45), the actual heat-input profile is not uniform. The relative magnitude of the source term corresponding to the estimated actual heat-input profile is shown in Fig 62. Also shown in the figure is the idealized source term profile which is utilized in the solution of the liquid flow model.

Comparison of Theoretical and Experimental Results

The results of the numerical solution compare fairly well with those of the heat pipe tests. The reason for the difference between the predicted and measured saturation distribution is the lack of detailed energy coupling in the liquid flow model.

The heat input to the heat pipe cannot be a step function of time and space as it is in the model. The possible variation with position was shown in Fig 62. The heater probably stores significant amounts of heat. The heater temperature increases dramatically during the first seconds of the pulse to overcome both the contact resistance and the thermal resistance of the insulator. The estimated heat capacity of the heater is 14 J/°C. This means that the actual heat input to the heat pipe is less severe than the source term utilized in the model, as shown in Fig 63. The transient response in the experiment is controlled by

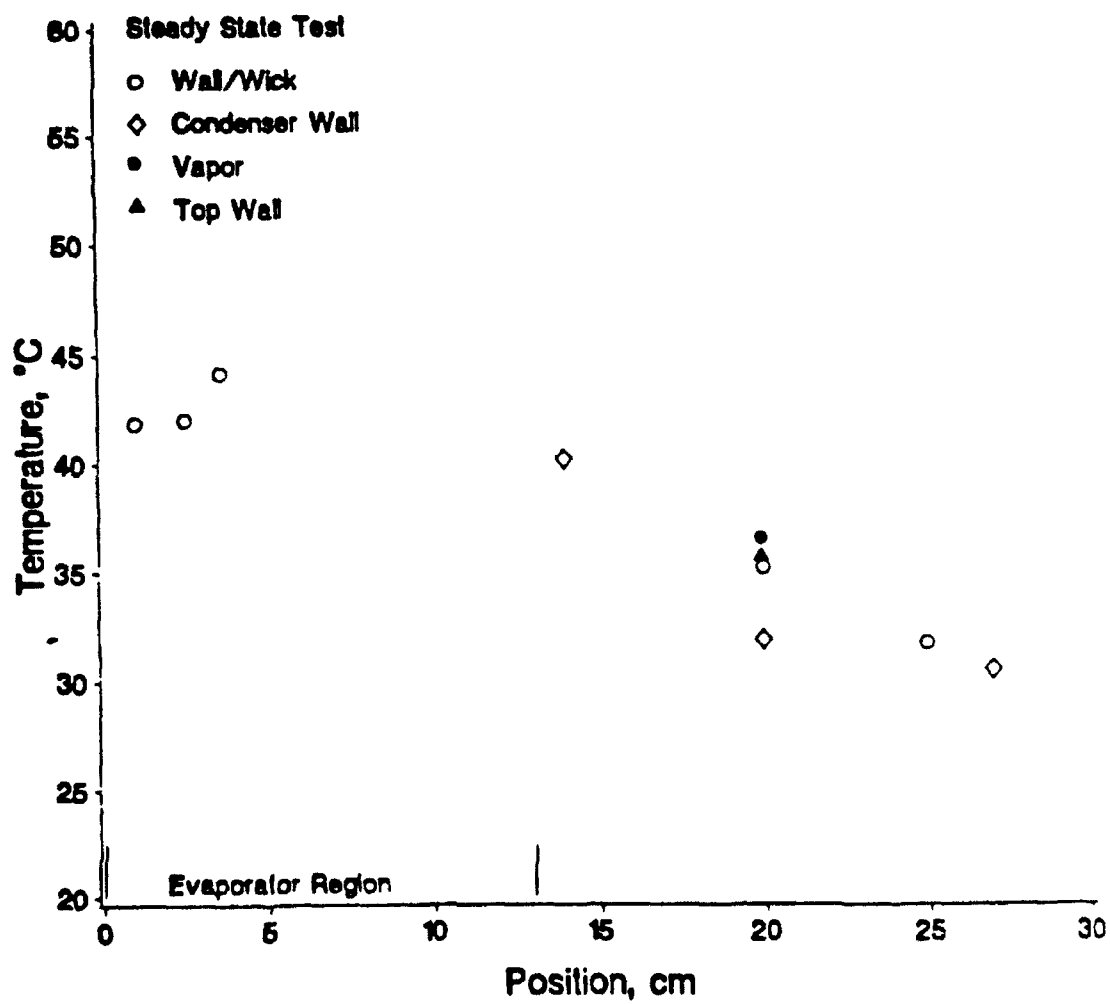


Fig 61 Steady-State Temperatures

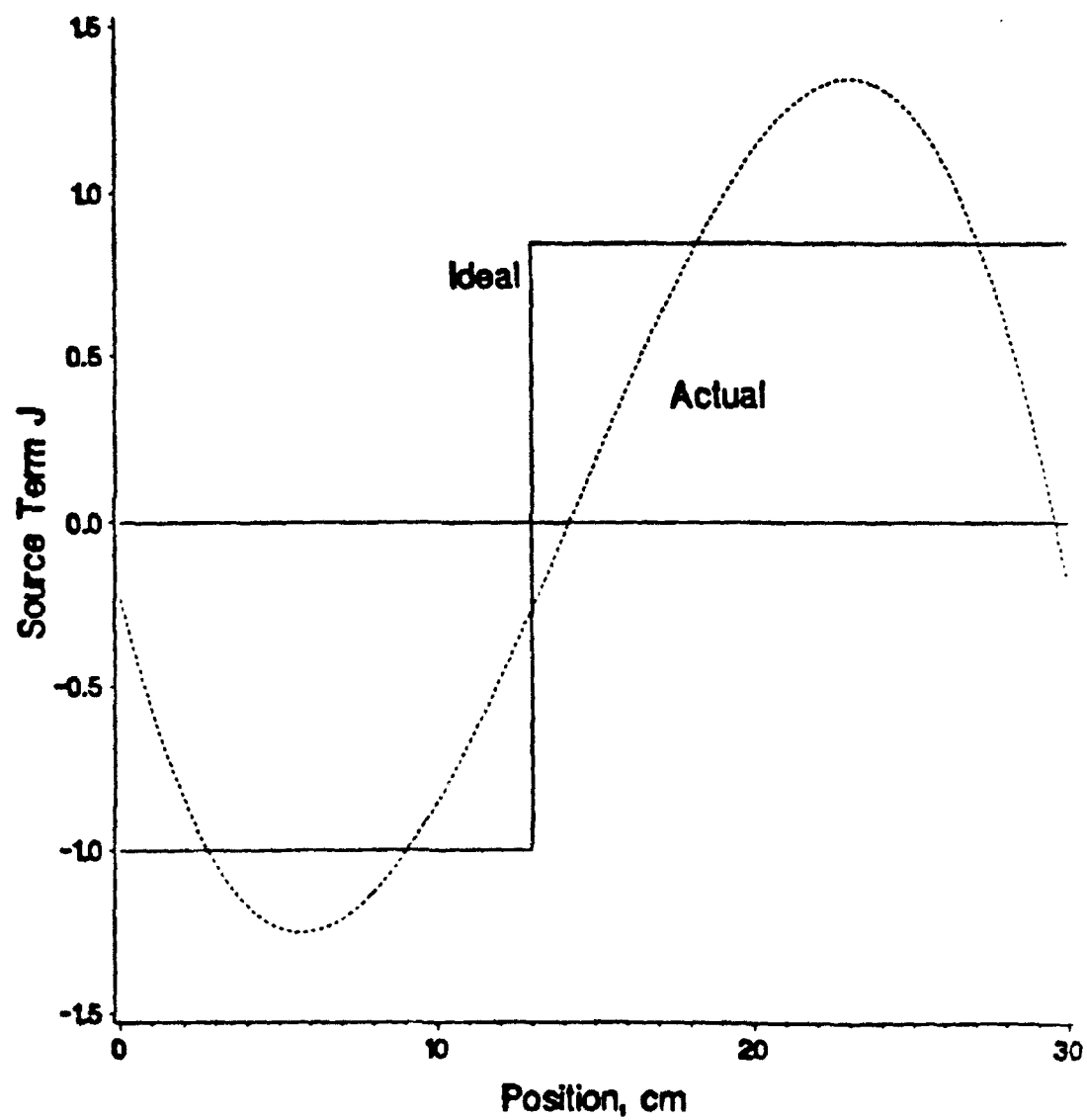


Fig 62 Spatial Dependence of the Source Term

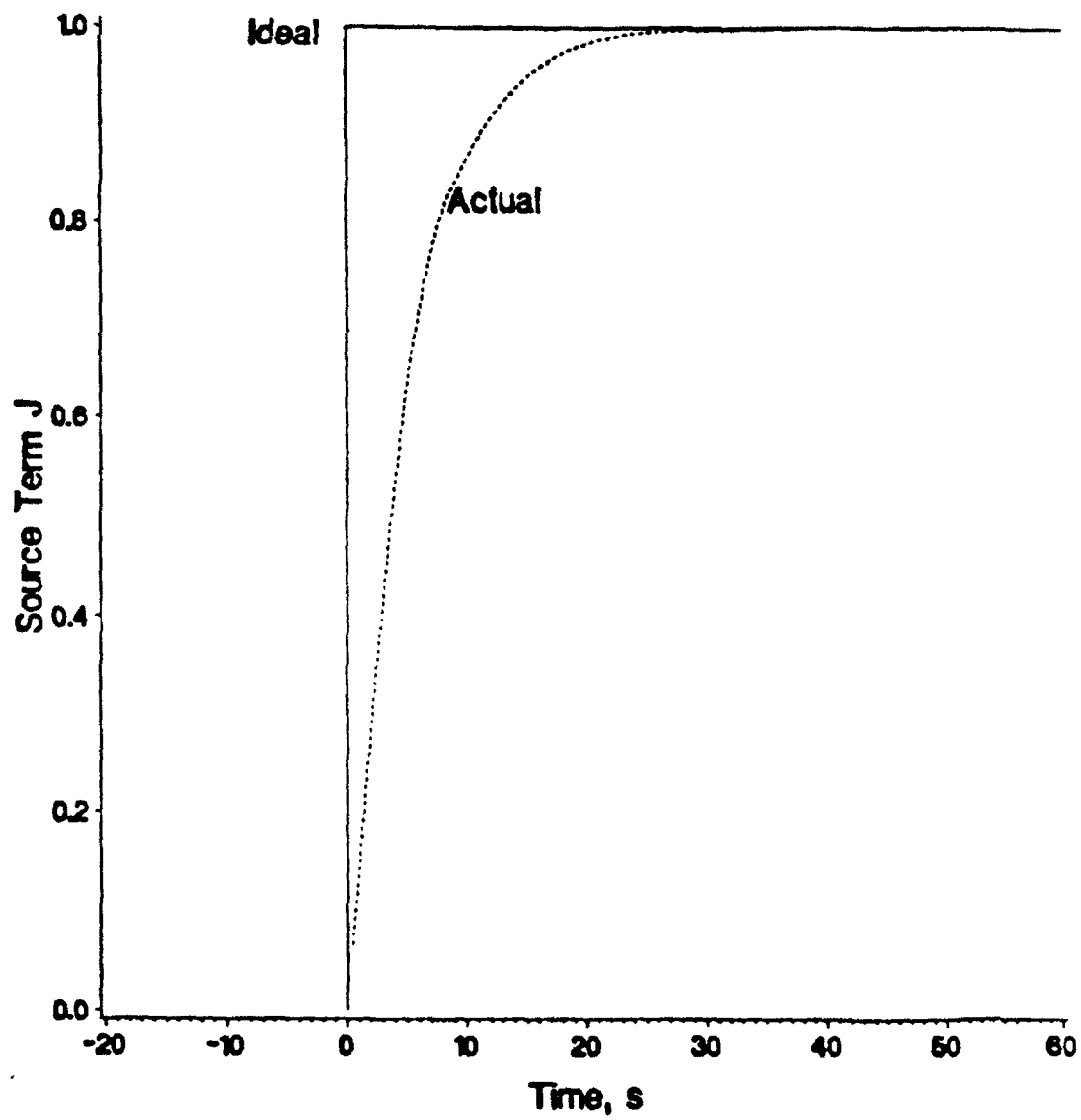


Fig 63 Temporal Dependence of the Source Term

the heat transfer rather than the fluid flow.

The actual heat input must vary continuously in space and time. This accounts for the difference in shape between measured and predicted saturation distributions in the evaporator region.

When overall energy storage is accounted for, the test results show similar reductions in saturation in the heated region to those predicted by the model.

Chapter 6

CONCLUSIONS

A detailed study of transient liquid movement in heat pipe wicks has been completed. An initial extension of a flat-front model for drying and rewetting of the wick provided useful information, but led to the conclusion that a new and more detailed liquid flow model was necessary for better accuracy. This led to the development of a technique utilizing X-ray radiography to measure liquid distribution in porous wick structures. Capillary flow properties were measured and shown to depend in an expected way on liquid saturation. These saturation dependent properties were used in a new, detailed, transient liquid-flow model to predict liquid distributions in the heat pipe wick under pulsed heat loading conditions. An experimental measurement of the liquid distributions in a heat pipe under pulsed loading conditions was performed to verify the model. The measured distributions compared favorably with those predicted using the model considering the non-ideal nature of the experiment.

The results for the saturation dependence of the capillary pressure verify the validity of the dimensionless scaling first proposed by Leverett. This scaling, named after Leverett, allows a calculation of the capillary pressure distribution for a variety of mesh wicks without difficult experimental measurements. Only the porosity and full permeability of the wick and surface tension of the liquid need be known.

Results for the relative permeability show the expected monotonically increasing trend. Unlike earlier results for the granular

materials, the present results are better fit by reduced saturation raised to the second rather than third power. This difference may be due to uncertainties in the present measurements or full permeability values used, or may be actual. Because of the good comparison of the capillary pressure results, it was also intuitively expected that the relative permeability would compare with previous results for granular media.

The results of the liquid flow model show that there is a rather steep drop in saturation in the evaporator region of the wick. This steep drop is also present in the experimental results obtained from the beryllium heat pipe. The nature of the measured distribution in the evaporator region is slightly different, these differences are explained by the non-ideal nature of the heat input in the experiment.

The objective of development of the detailed liquid-flow model was to create a much more powerful predictive tool for transient operation than was previously available. The results have pointed out that there are significant saturation reductions in the evaporator of a low-temperature heat pipe, even under conditions of steady-state operation. This fact provides further evidence of the usefulness of the liquid flow model. The transient operation of the heat pipe depends upon the previous heat loading history because this determines the distribution of liquid within the heat pipe. The distribution affects the performance capability.

Another important aspect of the new model is that it greatly increases the ability to accurately model the energy flow and temperature distributions. Previous energy modeling for low-temperature

heat pipes has been lacking in regard to adequate description of the heat transfer in the wick. One very important step forward was the recognition that boiling plays a major role in the evaporative heat transfer. The present model will allow another important advance in the modeling of heat transfer in the wick to be made, namely the saturation dependence of the wick thermal properties:

1. Using the liquid flow model, the (significant) changes in thermal resistance of the wick in the condenser can be modeled. When excess liquid is present, the conduction across this layer increases the temperature drop across the wick.
2. Temperature increases in the evaporator region during dryout can be more accurately modeled if the extent of the dry region is known. Prescription of the boundary condition at the interface between wall and wick during dryout requires detailed knowledge of the local saturation distribution.

Appendix A

UNCERTAINTY ANALYSIS

In any experiment, the uncertainty of measurements is important in determining the value of the results. In the present work the most important value measured was the saturation. Because this value involved a complex measurement procedure, there are many possible areas of uncertainty. These will be discussed in order of importance, starting with the assumption of constant attenuation coefficient.

Assumption of Constant Attenuation Coefficient

In Chapter 3, it was stated that the saturation could be determined accurately by comparison of optical densities taken from X-rays. A set of several X-rays of wicks containing known amounts of fluid would be sufficient for calibration. However, because the heat pipe wicks used were limited in thickness, an extensive calibration would introduce still further uncertainty. The reason for additional uncertainty stems from the nature of the liquid distribution at equilibrium in a capillary structure. Known amounts of fluid could be introduced into any structure which, having known porosity, would allow a knowledge of the overall saturation. However, in the wicks of interest, the local saturation could vary greatly even if the overall amount of fluid present in the structure is known. For this reason, the calibration procedure described above was not attempted, or rather was abridged severely. X-rays were taken of wicks which were completely dry or fully saturated. The saturation was calculated assuming a constant attenuation coefficient. Bougar's Law relating incident and transmitted

radiation intensities is given as:

$$I/I_0 = \exp(-\kappa\ell) , \quad (A.1)$$

where κ is the attenuation coefficient and ℓ is the thickness of material penetrated. In this relation, κ must be considered constant. It actually depends on wavelength, so this relation is exact only for monochromatic radiation. The radiation from an X-ray tube is white radiation and as such, the energy distribution of the beam will change upon passing through a material. The weaker, longer wavelengths will be absorbed much more than the shorter ones.

The local saturation defined for one axial location of the wick is proportional to the amount of liquid at that location. This is the equivalent thickness of the liquid layer. If this thickness is ℓ_0 for the fully saturated case, then we have for the saturation:

$$S = \frac{\ell}{\ell_0} . \quad (A.2)$$

If a constant attenuation coefficient is assumed (Bougar's Law), then the local saturation can be written as:

$$\frac{\ell}{\ell_0} = \frac{\ln(I_d/I_{ps})}{\ln(I_d/I_{fs})} \quad (A.3)$$

where the I s are the transmitted intensities in the fully saturated, dry and partially saturated cases, I_{fs} , I_d and I_{ps} , respectively. Thus each saturation value is calculated from three different optical density

measurements. These readings will be designated as D_{fs} , D_d and D_{ps} , respectively. For the films used in this study, the optical density is proportional to the logarithm of the exposure over most of the useful range of exposures [34]. In terms of the optical densities, the saturation is then:

$$S = \frac{D_d - D_{ps}}{D_d - D_{fs}} . \quad (A.4)$$

The validity of using the constant attenuation coefficient assumption can be assessed by plotting the optical density versus thickness of material penetrated. In the present investigation, this was accomplished by making a wedge shaped vessel using two beryllium plates. The plates touched each other at one end and separated to a spacing of about 1/4 inch at the other end, about 11 inches away. The void in this vessel was filled with working fluid and X-ray radiographs were taken. The thickness of fluid penetrated was thus linear, and the plot of optical density versus thickness is shown in Figs A.1,A.2. Fig A.1 was obtained using Freon 113 and Fig A.2 was obtained using methanol. It is seen from these plots that the behavior can be approximated as linear, provided that the thickness range is not large. For Freon 113 and thicknesses of 0 to 1 mm, the maximum deviation from linear behavior is about 10%. The experiments involving freon used wicks of the order of 1 mm thick. For methanol the deviation from linear behavior is approximately 30% for thicknesses up to about 6 mm. The relative permeability experiment utilized methanol and a wick of about 9 mm thick. Because of the porosity of around 70%, the thickness of liquid

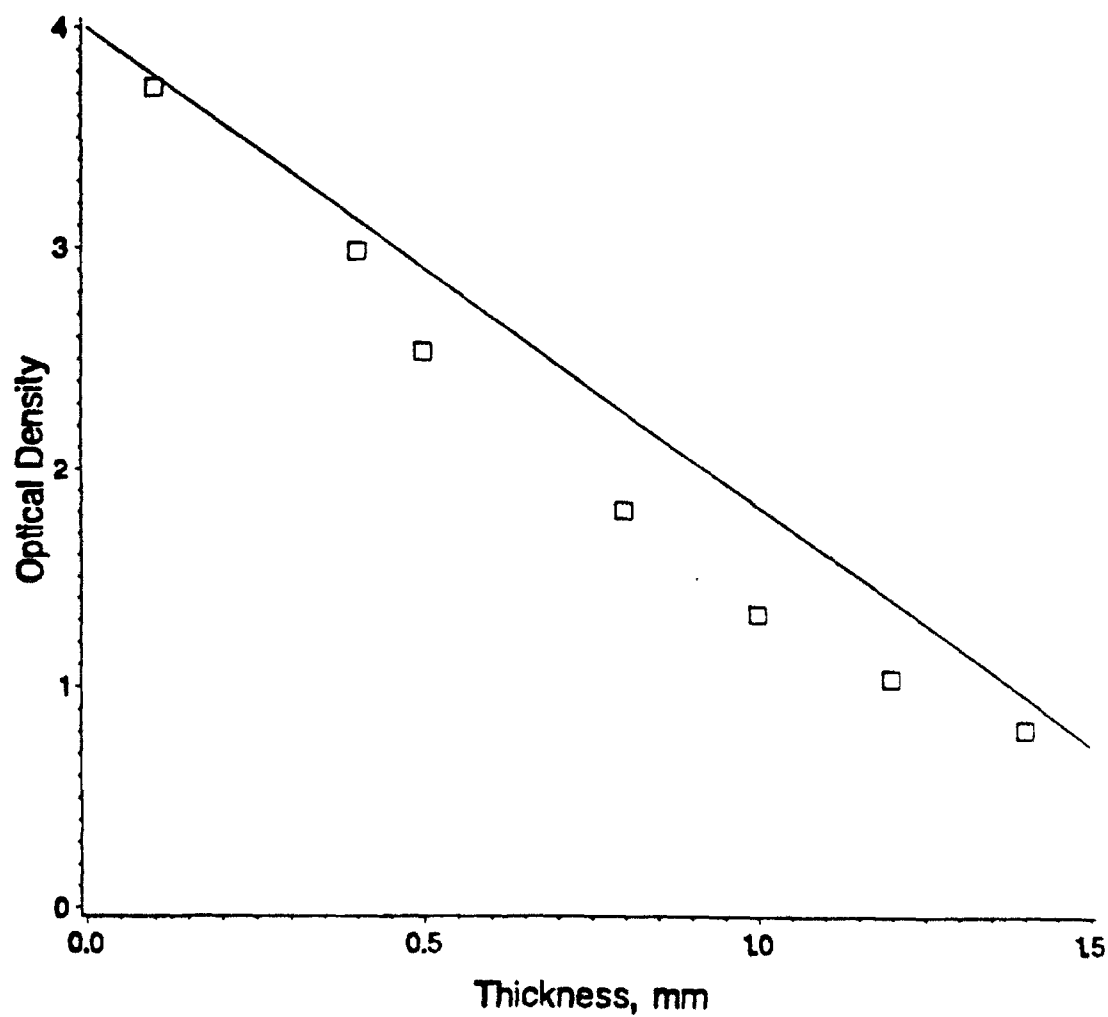


Fig A.1 Effective Attenuation Coefficient - Freon 113

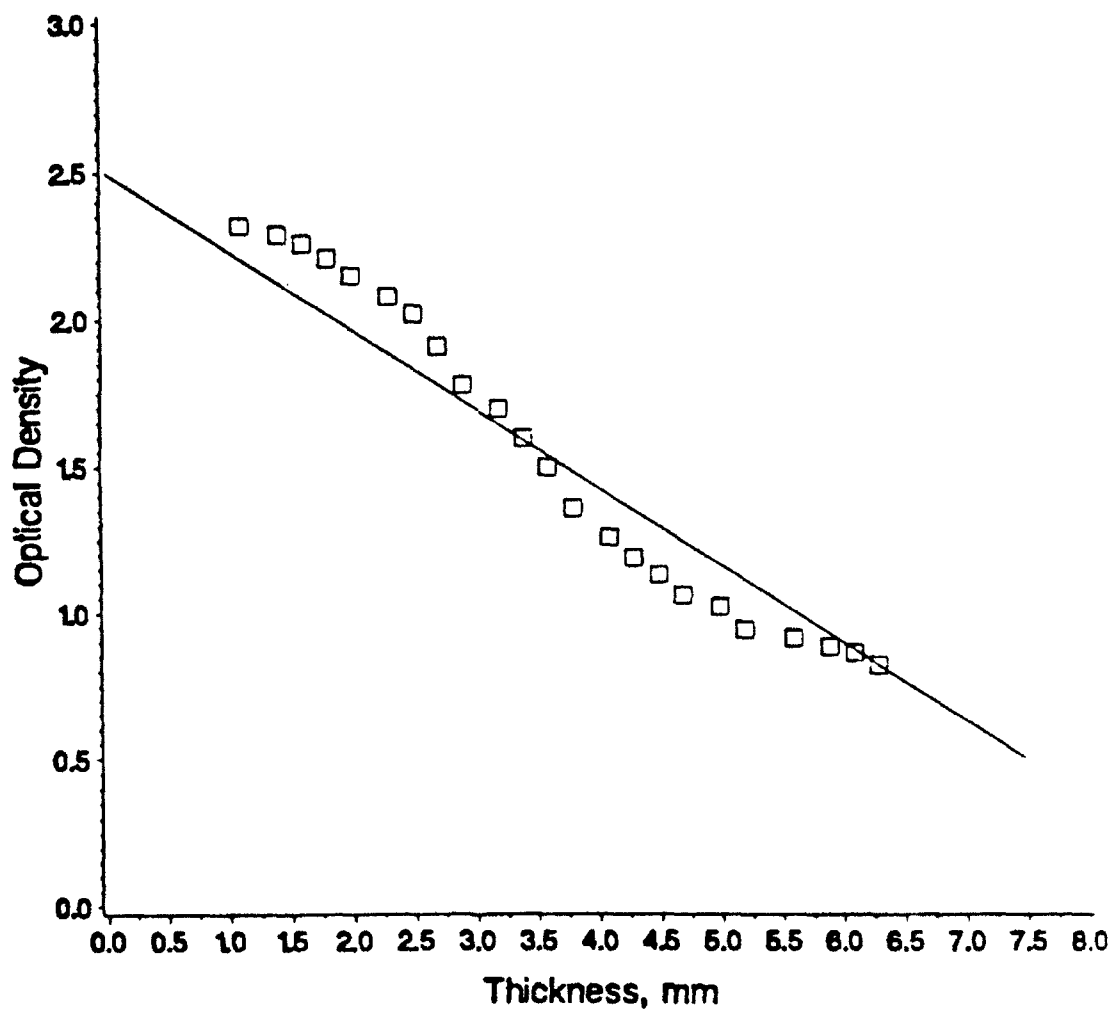


Fig A.2 Effective Attenuation Coefficient - Methanol

would be about 6.5 mm for the fully saturated case.

Optical Density Measurements

The uncertainty in the measurement of optical density using the X-Rite model 301RS photodensitometer is given as $\pm 0.02D$ for the density range 0 to 5D. This level of uncertainty is related to the saturation measurement as follows. The saturation corresponding to D_{ps} is given by Eq(A.4). Let $\Delta S = D_d - D_{ps}$ and $\Delta S' = D_d - D_{fs}$. Then $S = \Delta S / \Delta S'$. The uncertainty in the measurement S is given by [35]:

$$W_S = \left[(0.02)^2 \left[\left(\frac{\Delta S' - \Delta S}{\Delta S'} \right)^2 + \left(\frac{1}{\Delta S'} \right)^2 + \left(\frac{\Delta S}{\Delta S'^2} \right)^2 \right] \right]^{1/2} . \quad (A.5)$$

This uncertainty will obviously be greatest for very small optical densities. Provided that $\Delta S'$ is approximately one, W_S can be approximated by:

$$W_S = 0.028 \sqrt{1 + 1/S^2} - 1/S \quad (A.6)$$

This uncertainty is tabulated in Table A-1 for the range of S . In all measurements, the exposure parameters were adjusted so that $\Delta S'$ was at least unity.

Table A-1. Uncertainty of Saturation Measurement

S	0.9	0.8	0.7	0.6	0.5	0.4	0.3	0.2	0.1
W_S	3%	3.2%	3.6%	4.1%	4.9%	6.0%	8.4%	13%	27%

It is seen that the uncertainty increases rapidly for small values of the saturation. This is due in most part to the decrease in absolute magnitude of the saturation. For saturations of the order of a few percent, the uncertainty is 100%.

Overall Uncertainty of Measurement

Based on the two sources of uncertainty described in this section, the overall uncertainty in S is estimated to approximately 20%, for saturations greater than 0.1. For saturations less than 0.1, it becomes larger.

Uncertainty of Relative Permeability Calculation

The relative permeability values calculated from the transient wicking rise results are given by:

$$K_r = - \frac{\mu U}{K \frac{dP_c}{dS} \frac{\partial S}{\partial x}} . \quad (A.7)$$

The term which introduces the greatest uncertainty in Eq(A.7) is the saturation gradient. This was obtained by first fitting the saturation data with a second-order polynomial over the region of interest and then calculating the derivative of the polynomial. If the polynomial in x is given by:

$$S = \beta_0 + \beta_1 x + \beta_2 x^2 , \quad (A.8)$$

then the variance of the slope is given by:

$$\text{var}(dS/dx) = \text{var}(\beta_1) + 4x^2 \text{var}(\beta_2) + 2xcov(\beta_1\beta_2) . \quad (A.9)$$

The variance data were calculated for the quantities and for the multiple $S(x)$ curves. From this the standard deviation of the derivative term was found to be 25-30%. Based on this and the uncertainty of the S , the uncertainty in the relative permeability calculation is estimated to be as large as 50% for the lower saturation range. This large uncertainty is reflected by scatter in the relative permeability data.

Appendix B
EVALUATION OF NUMERICAL PARAMETERS
USED IN SPRINT CODE

To obtain the most accurate solution to the problem Eq(42), the effect of number of grid points, size of time step and tolerance on time integration were examined. The examination consisted of comparing results for a given time ($t=20$ seconds) and source term ($Q=20$ W) while varying one of the above parameters.

Table B-1 shows the effect of variation of number of grid points. It is seen that the results are quite insensitive, especially so for 60 or more grid points.

Table B-2 shows the effect of variation of time step. Again, the results show no change for the limited range examined. The range of time steps examined was limited because of the computational time required for the code.

Table B-3 shows the effect of variation of the tolerance placed on the time integration. It is seen that setting the tolerance lower than 10^{-4} has virtually no effect on the results.

Based on the numerical experimentation outlined here, a set of parameters was chosen for the final results presented in Chapter 5.

These parameters are:

1. Number of grid points - 120
2. Size of time increment - 1 second
3. Tolerance on time integration - 10^{-4}

Table B-1. Effect of Grid Size

EVALUATION OF GRID SIZE USING SPRINT CODE
Q-20 TIME STEP = 1.0 SECOND

NO. POINTS	30	60	120	300
	0.8271638E+00	0.8259208E+00	0.8253792E+00	0.8250791E+00
	0.8271638E+00	0.8268856E+00	0.8268084E+00	0.8267805E+00
	0.8310652E+00	0.8316181E+00	0.8319338E+00	0.8321334E+00
	0.8385747E+00	0.8397757E+00	0.8403917E+00	0.8407629E+00
	0.8491798E+00	0.8508291E+00	0.8516474E+00	0.8521325E+00
	0.8622596E+00	0.8641697E+00	0.8651002E+00	0.8656471E+00
	0.8771899E+00	0.8792025E+00	0.8801714E+00	0.8807374E+00
	0.8934125E+00	0.8954055E+00	0.8963567E+00	0.8969094E+00
	0.9104678E+00	0.9123532E+00	0.9132469E+00	0.9137633E+00
	0.9279984E+00	0.9297168E+00	0.9305261E+00	0.9309909E+00
	0.9457377E+00	0.9472520E+00	0.9479597E+00	0.9483633E+00
	0.9634937E+00	0.9647824E+00	0.9653785E+00	0.9657154E+00
	0.9811315E+00	0.9821843E+00	0.9826636E+00	0.9829314E+00
	0.9972819E+00	0.9981457E+00	0.9985299E+00	0.9987416E+00
	0.1011404E+01	0.1012225E+01	0.1012579E+01	0.1012776E+01
	0.1024529E+01	0.1025349E+01	0.1025694E+01	0.1025883E+01
	0.1036665E+01	0.1037528E+01	0.1037884E+01	0.1038078E+01
	0.1047824E+01	0.1048773E+01	0.1049161E+01	0.1049370E+01
	0.1058015E+01	0.1059094E+01	0.1059534E+01	0.1059771E+01
	0.1067247E+01	0.1068500E+01	0.1069013E+01	0.1069290E+01
	0.1075529E+01	0.1077000E+01	0.1077607E+01	0.1077937E+01
	0.1082869E+01	0.1084603E+01	0.1085325E+01	0.1085720E+01
	0.1089275E+01	0.1091317E+01	0.1092176E+01	0.1092647E+01
	0.1094752E+01	0.1097149E+01	0.1098166E+01	0.1098727E+01
	0.1099308E+01	0.1102105E+01	0.1103302E+01	0.1103965E+01
	0.1102946E+01	0.1106191E+01	0.1107590E+01	0.1108369E+01
	0.1105671E+01	0.1109412E+01	0.1111036E+01	0.1111942E+01
	0.1107486E+01	0.1111771E+01	0.1113642E+01	0.1114690E+01
	0.1108394E+01	0.1113270E+01	0.1115412E+01	0.1116615E+01
	0.1108394E+01	0.1113913E+01	0.1116349E+01	0.1117721E+01

Table B-2. Effect of Time Step

EVALUATION OF TIME STEP USING SPRINT CODE
Q = 20 NO. GRID INCREMENTS = 120

TIME STEP	2.0	1.0	0.1
0.8253784E+00	0.8253784E+00	0.8253792E+00	0.8253801E+00
0.8268076E+00	0.8268076E+00	0.8268084E+00	0.8268093E+00
0.8319330E+00	0.8319330E+00	0.8319338E+00	0.8319348E+00
0.8403909E+00	0.8403909E+00	0.8403917E+00	0.8403928E+00
0.8516466E+00	0.8516466E+00	0.8516474E+00	0.8516485E+00
0.8650995E+00	0.8650995E+00	0.8651002E+00	0.8651012E+00
0.8801708E+00	0.8801708E+00	0.8801714E+00	0.8801722E+00
0.8963563E+00	0.8963563E+00	0.8963567E+00	0.8963573E+00
0.9132465E+00	0.9132465E+00	0.9132469E+00	0.9132474E+00
0.9305258E+00	0.9305258E+00	0.9305261E+00	0.9305266E+00
0.9479594E+00	0.9479594E+00	0.9479597E+00	0.9479602E+00
0.9653782E+00	0.9653782E+00	0.9653785E+00	0.9653790E+00
0.9826633E+00	0.9826633E+00	0.9826636E+00	0.9826642E+00
0.9985297E+00	0.9985297E+00	0.9985299E+00	0.9985306E+00
0.1012579E+01	0.1012579E+01	0.1012579E+01	0.1012578E+01
0.1025694E+01	0.1025694E+01	0.1025694E+01	0.1025693E+01
0.1037884E+01	0.1037884E+01	0.1037884E+01	0.1037884E+01
0.1049161E+01	0.1049161E+01	0.1049161E+01	0.1049160E+01
0.1059534E+01	0.1059534E+01	0.1059534E+01	0.1059533E+01
0.1069013E+01	0.1069013E+01	0.1069013E+01	0.1069012E+01
0.1077607E+01	0.1077607E+01	0.1077607E+01	0.1077606E+01
0.1085326E+01	0.1085326E+01	0.1085325E+01	0.1085325E+01
0.1092176E+01	0.1092176E+01	0.1092176E+01	0.1092175E+01
0.1098166E+01	0.1098166E+01	0.1098166E+01	0.1098165E+01
0.1103302E+01	0.1103302E+01	0.1103302E+01	0.1103301E+01
0.1107591E+01	0.1107591E+01	0.1107590E+01	0.1107590E+01
0.1111036E+01	0.1111036E+01	0.1111036E+01	0.1111035E+01
0.1113642E+01	0.1113642E+01	0.1113642E+01	0.1113641E+01
0.1115413E+01	0.1115413E+01	0.1115412E+01	0.1115412E+01
0.1116350E+01	0.1116350E+01	0.1116349E+01	0.1116348E+01

Table B-3. Effect of Tolerance Placed on Time Integration

RTOL	1.0D-5	1.0D-6	1.0D-8
ATOL	1.0D-5	1.0D-6	1.0D-8
0.7877479E+00	0.7877467E+00	0.7877467E+00	0.7877467E+00
0.7900133E+00	0.7900122E+00	0.7900121E+00	0.7900121E+00
0.7979863E+00	0.7979852E+00	0.7979852E+00	0.7979852E+00
0.8106766E+00	0.8106756E+00	0.8106755E+00	0.8106755E+00
0.8268002E+00	0.8267993E+00	0.8267993E+00	0.8267993E+00
0.8451394E+00	0.8451386E+00	0.8451386E+00	0.8451386E+00
0.8647263E+00	0.8647257E+00	0.8647257E+00	0.8647257E+00
0.8848723E+00	0.8848718E+00	0.8848719E+00	0.8848719E+00
0.9051218E+00	0.9051215E+00	0.9051215E+00	0.9051215E+00
0.9251894E+00	0.9251891E+00	0.9251891E+00	0.9251891E+00
0.9449048E+00	0.9449046E+00	0.9449046E+00	0.9449046E+00
0.9641730E+00	0.9641729E+00	0.9641729E+00	0.9641729E+00
0.9829466E+00	0.9829466E+00	0.9829466E+00	0.9829466E+00
0.1000015E+01	0.1000015E+01	0.1000015E+01	0.1000015E+01
0.1015276E+01	0.1015276E+01	0.1015276E+01	0.1015276E+01
0.1029581E+01	0.1029581E+01	0.1029581E+01	0.1029581E+01
0.1042932E+01	0.1042932E+01	0.1042932E+01	0.1042932E+01
0.1055330E+01	0.1055331E+01	0.1055331E+01	0.1055331E+01
0.1066778E+01	0.1066778E+01	0.1066778E+01	0.1066778E+01
0.1077275E+01	0.1077276E+01	0.1077276E+01	0.1077276E+01
0.1086825E+01	0.1086825E+01	0.1086825E+01	0.1086825E+01
0.1095427E+01	0.1095428E+01	0.1095428E+01	0.1095428E+01
0.1103084E+01	0.1103084E+01	0.1103084E+01	0.1103084E+01
0.1109795E+01	0.1109796E+01	0.1109796E+01	0.1109796E+01
0.1115563E+01	0.1115564E+01	0.1115564E+01	0.1115564E+01
0.1120388E+01	0.1120389E+01	0.1120389E+01	0.1120389E+01
0.1124271E+01	0.1124271E+01	0.1124271E+01	0.1124271E+01
0.1127211E+01	0.1127212E+01	0.1127212E+01	0.1127212E+01
0.1129211E+01	0.1129212E+01	0.1129211E+01	0.1129211E+01
0.1130269E+01	0.1130270E+01	0.1130270E+01	0.1130270E+01

REFERENCES

1. Dobran, F., "Heat Pipe Research and Development in the Americas," Proc. Sixth International Heat Pipe Conference, Grenoble, France, 1987.
2. Polasek, F., Heat Pipe Research and Development in East European Countries," Proc. Sixth International Heat Pipe Conference, Grenoble, France, 1987.
3. Beam, J.E., Unsteady Heat Transfer in Heat Pipes, PhD Dissertation, School of Engineering, University of Dayton, 1985.
4. Holderness, J.H., Operation of a Heat Pipe Beyond the Capillary Limit, PhD Dissertation, Nuclear Engineering, University of Michigan, 1973.
5. Chang, W.S., Heat Pipe Start Up from the Supercritical State, PhD Dissertation, Georgia Institute of Technology, 1981.
6. Moss, R.A. and A.J. Kelly, "Neutron Radiographic Study of Limiting Planar Heat Pipe Performance," Int J. Heat Mass Transfer, Vol. 13, pp. 491-502, 1970.
7. Eninger, J.E., "Capillary Flow through Heat-Pipe Wicks," Progress in Astronautics and Aeronautics, Vol. 49, pp. 435-459, 1976.
8. Shishido, I., I. Oishi and S. Ohtani, "Capillary Limit in Heat Pipes," J. of Chemical Engineering of Japan, Vol. 17, No. 2, pp. 179-186, 1984.
9. Adam, N.M., The Physics and Chemistry of Surfaces, Oxford Press, 1930.
10. Smith, W.O., "The Final Distribution of Retained Liquid in an Ideal Uniform Soil," Physics, Vol. 4, pp. 425-438, 1933.
11. Leverett, M.C., "Capillary Behavior in Porous Solids," Trans. AIME, Vol. 142, pp. 152-169, 1941.
12. Brown, H.W., "Capillary Pressure Investigations," Trans. AIME, Vol. 192, pp. 67-74, 1951.
13. Chi, S.W., Heat Pipe Theory and Practice, Hemisphere Publishing Corp., Washington, D.C., 1976.
14. Wyckoff, R.D. and H.G. Botset, "The Flow of Gas-Liquid Mixtures Through Unconsolidated Sands," Physics, Vol. 7, pp. 325-342, 1936.
15. Leverett, M.C. and W.B. Lewis, "Steady Flow of Gas-oil-water Mixtures through Unconsolidated Sands," Trans. AIME, Vol. 142, pp. 107-116, 1941.

16. Miller, F.G., "Steady Flow of Two-Phase Single-Component Fluids through Porous Media," Trans. AIME, Vol 192, pp. 205-216, 1951.
17. Udell, K.S., "Heat Transfer in Porous Media Considering Phase Change and Capillarity - the Heat Pipe Effect," Int. J. Heat Mass Transfer, Vol. 28, No. 2, pp.485-495, 1985.
18. Udell K.S., "Heat Transfer in Porous Media Heated from Above with Evaporation, Condensation and Capillary Effects," J. Heat Transfer, Vol. 105, No. 3, pp. 485-492, 1983.
19. Chang, W.S. and G.T. Colwell, "Mathematical Modeling of the Transient Operating Characteristics of a Low-Temperature Heat Pipe," Numerical Heat Transfer, Vol. 8, pp. 169-186, 1985.
20. Merrigan, M.A., E.S. Keddy and J.T. Sena, "Transient Performance Investigation of a Space Power System Heat Pipe," AIAA 86-1273, 1986.
21. Brennan, P.S. and E.J. Kroliczek, Heat Pipe Handbook, Vol. 2, B&K Engineering, Inc., Towson MD, 1979.
22. Boyer, R.L., F. Morgan and M. Muskat "A New Method for Measurement of Oil Saturation in Cores," Trans. AIME, Vol. 170, pp. 15-33, 1947.
23. Morgan, F., J.M. McDowell and E.C. Doty, "Improvements in the X-Ray Saturation Technique of Studying Fluid Flow," Trans. AIME, Vol. 189, PP. 183-194, 1950.
24. Laird, A.D.K. and J.A. Putnam, "Fluid Saturation in Porous Media by X-Ray Technique," Trans. AIME, Vol. 192, pp. 275-284, 1951.
25. Matsumoto, G., M. Tamaki, K. Ohkubo and Y. Ikeda, "Real-Time Image of Working Fluids in Heat Pipes by Neutron Television," Proc. Fifth International Heat Pipe Conference, Tsukuba, Japan, 1984.
26. Friedman, H. and L.S. Birks, "Thickness Measurement of Thin Coatings by X Ray Absorption," Rev. Sci. Instr., Vol. 17, No. 3, March 1946.
27. Phillips, J.R., L.C. Chow and W.L. Grosshandler, "Thermal Conductivity of Layered Cloth Heat Pipe Wicks," J. Heat Transfer, Vol. 109, No. 3, pp. 775-781, 1987.
28. Vafai, K. and C.L. Tien, "Boundary and Inertia Effects on Flow and Heat Transfer in Porous Media," Int. J. Heat Mass Transfer, Vol. 24, pp. 195-203, 1981.
29. Shibayama, S. and S. Morooka, "Study on a Heat Pipe," Int. J. Heat Mass Transfer, Vol. 23, pp. 1003-1013, 1980.

30. Scheidegger, A.E., The Physics of Flow Through Porous Media, Macmillan Co., New York, 1957.
31. Berzins, M., R.M. Furzeland, A User's Manual for Sprint, Parts 1 and 2, Department of Computer Studies Reports 199 and 202, Leeds University, England, 1986.
32. Berzins, M., P.M. Dew and R.M. Furzeland, "Developing Software for Time Dependent Problems Using the Method of Lines and the Differential Algebraic Integrators," Applied Numerical Mathematics, to appear.
33. Ambrose, J.H., L.C. Chow, R. Ponnappan, J.E. Beam and E.T. Mahefkey, "A Boiling Heat Transfer Correlation for Heat Pipes," SAE Transactions, Vol. 94, Sect. 5, pp. 161-167, 1985.
34. Corney, G.M., "X-Ray Film," from The Encyclopedia of X-Rays and Gamma Rays, G.L. Clark, Ed., pp.375-381, Reinhold, New York, 1963.
35. Holman, J.P., Experimental Methods for Engineers, p. 45, McGraw-Hill, New York, 1978.